Development of a laser wire beam profile monitor and measurement of vertical emittance in the KEK-ATF damping ring

Hiroshi Sakai

Department of Physics , Faculty of Science

Kyoto University

Abstract

Production and manipulation of a low emittance electron beam is one of the key issues in realizing future linear colliders. Accelerator Test Facility (ATF) was constructed at KEK to develop various technologies for such a beam. ATF consists of an electron linac, a damping ring and an extraction line. Emittance of the beam is reduced in the damping ring.

Up to now, however, there is no reliable monitor which can directly measure the beam size in the ring. We have designed and built a new type of a profile monitor, which is based upon the Compton scattering process of a laser beam target with an electron beam. We call this monitor a *laser wire beam profile monitor*. By scanning the position of a laser wire and counting the number of photons emitted by the Compton process, a projected beam size can be measured. Since the vertical beam size of about 10μm is expected, the laser beam must be thinner than 10μm. For fast and precision measurement, high intensity is required for the laser beam. To satisfy these requirements, we used a Fabry-Perot optical cavity. By choosing a nearly concentric configuration, we could reduce its beam size to $7.3 \pm 0.2\mu$m (its beam waist was $w_0 = 14.5 \pm 0.4\mu$m). With high reflectivity mirrors ($> 99\%$), we achieved a power enhancement factor of 220 ± 20. The effective laser power inside the cavity exceeded 11 W.

We installed this monitor in the straight section of the ATF damping ring. We could successfully identify the Compton photons, and confirmed that the counting rate as well as its energy spectrum agreed well with the expected ones. The measured vertical emittance was $\varepsilon_y = (1.17 \pm 0.08) \times 10^{-11}$ m·rad; this value satisfies the emittance requirement set for the JLC damping ring .

The advent of the laser wire beam profile monitor will certainly open up a new era in studying beam dynamics of low emittance electron rings.

Acknowledgement

First, I would like to express my thank to Professor N. Sasao of Kyoto University for his continously encouragements and supports. I was also helped on his much fruitful discussions and comments during the laser wire experiments.

Futhremore I would especially like to thank to the Laser wire members: Prof. J. Urakawa, Dr. Y. Higashi, Dr. T. Taniguchi, Dr. T. Okugi, Mr. S. Araki of High Energy Accelerator Reserch Organization (KEK), Dr. M. Takano of Toho University, and Mr. Y. Honda of Kyoto University. I had many exciting discussions and was helped through the experiments on the view point of the software and hardware.

I would also like to express my gratitude to Prof.H.Hayano, Prof.S.Takeda, Dr. K. Kubo, Dr. N. Terunuma, Dr. T. Naito, Dr. S. Kuroda, Prof. N. Toge, Prof.S.Kamada, Dr.M.Kuriki, Prof.T.Higo, Prof.K.Oide, Prof.M.Akemoto, Prof. T. Suzuki, Dr. T. Omori, Dr. Y. Kurihara of KEK, and Mr. T. Imai, Mr.I.Yoshida, Mr.K.Hasegawa of Science Universityof Tokyo, and Mr.T.Iimura of Seikei University, and Mr. T. Sakamoto, Mr. D. Aizawa of Tohoku-Gakuin University, and Dr. K. Dobashi, Mr. K. Sugiyama, Ms. I. Sakai, Mr. T. Muto, Mr.M.Fukuda, Mr.Y.Kamiya of Tokyo Metroporitan University, and Mr.F.Tamura of University of Tokyo, and Dr. S. Kashiwagi, Mr. T. Kobuki, Mr. R. Kuroda, Ms. A. Higurashi, Mr. A. Aoki, Mr. T. Oshima of Waseda University, and Mr. S. Morita, Mr. K. Wachi, Mr. H. Edagawa, Mr. K. Nakamura of E-cube Co., and Mr. J. Ozawa, Mr. F. Takagi, Mr. A. Hayakawa, Ms. H. Otsuka of Kanto-Joho Co., and all members of the KEK-ATF group, for their many many helpful supports and was helped through the ATF beam operation.

I also thank to the old laser wire member: Mr. Y. Sakamura of Tokyo Institute for Technology, and Dr. T. Korhonen of Paul Scherrer Institute, and Mr. H. Matsuo[1], Mr. T. Shima, Mr. E. Shinya of Kyoto University, and Mr. Y. Funahashi of KEK, and Dr. Y. Hemmi of Daido Institute of Technology for their supports.

I am also grateful to Dr. M. Ross, Dr. J. Frisch, Dr. T. Kotseloglou for their fruitful discussions with our laser wire experiment. I thank to Prof.T.Shintake for their philosophical suggestion for our experiments.

I would like to thank to Prof.K.Nishikawa, Prof.H.Sakamoto, Dr.T.Nakaya, Dr.T.Nomura, Mr.M.Suehiro, Dr.Y.Takeuchi, Dr.K.Murakami, Mr.Y.Matono, Mr.Y.Ushiroda, Mr.T.Fujiwara, Mr.T.Inagaki, Mr.T.Nakamura, Ms.N.Nakamura, Mr. S. Nishida, Mr. H. Yokoyama, Mr. H. Yumura, Mr. S. Mukai, Mr. I. Kato,

[1] To the memory of HM who decreased on July 19 1998.

Mr. A. Shima, Mr. H. Maesaka, Mr. K. Mizouchi, and Ms. K. Uchida of the High Energy group of Kyoto University for continuously supporting of this experiment.

It is my pressure to thank Profs H. Sugawara, M. Kihara, Y. Kimura, S. Iwata and K. Takara for their supports.

Finally, I would like to thank my parents for their many many many continuous support and encouragement.

Contents

Chapter 1

Introduction

For confirmation of the Standard Model and investigation beyond it in high energy particle physics, a TeV-region electron linear collider is needed. JLC is one of the projects to build such a linear collider, and intensive R&D works are now underway. From the view point of high energy experiments, luminosity of a collider as well as its energy is of crucial importance. In order to realize high luminosity, electron and positron beams are squeezed into a size less than 300nm horizontally and 3nm vertically at an interaction point. To achieve such a small beam size, a low emittance electron beam is required.

An Accelerator Test Facility (ATF) was built at KEK in the hope of developing techniques for such a low emittance beam. In a damping ring at ATF, vertical beam size is squeezed to less than 10 μm. There exists no device which can directly measure such a small beam size up to now. For this purpose, we have decided to develop a new type of a beam profile monitor, which is based on the Compton scattering process of electrons with laser light. By scanning the position of a laser beam and counting the number of scattered photons, a projected beam size is obtained. We call this system a *laser wire beam profile monitor*. For precise measurement of a small beam size, a thin and intense laser beam is needed. There are two ways. One of them is to use a high power pulsed laser beam [1], [2], [3]. The other one is to use a CW laser injected into a Fabry-Perot optical cavity and to amplify the laser light. The former type is realized already, but is not suitable for the circulating beam in the damping ring. We have chosen the latter method for our purpose. The salient features of this monitor, when compared with a solid material wire scanner [4], which is commonly used for measurements of extracted beam size at the ATF damping ring, are non-destructiveness and durability in an intense circulating beam.

In this thesis, we describe development of this new beam profile monitor and measurement of vertical emittance in the ATF damping ring using it.

This thesis is organized as follows. In this chapter, we describe briefly the JLC project. Our special interests are its luminosity and vertical emittance. The principle of our laser wire is presented in chapter 2, and its experimental setup, including the ATF damping ring, is described in chapter 3. In chapter 4, data taking, data reduction and analysis procedure are described. We also present our measurement results and discussions. The last chapter is devoted to the conclusion.

1.1 JLC(Japan Linear Collider)

1.1.1 Motivation of a linear collider

Up to now, LEPII reached the highest center of mass energy ($\sim$ 200GeV) among existed electron-positron colliders. The circumference of the ring is 30km and it seems to be the largest one to build. To increase the CM energy to much higher energy by a circular collider, there is a serious problem due to synchrotron radiation. Its energy loss per one turn U_0 is expressed by [5]

$$U_0 = \frac{4\pi}{3}\frac{e^2}{(m_e c^2)^4}\frac{E_0^4}{\rho_c} \tag{1.1}$$

$$\begin{cases} E_0 & \text{Energy of electron or positron} \\ \rho_c & \text{the radius of a circular collider} \\ m_e & \text{electron mass} \\ c & \text{speed of light} \\ e & \text{charge of electron} \end{cases}$$

At LEPII (E_0 = 100GeV), for example, this energy loss is 2.9GeV per turn per electron. The attainable energy of LEPII is limited by this energy loss. To increase the CM energy up to a TeV region, it is needed to eliminate such a huge energy loss. The only possible solution is a linear collider, in which electron and positron beams are accelerated by linear accelerators with opposite directions. Recently, new electron-positron linear colliders aiming at the center of mass energy of 0.5-1.5 TeV have been proposed; NLC [6], TESLA [7] ,CLIC [8] and JLC [9]. Among them, JLC is a Japanese project for such a collider now under preparation.

Fig.1.1 shows the conceptual design of JLC. At first, electron and positron beams are accelerated up to 1.98GeV and injected into a damping ring to decrease their emittance. After going through a bunch compressor, these beams are accelerated by a main linac up to 250 $\sim$ 750 GeV. Finally these

beams are squeezed into a size less than 300nm horizontally and 3nm vertically at an interaction point to collide. This design comes from requirements to attain $\sim 1 \times 10^{34} cm^{-2} sec^{-1}$ in luminosity.

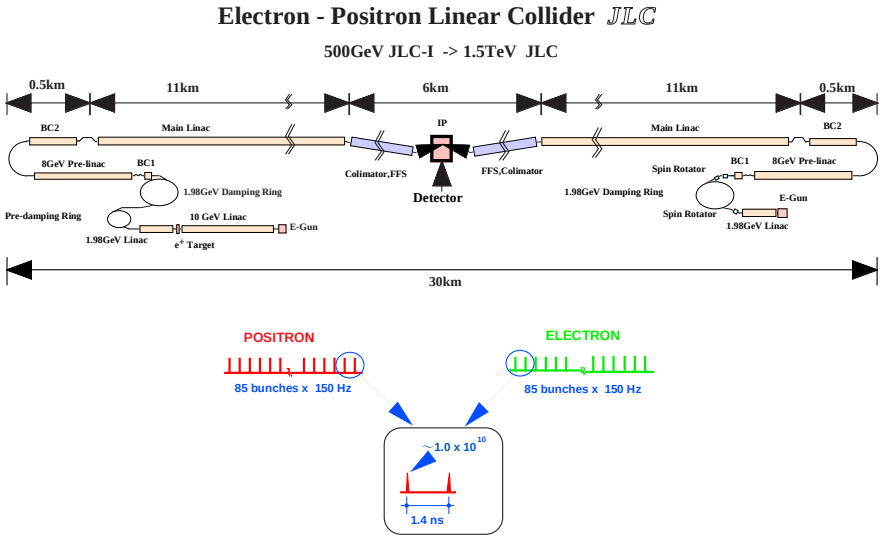

Figure 1.1: Layout of JLC.

1.1.2 Requirements from the luminosity

Luminosity is one of the most important parameters in machine design. In general, luminosity L is defined as

$$L \simeq \frac{f k_b N_e^2}{4\pi \sigma_x^* \sigma_y^*} \cdot \frac{\sigma_x^*}{\sqrt{(\sigma_x^*)^2 + (\sigma_z^* \theta_c)^2}}. \tag{1.2}$$

$$\begin{cases} N_e & \text{Number of electron per bunch} \\ k_b & \text{Number of bunch per pulse} \\ f & \text{Repetition ratio} \\ \sigma_x^* & \text{Horizontal beam size at an interaction point} \\ \sigma_y^* & \text{Vertical beam size at an interaction point} \\ \sigma_z^* & \text{Bunch length at an interaction point} \\ \theta_c & \text{Horizontal crossing angle of the beams } (\theta_c \ll 1) \end{cases}$$

Table 1.1: JLC parameters at the collision point.

Parameter		X-band		C-band		unit
Center of mass energy	E_{CM}	500	1000	500	1000	GeV
Number of particles per bunch	N_e	0.70	0.70	1.11	1.39	10^{10}
Number of bunches per pulse	k_b	85	85	72	72	-
Repetition frequency	f	150	150	100	50	Hz
Normalized emittance	$\gamma\varepsilon_x$	3.0	3.0	3.0	3.0	$10^{-6}m \cdot rad$
at damping ring exit	$\gamma\varepsilon_y$	3.0	3.0	3.0	3.0	$10^{-8}m \cdot rad$
R.m.s of beam size	σ_x^*	260	184	318	318	nm
	σ_y^*	3.14	2.28	4.43	3.14	nm
R.m.s of bunch length	σ_z^*	90	90	200	200	μm
Crossing angle	θ_c	8.0	8.0	8.0	8.0	$mrad$
Energy loss by beamstrahlung	δ_{br}	3.40	6.90	4.09	8.34	%
Luminosity	L	5.18	7.66	7.18	7.65	$10^{33}cm^{-2}s^{-1}$

From Eq.(1.2), it is clear that we must squeeze the beam sizes, σ_x^* and σ_y^*, as small as possible to reach high luminosity. In the JLC project, they are designed to be in a nanometer range.

The beam sizes σ_x^* and σ_y^* of the collision point are approximately given by

$$\sigma_x^* \sim \sqrt{\beta_x^* \varepsilon_x} \ , \ \sigma_y^* \sim \sqrt{\beta_y^* \varepsilon_y}, \tag{1.3}$$

where $\beta_{x,(y)}^*$ is a β function at the collision point and $\varepsilon_{x,(y)}$ is emittance. We note that β function is determined by a lattice optics, namely layout of magnets, especially focusing quadrupole magnets. Normalized emittance ($\gamma\varepsilon_{x,(y)}$) remains constant in a transport line, for example, in a main linac. To achieve high luminosity, the β function, of course, must be reduced. It is also essential to reduce the normalized emittance itself before injecting into the main linac.

Table.1.1 shows the main parameters at the collision point. (X-band and C-band denote the RF frequencies of the main linac.) In JLC, the normalized emittances are designed to be 3×10^{-6} m·rad horizontally, and 3×10^{-8} m·rad vertically. These values are 100 - 1000 times smaller than those of Stanford Linear Collider(SLC). We notice a big disparity between the horizontal and vertical beam size or emittance. This is because, given the same cross section

of the beam ($\pi\sigma_x^*\sigma_y^*$), a flat beam has a big advantage over a round beam in reducing so called *beamstrahlung*. This is a beam-beam interaction process during the collision, and leads to huge energy loss due to radiation.

Reduction of the emittance is achieved in a special ring called damping ring. Roughly speaking, horizontal emittance is determined by an equilibrium condition between radiation damping and quantum excitation.(See Appendix A for detail.) On the other hand, vertical emittance can be negligibly small (compared with horizontal) with a proper design for a lattice. A flat beam at collision point is a natural choice in this regard.

1.2 Measurement of the emittance in ATF damping ring

The Accelerator Test Facility (ATF) was constructed at KEK to study low emittance beam physics and to develop the technologies associated with it. As shown in Fig.1.2, it consists of an S-band electron linac, a damping ring, and an extraction line [10]. Table.1.2 shows design parameters of the ATF damping ring together with those for JLC. The same normalized emittance is set as a goal at both JLC and ATF.

The vertical beam size (σ_y) in the damping ring is expressed by

$$\sigma_y \simeq \sqrt{\beta_y \varepsilon_y + \left(\eta_y \frac{\sigma_p}{p}\right)^2}. \tag{1.4}$$

In order to measure the vertical emittance, we need to measure the beam size (σ_y), β function (β_y), dispersion function (η_y) and momentum spread ($\frac{\sigma_p}{p}$). In the ATF damping ring, the vertical beam size is in a range of 10 μm throughout the damping ring. There are two emittance monitors in ATF at present. One is a wire scanner set at the extraction line. A fine wire made of the tungsten or carbon is scanned in y(x) direction. When electrons hit the wire, photons are emitted. By counting those photons as a function of wire position, a projected beam size is obtained. There are 5 wire scanners in ATF. Results of the horizontal emittance measurement, done successfully at the extraction line, have been already published [11]. Measurement of vertical emittance was also attempted using these monitors [12]. At present, however, we cannot estimate residual vertical dispersion and/or x-y β coupling effects at the extraction line. Unfortunately no meaningful measurement is possible with these monitors.

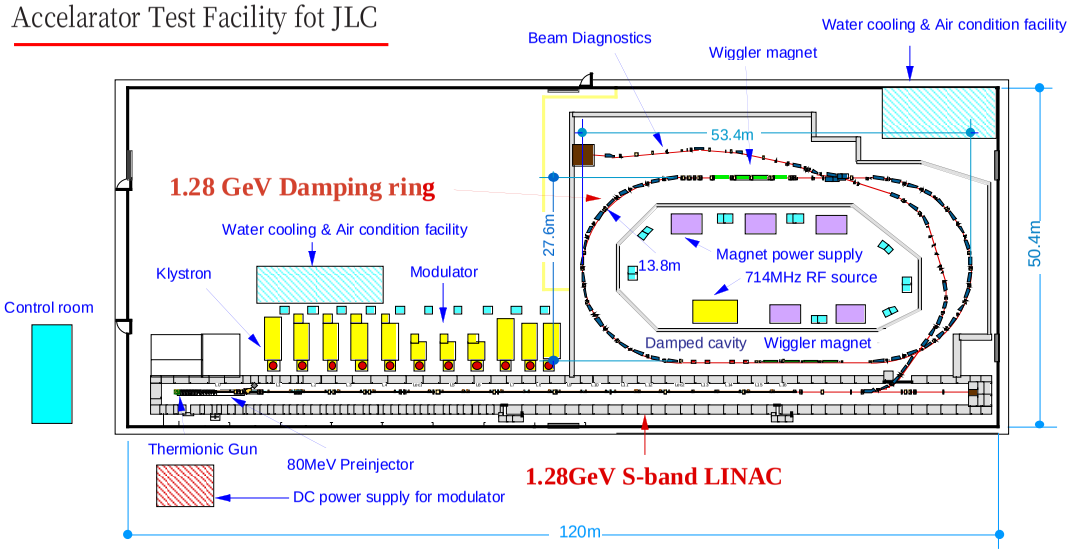

Figure 1.2: Layout of ATF

Another profile monitor is an SR interferometer installed in the damping ring. When an electron beam is bent by bending magnets, synchrotron radiation(SOR) is emitted. This SOR has beam size information. It actually measures the visibility of interference pattern in SOR made by a double slit [13]. The smaller is the beam size, the larger is the visibility. In principle, it can measure the beam size of $5-50\mu m$. In practice, however, its accuracy has not reached to the designed value. One advantage in this monitor is its fast response time ($\sim$ a few ms); thus it is used routinely to monitor beam size in the ring. Efforts are continued to improve this monitor.

We have pointed out the importance of vertical emittance measurement and lack of a monitor with enough accuracy. This situation lead us to develop a new type of a monitor. It is based on the Compton scattering process of electrons with laser light. This monitor was installed in 2000 and measured successfully vertical beam emittance in the ring for the first time [14].

In the next section, we describe this monitor in detail.

Table 1.2: ATF & JLC damping ring parameters(design value)

Parameter		ATF	JLC	unit
Energy	E_0	1.54	1.98	GeV
Circumference	C	138.6	277.12	m
Normalized emittance	$\gamma\varepsilon_x$	4.3-5.1	3	μm
	$\gamma\varepsilon_y$	30	30	nm
Bunch length	σ_z	5	4.9	mm
Particles/bunch	N_e	1-3	0.7-1.5	10^{10}
Bunch/spacing	t_b	2.8-5.6	1.4	ns
Bunch/train	N_b	10-60	85(max)	-
Train spacing	t_B	60	60	ns
Train/ring	N_B	2-5	5	-
RF frequency	f_{RF}	714.000	714.000	MHz
Harmonic number	h_c	330	660	-
Damping times	τ_x/τ_y	6.8/9.1	4.22/4.83	ms
Kicker Rise/Fall Time	τ_{kick}	60	60	ns
Momentum compaction factor	α_M	1.93×10^{-3}	8.02×10^{-4}	-
RF Voltage	V_{RF}	0.587-0.678	1.2	MV
Synchrotron radiation loss	U_0	155	758	keV
Energy spread	$\Delta E/E$	8.0	8.62	10^{-4}

Chapter 2

Laser wire

In this chapter, we describe the laser wire beam profile monitor from the theoretical viewpoint. First we explain its principle together with requirements for vertical emittance measurement. Next, we describe the characteristic of an optical cavity. Basic parameters, such as, a beam waist and power enhancement factor, are explained in detail. Finally, a count rate of scattered photons by the Compton process and their energy spectrum are estimated.

2.1 Principle of the monitor

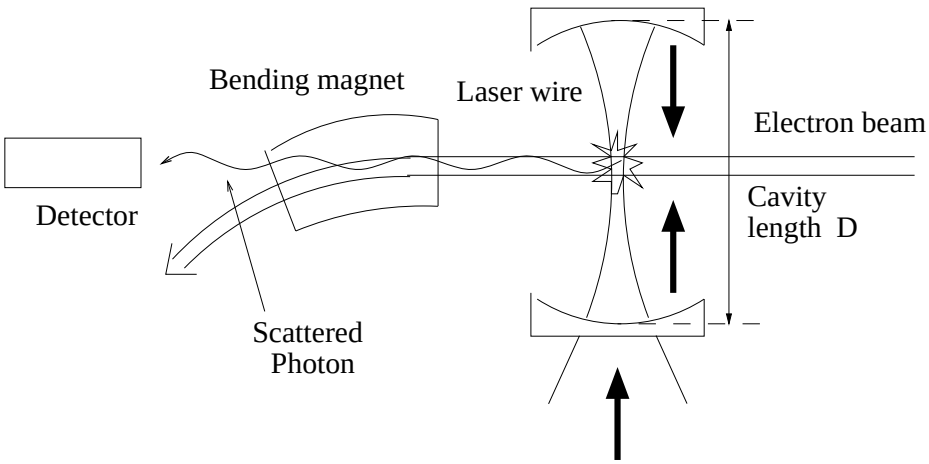

Figure 2.1: Schematic diagram of the laser wire to illustrate measurement principle. An electron beam interacts with the laser and emits energetic photons, which are detected by a detector placed in the forward direction.

The principle of beam size measurements using the laser wire is as follows.

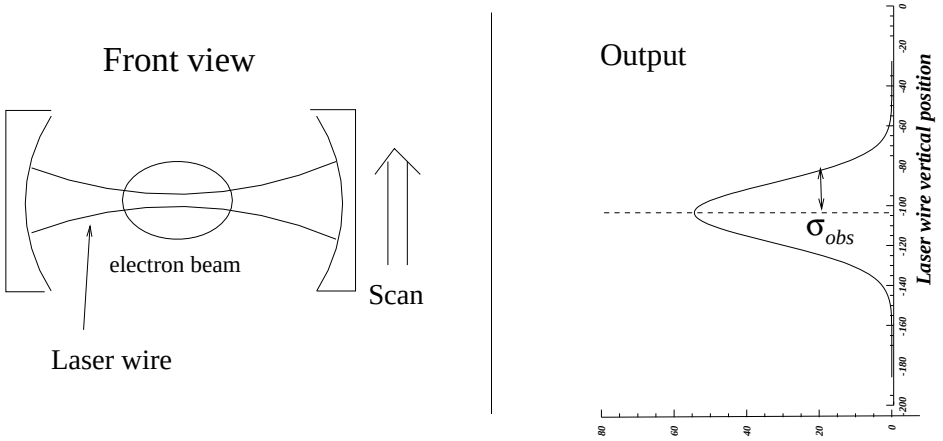

Figure 2.2: Method of beam size measurement. (Left) The front view of the laser wire and the electron beam. The laser will be scanned vertically to obtain the vertical electron beam size. After scanning the laser wire, (Right) Count rate vs the laser wire position.

Suppose we make a stable laser beam and install it perpendicular to an electron beam as shown in Fig.2.1. Electrons interact with the laser light and emit energetic photons in the forward direction by the Compton scattering process. After the scattering, all electrons are bent by a magnet, while emitted photons are detected by a photon detector placed downstream in the forward direction. As shown in Fig.2.2, by scanning the position of the laser beam, a shape of photon counts is obtained. The size of the electron beam can be measured by unfolding a known laser wire width. In particular, if both electron and laser beam are assumed to have gaussian profiles with width σ_y and σ_{lw}, the observed profile is also gaussian with width σ_{obs} expressed by $\sigma_{obs}^2 = \sigma_{lw}^2 + \sigma_y^2$.

We have chosen a CW laser, instead of a pulsed one [1], [2], [3], because it is suited for the quasi-continuous beam of the ATF damping ring. One advantage is that an electron beam size can be measured without considering exact timing of the laser pulse. In addition, intensity of CW lasers are generally more stable ($< 0.5\%$) than pulsed ones.

In the ATF damping ring, the vertical electron beam size is about 10 μm. To measure it precisely, a thin and intense laser beam is required. We utilize a Fabry-Perot optical cavity to fulfill these requirements. There are several advantages in this type of cavity. First, by choosing a nearly concentric configuration, a very thin beam waist can be realized. Second, we can amplify light intensity inside the cavity by making the cavity satisfy a resonance condition. Finally, this type of a cavity allows us to select various

"modes" (intensity distribution) at will; in this particular application, we have chosen the fundermental gauss mode (TEM_{00}).

In the next section, we describe the characteristic of the optical cavity. Two parameters, a beam waist and an enhancement factor, are of special interest. The former characterizes thinness of a laser beam while the latter specifies an amplification factor of intensity inside the cavity. We will explain these two parameters in detail.

2.2 Optical Cavity

2.2.1 Gaussian beam

Before explaining the optical cavity itself, we describe a gaussian beam inside the cavity.

Wave analysis of beams The behavior of laser light is described by an amplitude and a phase. We introduce scalar field $u(\vec{r})$ to represent it. It is known that $u(\vec{r})$ obeys the Helmholtz wave equation [15], [16]:

$$\nabla^2 u(\vec{r}) + k^2 u(\vec{r}) = 0 \qquad (2.1)$$
$$k = \frac{2\pi}{\lambda}$$

Among various solutions, we are interested in a traveling wave, say, in the z direction. In this case, $u(\vec{r})$ is expressed by

$$u(\vec{r}) = \psi(x, y, z) \exp(-ikz), \qquad (2.2)$$

where ψ is a slowly varying complex function. By "slowly", we mean that a fractional change in ψ (and its derivative) in one wave length λ is negligible; $\lambda \left|\frac{\partial \psi(\vec{r})}{\partial z}\right| \ll |\psi(\vec{r})|$, and $\lambda \left|\frac{\partial^2 \psi(\vec{r})}{\partial z^2}\right| \ll \left|\frac{\partial \psi(\vec{r})}{\partial z}\right|$. When these conditions are satisfied, Eq.(2.1) can be rewritten

$$\left(\frac{\partial^2}{\partial x^2} + \frac{\partial^2}{\partial y^2} + 2ik\frac{\partial}{\partial z}\right)\psi(\vec{r}) = 0. \qquad (2.3)$$

This equation is similar to the time dependent *Schrödinger equation*. It is known that one solution can be expressed by

$$\begin{aligned} \psi(\vec{r}) &= \exp\left\{-i\left(p(z)+\frac{k}{2q(z)}r^2\right)\right\}, \qquad (2.4)\\ r^2 &= x^2+y^2,\\ p(z) &: \text{complex phase shift, and}\\ q(z) &: \text{complex beam parameter.} \end{aligned}$$

Inserting Eq.(2.4) into Eq.(2.3), and comparing terms of equal powers in r , we obtain a set of differential equations;

$$\frac{\partial p(z)}{\partial z} = -\frac{i}{q(z)} \quad , \quad \frac{\partial q(z)}{\partial z} = 1$$

$$\text{with solutions,} \qquad q(z) = z + q_0 \quad , \quad p(z) = i\ln\left(1+\frac{z}{q_0}\right) \qquad (2.5)$$

This solution is thus characterized by a single parameter q_0, and is rewritten by [1]

$$q_0 = i\frac{\pi w_0^2}{\lambda}, \qquad (2.6)$$

where λ represents the wave length of light. The parameter w_0 is a beam spot size at $z = 0$ ($\psi(\vec{r}) = \exp(-r^2/w_0^2)$ at $z = 0$). For $z \neq 0$, it is more convenient to introduce two real parameters $R(z)$ and $w(z)$ by

$$\frac{1}{q(z)} = \frac{1}{R(z)} - i\frac{\lambda}{\pi w(z)^2} \qquad (2.7)$$

Inserting Eq.(2.7) into Eq.(2.4), we obtain

$$\psi(\vec{r}) = \exp\left(-ip(z) - i\frac{kr^2}{2R(z)}\right)\exp\left(-\frac{r^2}{w^2(z)}\right) \qquad (2.8)$$

From this equation, we realize that $R(z)$ is a radius of the wave front curvature and $w(z)$ is a beam spot size at z. From Eq.(2.5) and Eq.(2.7) with Eq.(2.6), we obtain

[1] The real part is irrelevant because it only expresses a physically meaningless complex phase.

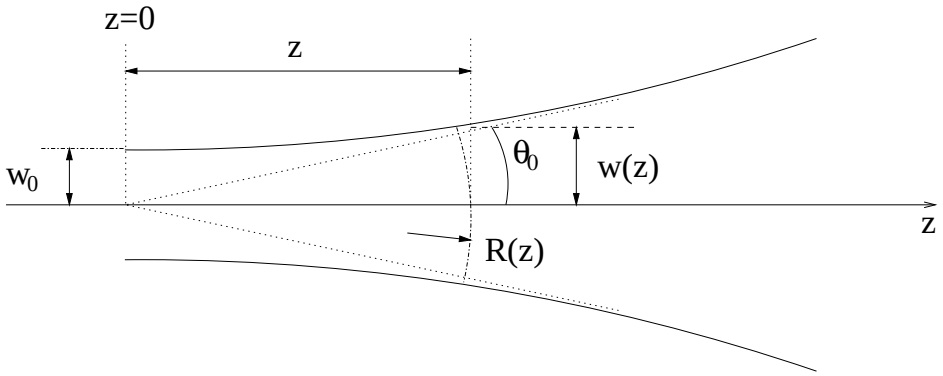

Figure 2.3: Propagation of the gaussian beam. Laser propagates in the z direction. We denote the beam waist at z=0.

$$w(z) = w_0\sqrt{1+\left(\frac{\lambda z}{\pi w_0^2}\right)^2} = w_0\sqrt{1+\left(\frac{z}{z_0}\right)^2} \tag{2.9}$$

$$R(z) = z\left\{1+\left(\frac{\pi w_0^2}{\lambda z}\right)^2\right\} = z\left\{1+\left(\frac{z_0}{z}\right)^2\right\} \tag{2.10}$$

$$z_0 = \frac{\pi w_0^2}{\lambda},$$

where z_0 is called *Reighly length*. The intensity of the beam is represented by

$$|\psi(\vec{r})|^2 = \left(\frac{w_0}{w(z)}\right)^2 \exp\left(-\frac{2r^2}{w^2(z)}\right). \tag{2.11}$$

The width of intensity profile, expressed by $w^2(z)$, takes the form of a hyperbola (See Fig.2.3). As z increases, $w(z)$ approaches to the line defined by $\theta_0 \equiv w_0/z_0$, which is known as *far-field diffraction angle*. At $z = 0$, the beam has the smallest waist w_0 and an infinite curvature (R = ∞). Summing up various expressions derived above, we finally obtain

$$u(\vec{r}) = \frac{w_0}{w(z)}\exp\left\{-i(kz-\Phi(z)) - r^2\left(\frac{1}{w^2(z)}+\frac{ik}{2R(z)}\right)\right\} \tag{2.12}$$

$$\Phi(z) = \arctan\left(\frac{\lambda z}{\pi w_0^2}\right), \tag{2.13}$$

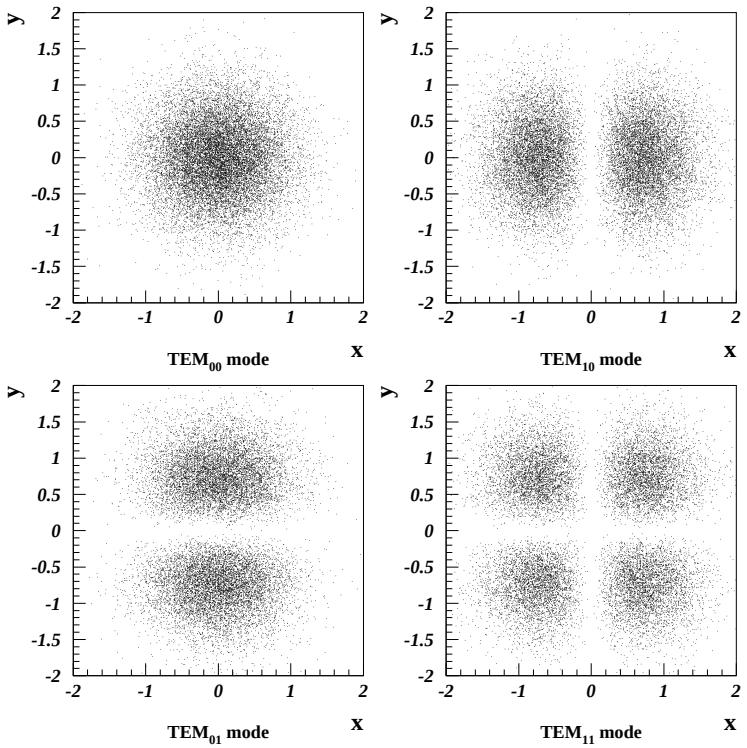

Figure 2.4: Intensity profile of the gauss modes specified at the bottom of each figure.

where $\Phi(z)$ is called *Guoy phase factor*. So far we have analyzed the simplest solution of Eq.(2.3). This solution is often called a fundamental mode of the gaussian beam, and is denoted by TEM_{00}. There are other solutions of Eq.(2.3) with similar properties. We may expand the solutions to the transverse direction. We only show the result here;

$$\begin{aligned} u_{nm}(\vec{r}) &= \frac{w_0}{w(z)} H_m\left(\frac{\sqrt{2}x}{w(z)}\right) H_n\left(\frac{\sqrt{2}y}{w(z)}\right) \\ &\times \exp\left\{-i(kz-(1+m+n)\Phi(z)) - r^2\left(\frac{1}{w^2(z)} + \frac{ik}{2R(z)}\right)\right\} \\ \Phi(z) &= \arctan\left(\frac{\lambda z}{\pi w_0^2}\right), \end{aligned} \tag{2.14}$$

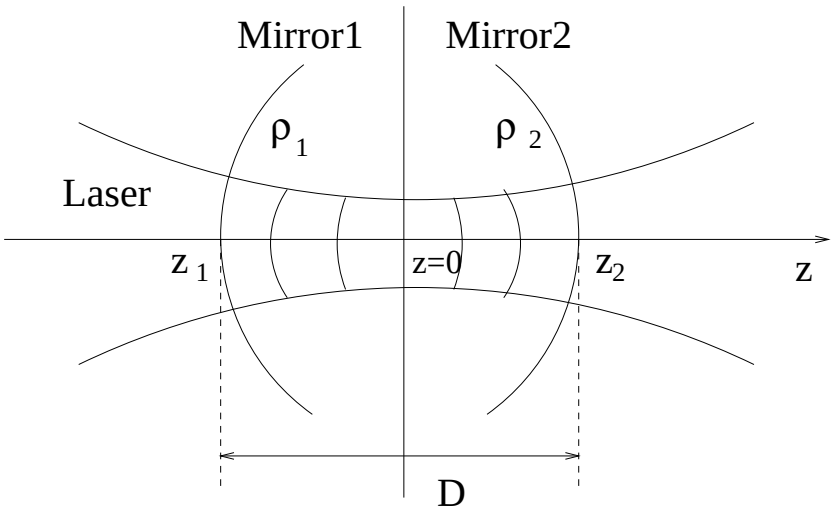

Figure 2.5: Behavior of laser beam propagation inside the cavity. Only when the wave front of the laser beam matches the mirror curvatures, a laser beam with a particular mode is excited in the cavity.

where $H_m(x)$ is the Hermite polynomial of order m. By setting $m = n = 0$, we reproduce the *fundamental mode*. We call Eq.(2.14) *transverse mode* and denote it by TEM_{mn}. Examples of gaussian beam intensity profile at $z = 0$ are shown in Fig.2.4.

Wave analysis of optical cavity Next, we discuss laser beam propagation inside the cavity. Suppose two mirrors with curvatures ρ_1 and ρ_2 are placed at z_1 and z_2, respectively, as shown in Fig.2.5. We denote the cavity length by D ($D = z_1 - z_2$), and define its center to be $z = 0$. As we discussed in the previous paragraph, the wave front of the gaussian beam has a curvature represented by Eq.(2.10). If it exactly matches curvatures of the cavity mirrors, then the beam will propagate back along the same passage to its original point. Thus it will bounce back and forth many times, if mirror's reflectivity is high. Below we will consider precise conditions to realize such situation described above.

First of all, to match the wave front with the mirror's curvature, the following conditions must be satisfied (See Eq.(2.10));

$$\begin{aligned} -\rho_1 &= z_1 + z_0^2/z_1 \\ \rho_2 &= z_2 + z_0^2/z_2 \end{aligned}$$

From equations above, the mirror positions z_1 and z_2 and beam waist w_0 are

shown to satisfy

$$\begin{aligned} z_1 &= \frac{-D(\rho_2 - D))}{\rho_1 + \rho_2 - 2D} \\ z_2 &= \frac{D(\rho_1 - D))}{\rho_1 + \rho_2 - 2D} \\ w_0^2 &= \frac{\lambda}{\pi} \cdot \frac{\sqrt{D(\rho_1 - D)(\rho_2 - D)(\rho_1 + \rho_2 - D)}}{|\rho_1 + \rho_2 - 2D|}. \end{aligned}$$

In particular, if the curvatures are same ($\rho = \rho_1 = \rho_2$), then the beam waist w_0 is deduced to

$$w_0^2 = \frac{\lambda}{\pi} \cdot \frac{\sqrt{D(2\rho - D)}}{2}. \tag{2.15}$$

Fig.2.6 shows the beam waist w_0 as a function of the cavity length D for $2\rho = 40$mm and $\lambda = 532$nm. The expanded view shows w_0 vs D when the cavity is nearly concentric. To realize small w_0, D has to be close to 2ρ. In order to fix w_0 to a specified value, a precise control on D is needed. For example, if $w_0 = 10\mu$m is to be realized with $\rho = 20$mm, then D=39.965mm (See Eq.(2.6)). In this case, the tolerance in D is only 10μm to keep w_0 within 1μm of the desired value.

2.2.2 Enhancement factor

Fig.2.7 shows a schematic diagram of a laser beam injected into a cavity made with two mirrors. At the interface of the mirror 1, a part of the beam will be transmitted with an amplitude t_1, and the rest will be reflected back with an amplitude $-r_1$ [2]. Similarly, at the interface of the mirror 2, t_2 will be transmitted, and r_2 will be reflected. The laser beam trapped inside the cavity will create an infinite number of reflected and transmitted beam, as shown in Fig.2.7. Transmissivity T_i and reflectivity R_i of the mirror i ($i = 1, 2$) are related to t_i and r_i by

$$\begin{aligned} t_i &= \sqrt{T_i} \\ r_i &= \sqrt{R_i} \end{aligned}$$

[2]Several comments are necessary. Amplitudes are normalized to that of the incident beam. The mirrors sign in $-r_1$ is introduced for convenience. If there is some power loss at the surface, then $|t_1|^2 + |r_1|^2 < 1$.

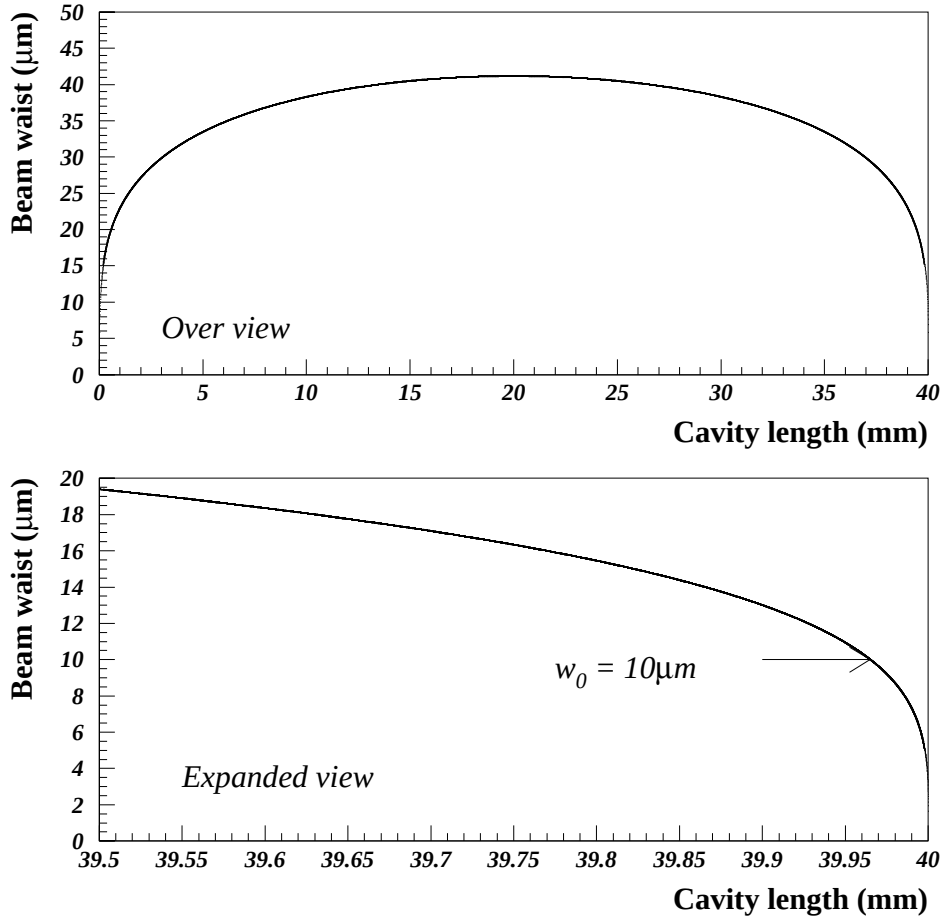

Figure 2.6: (Top) Over view. (Bottom) Expanded view. For $w_0 = 10(\mu\mathrm{m})$, $D = 39.965(\mathrm{mm})$.

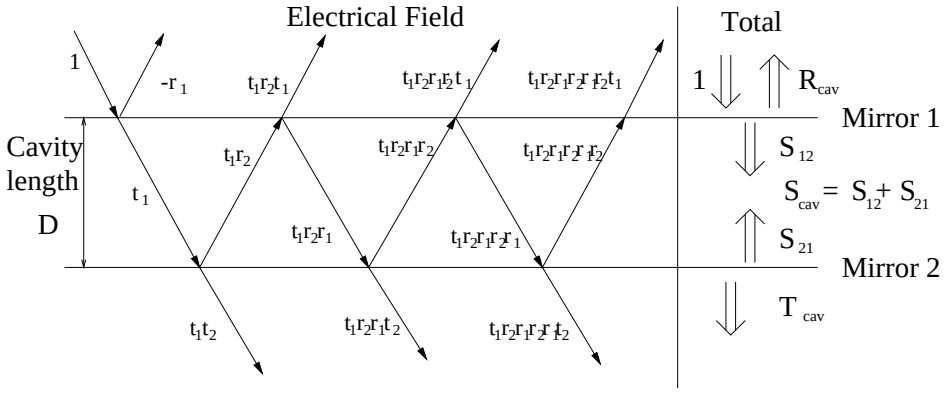

Figure 2.7: Schematic diagram of the optical cavity. Each arrow represents either transmitted or reflected laser beam with specified amplitude. The sum of these amplitudes determines the reflectivity R_{cav}, the transmissivity T_{cav} and the enhancement factor S_{cav} at the cavity. See details in the text.

Denoting absorption of the mirror by A_i, the relation $T_i + R_i + A_i = 1$ holds thanks to power conservation.

We now want to define transmissivity (T_{cav}) and reflectivity (R_{cav}) of the cavity as a whole. Summing up all transmitted and/or reflected waves, we have

$$\begin{aligned}
\sqrt{T_{cav}} &= t_1 t_2 \left[1 + r_1 r_2 e^{i\varphi} + (r_1 r_2 e^{i\varphi})^2 + \cdots\right] \\
&= \frac{t_1 t_2}{1 - r_1 r_2 e^{i\varphi}} \qquad (2.16) \\
\sqrt{R_{cav}} &= -r_1 + t_1 r_2 t_1 e^{i\varphi} \left[1 + r_1 r_2 e^{i\varphi} + (r_1 r_2 e^{i\varphi})^2 + \cdots\right] \\
&= -r_1 + \frac{t_1^2 r_2 e^{i\varphi}}{1 - r_1 r_2 e^{i\varphi}}, \qquad (2.17)
\end{aligned}$$

where φ is the phase advance in one round trip inside the cavity. If we ignore an extra phase at the mirrors, the phase advance φ is represented simply by $\varphi = 2\pi\left(\frac{2D}{\lambda}\right)$. Stored power can be calculated in a similar way. Summing up separately the waves going from 1 to 2 and from 2 to 1, we obtain

$$\begin{aligned}
\sqrt{S_{12}} &= t_1 \left[1 + r_1 r_2 e^{i\varphi} + (r_1 r_2 e^{i\varphi})^2 + \cdots\right] \\
&= \frac{t_1}{1 - r_1 r_2 e^{i\varphi}} \qquad (2.18) \\
\sqrt{S_{21}} &= t_1 r_2 \left[1 + r_1 r_2 e^{i\varphi} + (r_1 r_2 e^{i\varphi})^2 + \cdots\right]
\end{aligned}$$

$$= \frac{t_1 r_2}{1 - r_1 r_2 e^{i\varphi}}, \tag{2.19}$$

where S_{12} and S_{21} represents the stored power from each component. The total power S_{cav} is just the sum of S_{12} and S_{21}; $S_{cav} = S_{12} + S_{21}$. A straightforward calculation leads us from Eq.(2.16), Eq.(2.17), Eq.(2.18) and Eq.(2.19) to

$$T_{cav} = \left| \frac{t_1 t_2}{1 - r_1 r_2 e^{i\varphi}} \right|^2 = \frac{T_1 T_2}{(1 - \sqrt{R_1 R_2})^2 + 4\sqrt{R_1 R_2} \sin^2(\frac{2\pi D}{\lambda})} \tag{2.20}$$

$$\begin{aligned} R_{cav} &= \left| -r_1 + \frac{t_1^2 r_2 e^{i\varphi}}{1 - r_1 r_2 e^{i\varphi}} \right|^2 \\ &= \frac{\left\{ \sqrt{R_1} - \sqrt{R_2}(1 - A_1) \right\}^2 + 4\sqrt{R_1 R_2}\,(1 - A_1) \sin^2(\frac{2\pi D}{\lambda})}{\left(1 - \sqrt{R_1 R_2}\right)^2 + 4\sqrt{R_1 R_2} \sin^2(\frac{2\pi D}{\lambda})} \end{aligned} \tag{2.21}$$

$$\begin{aligned} S_{cav} &= \left| \frac{t_1}{1 - r_1 r_2 e^{i\varphi}} \right|^2 + \left| \frac{t_1 r_2}{1 - r_1 r_2 e^{i\varphi}} \right|^2 \\ &= \frac{T_1 (1 + R_2)}{\left(1 - \sqrt{R_1 R_2}\right)^2 + 4\sqrt{R_1 R_2} \sin^2(\frac{2\pi D}{\lambda})} \end{aligned} \tag{2.22}$$

When the condition $\varphi = 2\pi m$ or $D = m\frac{\lambda}{2}$ (m = integer) is fulfilled, the cavity is said to satisfy the resonance condition. When this is satisfied, both T_{cav} and S_{cav} become large. Fig.2.8 (above) shows T_{cav} as a function of the cavity length D for various parameters of R_i and T_i. The functional form represented by Eq.(2.20), Eq.(2.21) and Eq.(2.22) is referred to as *Airy function*. On resonance, it shows a sharp peak. The distance between two peaks is given by $\Delta D = \frac{\lambda}{2}$, and this quantity is called free spectral range (FSR). Fig.2.8 (bottom) shows R_{cav} and T_{cav} near the resonance condition. On resonance, R_{cav} shows the minimum giving the least reflected power from the cavity while T_{cav} exhibits its maximum.

The FWHM width ($2 \times \delta D$) of these function is given by

$$\frac{1}{2} \times \frac{T_1 T_2}{(1 - \sqrt{R_1 R_2})^2} = \frac{T_1 T_2}{(1 - \sqrt{R_1 R_2})^2 + 4\sqrt{R_1 R_2} \sin^2(\frac{2\pi \delta D}{\lambda})}$$

When δD is much smaller than λ, δD is represented by

$$\delta D = \frac{\lambda}{4\pi} \frac{1 - \sqrt{R_1 R_2}}{(R_1 R_2)^{1/4}} = \frac{\Delta D}{2F},$$

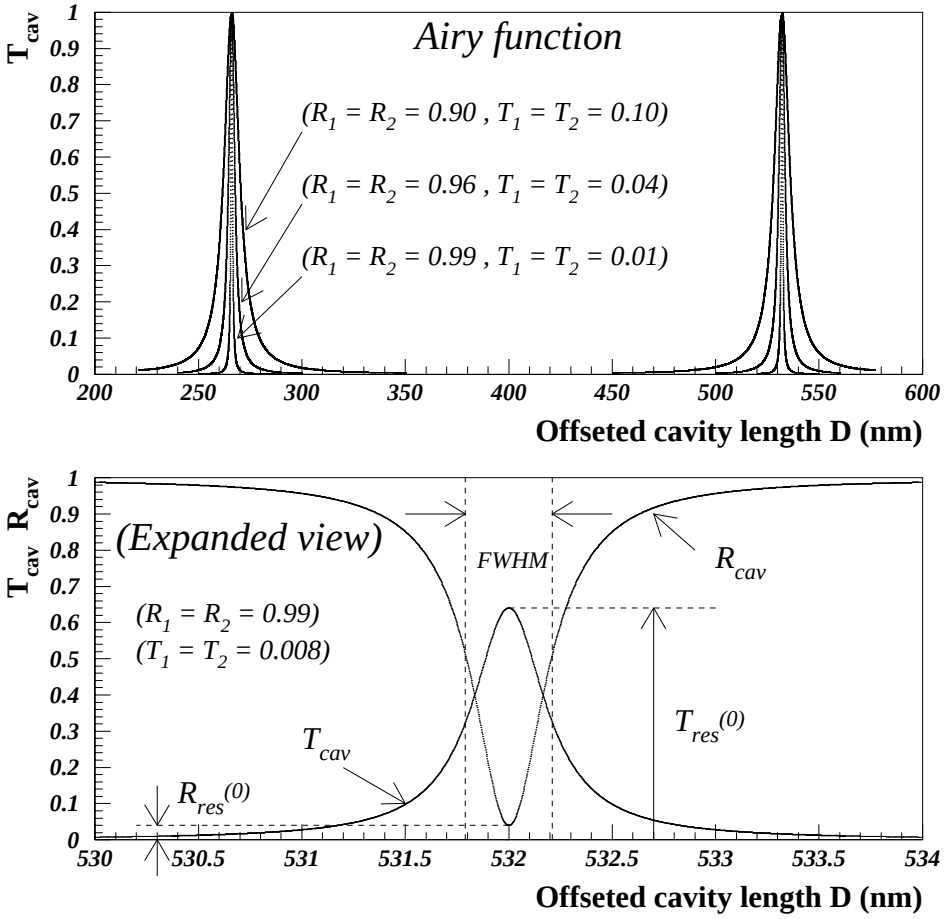

Figure 2.8: Airy functions for transmitted or reflected beam from the cavity. (Top) T_{cav} vs D. Mirror reflectivity R_i and transmissivity T_i are specified in the figure. (Bottom) R_{cav} and T_{cav} vs D near the resonance condition. ($R_1 = R_2 = 0.99$ and $T_1 = T_2 = 0.008$.) $T_{res}^{(0)}$, $R_{res}^{(0)}$ and $FWHM$ determine the enhancement factor $S_{res}^{(0)}$. See details in text.

where the quality F, called *Finesse*, is defined by

$$F \equiv \frac{(FSR)}{(FWHM)} = \frac{\Delta D}{2\delta D} = \frac{\pi (R_1 R_2)^{1/4}}{1 - \sqrt{R_1 R_2}} \tag{2.23}$$

We note that F can be determined experimentally by observing the Airy function of, say, T_{cav}; namely, by measuring ΔD (FSR) and δD (the width of the peak).

We summarize below T_{cav}, R_{cav} and S_{cav} on resonance;

$$T_{res}^{(0)} = \frac{T_1 T_2}{(1 - \sqrt{R_1 R_2})^2} \tag{2.24}$$

$$R_{res}^{(0)} = \frac{\left\{\sqrt{R_1} - \sqrt{R_2}(1 - A_1)\right\}^2}{\left(1 - \sqrt{R_1 R_2}\right)^2} \tag{2.25}$$

$$S_{res}^{(0)} = \frac{T_1 \left(1 + R_2\right)}{\left(1 - \sqrt{R_1 R_2}\right)^2} \tag{2.26}$$

When we use identical mirrors with 99% reflectivity ($R_1 = R_2 = 0.99$) and no absorption, then $T_{res}^{(0)} = 1$, $R_{res}^{(0)} = 0$, $S_{res}^{(0)} \simeq 200$ and $F = 313$. In practice, however, we cannot neglect the absorption of the mirrors. Then $T_{res}^{(0)} < 1$, $R_{res}^{(0)} > 0$ as shown in the bottom figure of Fig.2.8. By measuring $T_{res}^{(0)}$, $R_{res}^{(0)}$ and F, we can determine the enhancement factor $S_{res}^{(0)}$.

2.3 Estimation of Count rate

2.3.1 Kinematics

In this section, we calculate an expected energy spectrum of emitted photons by the Compton scattering. Fig.2.9 shows the Compton kinematics in our experimental configuration. Here a laser photon with an energy k_0 is assumed to come perpendicular to an electron beam with an energy E_0. We denote the incident electron and the photon direction by z and x, respectively, and the other direction by y. After interaction, the scattered photon with an energy k_s will go into the direction of an polar angle θ and an azimuthal angle ϕ. Similarly, the scattered electron with an energy E_s will go into θ_e and ϕ_e. The four vector of the incident electron, incident photon, scattered

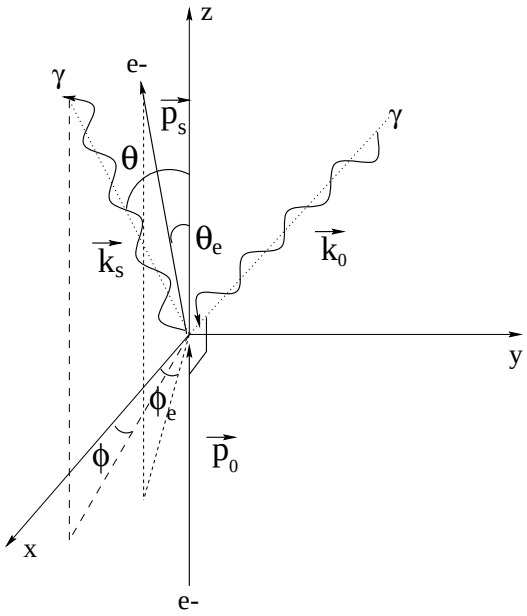

Figure 2.9: Compton scattering kinematics in our experimental configuration.

electron and scattered photon are defined by $\vec{P_0}, \vec{k_0}, \vec{P_s}$ and $\vec{k_s}$, respectively, and are expressed by

$$\vec{P_0} = \begin{pmatrix} E_0 \\ 0 \\ 0 \\ P_0 \end{pmatrix}, \quad \vec{k_0} = \begin{pmatrix} k_0 \\ k_0 \\ 0 \\ 0 \end{pmatrix}, \quad \vec{P_s} = \begin{pmatrix} E_s \\ P_s \cos\phi_e \sin\theta_e \\ P_s \sin\phi_e \sin\theta_e \\ P_s \cos\theta_e \end{pmatrix}, \quad \vec{k_s} = \begin{pmatrix} k_s \\ k_s \cos\phi \sin\theta \\ k_s \sin\phi \sin\theta \\ k_s \cos\theta \end{pmatrix},$$

$$\begin{cases} E_0^2 &= P_0^2 + {m_e}^2 \\ E_s^2 &= P_s^2 + {m_e}^2 \end{cases} \tag{2.27}$$

where m_e denotes the electron mass. We obtain the relations below:

$$\begin{cases} E_0 + k_0 &= E_s + k_s \\ k_0 &= P_s \cos\phi_e \sin\theta_e + k_s \cos\phi \sin\theta \\ 0 &= P_s \sin\phi_e \sin\theta_e + k_s \sin\phi \sin\theta \\ P_0 &= P_s \cos\theta_e + k_s \cos\theta \end{cases} \tag{2.28}$$

From Eq.(2.27) and Eq.(2.28), the energy of the scattered photon k_s is given by

$$k_s = \frac{k_0 E_0}{E_0 + k_0 - \sqrt{E_0^2 - {m_e}^2}\cos\theta - k_0 \sin\theta \cos\phi} \tag{2.29}$$

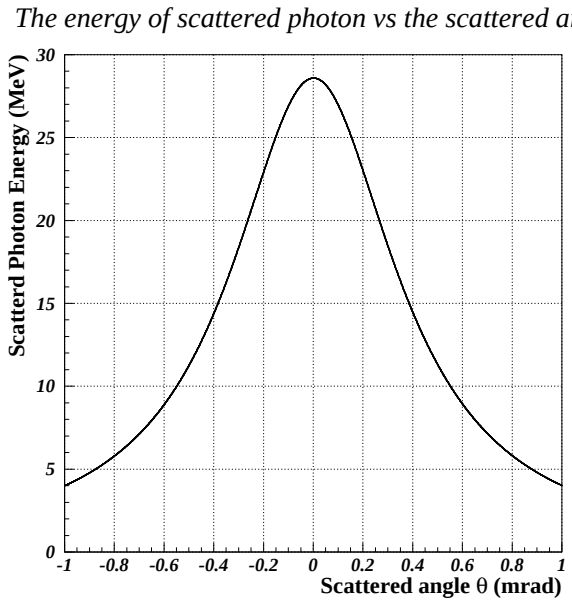

Figure 2.10: Scattered photon energy k_s vs the scattering angle θ. The maximum energy of 28.6 MeV is obtained at θ =0.

In principle, k_s depends upon both θ (hereafter referred to as a scattering angle) and ϕ. In practice, however, ϕ can be neglected, because the incident electron energy E_0(=1.28GeV) is much larger than the incident photon energy k_0 ($E_0 \gg k_0$). The energy k_s is plotted in Fig.2.10 as a function of θ for a green laser ($\lambda = 532$nm).

2.3.2 Differential cross section

Next, we calculate the differential cross section in a laboratory system. In order to calculate the cross section, we consider Lorenz boost between the laboratory and electron rest frame. As explained in the Sec.2.3.1, we can ignore the azimuthal angle ϕ. Thus we only consider the polar angle θ in the Lorenz boost. Fig.2.11 shows the kinematical variables both in the laboratory and electron rest frame. In this section, we use the following coordinate system. The x direction is defined by the incident electron, and the y direction is defined by the incident photon. The four vectors are expressed by

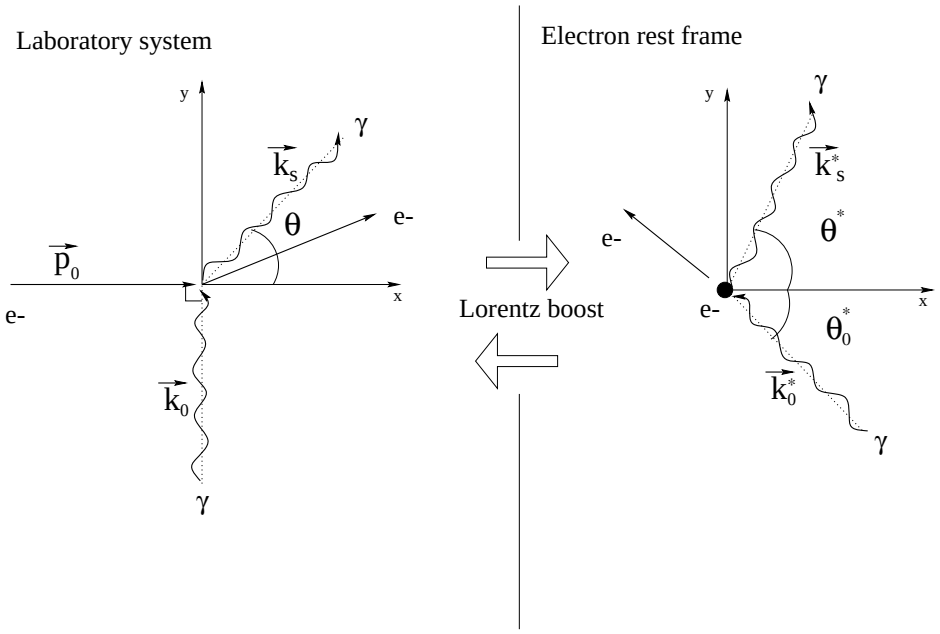

Figure 2.11: Lorenz boost between the laboratory system and electron rest frame.

$$\vec{P_0} = \begin{pmatrix} E_0 \\ P_0 \\ 0 \\ 0 \end{pmatrix}, \quad \vec{k_0} = \begin{pmatrix} k_0 \\ 0 \\ k_0 \\ 0 \end{pmatrix}, \quad \vec{k_s} = \begin{pmatrix} k_s \\ k_s \cos\theta \\ k_s \sin\theta \\ 0 \end{pmatrix}$$

$$E_0^2 = P_0^2 + {m_e}^2$$

Similarly, the four vectors for the incident and scattered photons in the electron rest frame are denoted by $\vec{k_0^*}$, $\vec{k_s^*}$, and are expressed by

$$\vec{k_0^*} = \begin{pmatrix} k_0^* \\ k_0^* \cos\theta_0^* \\ k_0^* \sin\theta_0^* \\ 0 \end{pmatrix}, \quad \vec{k_s^*} = \begin{pmatrix} k_s^* \\ k_s^* \cos\theta^* \\ k_s^* \sin\theta^* \\ 0 \end{pmatrix},$$

where θ_0^*, θ^* are the polar angles of incident and scattered photons, respectively. Hereafter, physics quantities with an asterisk are those in the electron rest frame. From the Lorenz transformations, $\vec{k_0^*}$ is given by

$$\vec{k_0^*} = \begin{pmatrix} \gamma_e & -\gamma_e\beta_e & 0 & 0 \\ -\gamma_e\beta_e & \gamma_e & 0 & 0 \\ 0 & 0 & 1 & 0 \\ 0 & 0 & 0 & 1 \end{pmatrix} \vec{k_0} = \begin{pmatrix} \gamma_e k_0 \\ -\gamma_e\beta_e k_0 \\ k_0 \\ 0 \end{pmatrix}$$

$$\begin{cases} \gamma_e &= E_0/m_e \\ \beta_e &= P_0/E_0 \end{cases}$$

In this configuration, $\vec{k_0^*} = \begin{pmatrix} k_0^* \\ k_0^*\cos\theta_0^* \\ k_0^*\sin\theta_0^* \\ 0 \end{pmatrix}$. Now we obtain the relations;

$$\begin{cases} k_0^* &= \gamma_e k_0 \\ \theta_0^* &= -\arctan(1/\gamma_e\beta_e) \end{cases}$$

Similarly, from the Lorenz transformation between $\vec{k_s^*}$ and $\vec{k_s}$, we obtain the relations of polar angles;

$$\cos\theta^* = \frac{\cos\theta - \beta_e}{1 - \beta_e\cos\theta}. \tag{2.30}$$

In the electron rest frame, the differential cross section of the Compton scattering process is given by *Klein-Nishina formula* [18]. If electrons and photons are not polarized, this formula is expressed by

$$\begin{cases} \dfrac{d\sigma_{comp}}{d\Omega^*} &= \dfrac{r_0^2}{2}(\dfrac{k_s^*}{k_0^*})^2 \left\{ \dfrac{k_s^*}{k_0^*} + \dfrac{k_0^*}{k_s^*} - \sin^2(\theta^* + \theta_0^*) \right\} \\ k_s^* &= \dfrac{m_e k_0^*}{m_e + (1+\cos(\theta^*+\theta_0^*))k_0^*} \end{cases} \tag{2.31}$$

where $d\Omega^*$ is the solid angle and r_0 is the classical electron radius. The differential cross section $\left(\dfrac{d\sigma_{comp}}{d\Omega}\right)$ in the laboratory system can be related to $\left(\dfrac{d\sigma_{comp}}{d\Omega^*}\right)$ by

$$\frac{d\sigma_{comp}}{d\Omega} = \frac{d\sigma_{comp}}{d\Omega^*} \cdot \frac{d\Omega^*}{d\Omega} = \frac{d\sigma_{comp}}{d\Omega^*} \cdot \frac{d(\cos\theta^*)}{d(\cos\theta)} \tag{2.32}$$

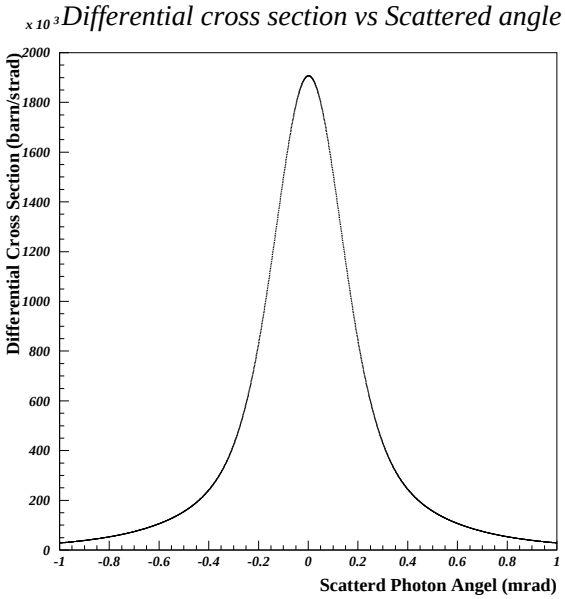

Figure 2.12: The differential cross section $\frac{d\sigma_{comp}}{d\Omega}$ in the laboratory system.

From Eq.(2.30), Eq.(2.31) and Eq.(2.32) [3], we finally arrive at

$$\frac{d\sigma_{comp}}{d\Omega} = \frac{1}{2} r_0^2 (\frac{k_s^*}{k_0^*})^2 \left\{ \frac{k_s^*}{k_0^*} + \frac{k_0^*}{k_s^*} - \sin^2(\theta^* + \theta_0^*) \right\} \frac{1}{\gamma_e^2 (1 - \beta_e \cos\theta)^2} \qquad (2.33)$$

$$\begin{cases} k_0^* &= \gamma_e k_0 \\ \cos\theta^* &= \frac{\cos\theta - \beta_e}{1 - \beta_e \cos\theta} \\ k_s^* &= \frac{m_e k_0^*}{m_e + (1 + \cos(\theta^* + \theta_0^*)) k_0^*} \\ \theta_0^* &= -\arctan(1/\gamma_e \beta_e) \end{cases}$$

Fig.2.12 shows the differential cross section as a function of θ in the laboratory system. It is found from Fig.2.12 that Eq.(2.33) is almost symmetric function of θ, because in electron rest frame the considerable region of θ^* is much greater than $\theta_0^* \sim \frac{1}{\gamma_e}$. We note that most of photons are emitted in the direction of the incident electron; for example, the cross section with photons above 23MeV ($\theta < 0.2$mrad) is 160mb, which should be compared with the total cross section of 651mb.

[3]The azimuthal angle was ignored in our configuration

2.3.3 Count rate

In this subsection, we calculate an expected count rate of scattered photons [19].

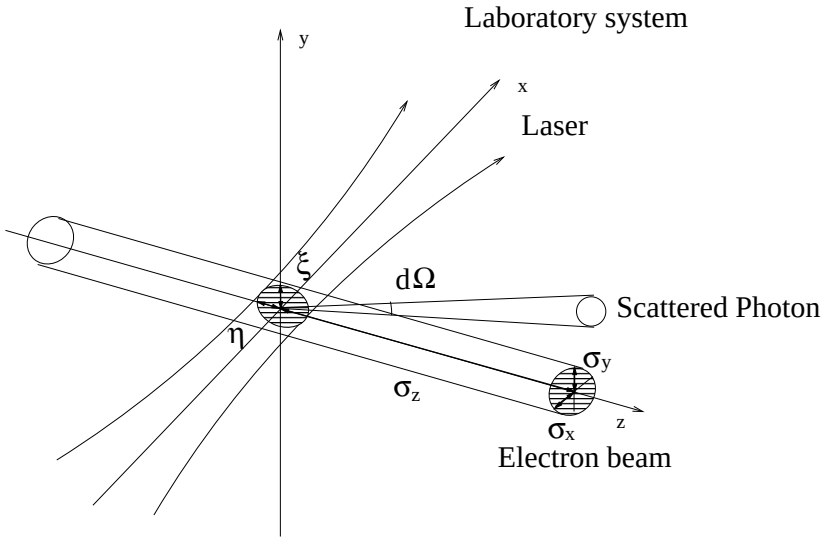

Figure 2.13: Schematic diagram showing the laser wire and electron beam profile and the coordinate system used in the calculation.

Fig.2.13 shows the schematic diagram of the laser wire and electron beam. We assume that intensity distributions ρ_e and ρ_l of the electron and laser beam are gaussian, and are expressed by

$$\begin{cases} \rho_e &= \dfrac{1}{(2\pi)^{3/2}} \dfrac{N_e}{\sigma_x \sigma_y \sigma_z} \exp\left\{ -\dfrac{1}{2}\left(\dfrac{x^2}{\sigma_x^2} + \dfrac{y^2}{\sigma_y^2} \right) - \dfrac{(z-\beta_e ct)^2}{2\sigma_z^2} \right\} \\ \rho_l &= \dfrac{W}{ck_0} \dfrac{1}{2\pi\xi\eta} \exp\left\{ -\dfrac{1}{2}\left(\dfrac{y^2}{\xi^2} + \dfrac{z^2}{\eta^2} \right) \right\} \end{cases} \tag{2.34}$$

Here σ with suffixes of x, y and z stands for the beam size $(1/\sqrt{e})$ of the electron in each direction. ξ and η are the laser beam size in y and z direction, respectively. For the TEM_{00} gauss mode, the relation $\xi = \eta = w_0/2$ holds. N_e denotes the number of electrons per bunch. W is wattage of the laser (inside the optical cavity), and the photon energy is represented by k_0. For simplicity, we assume the incident electron has only z momentum component. Similarly, the incident photon (laser) has only x momentum component; this can be justified by the fact the Reighly length is much larger than the electron beam width σ_x. The count rate of scattered photons per bunch per solid angle is given by

$$\frac{dN_{bunch}}{d\Omega} = \underbrace{c\int\int\int\int_{-\infty}^{+\infty} \rho_e \rho_l \, dx \, dy \, dz \, dt}_{L} \cdot \frac{d\sigma_{comp}}{d\Omega} \tag{2.35}$$

The factor L with $\frac{d\sigma_{comp}}{d\Omega}$ is referred as Luminosity, and is given by

$$\begin{aligned} L &= \frac{N_e W}{(2\pi)^{5/2} k_0 \xi \eta \sigma_x \sigma_y \sigma_z} \\ &\times \int\int\int\int_{-\infty}^{+\infty} \exp\left\{-(C_1\, x^2 + C_2\, y^2 + C_3\, z^2 + C_4\, zt + C_5\, t^2)\right\} dx\, dy\, dz\, dt \end{aligned} \tag{2.36}$$

$$\begin{cases} C_1 = \frac{1}{2\sigma_x^2}, \quad C_2 = \frac{1}{2}\left(\frac{1}{\sigma_y^2} + \frac{1}{\xi^2}\right), \quad C_3 = \frac{1}{2}\left(\frac{1}{\sigma_z^2} + \frac{1}{\eta^2}\right), \\ C_4 = -\frac{\beta_e c}{\sigma_z^2}, \quad C_5 = \frac{\beta_e^2 c^2}{2\sigma_z^2} \end{cases}$$

Integrating Eq.(2.36), we obtain

$$L = \frac{N_e W}{\sqrt{2\pi} k_0 c \beta_e \sqrt{\sigma_y^2 + \xi^2}} \tag{2.37}$$

It is convenient to change Eq.(2.35) into a different form. The differential count rate per second per unit energy of scattered photons is

$$\frac{dN}{dk_s} = f_{rev} \frac{dN_{bunch}}{d\Omega} \frac{d\Omega}{dk_s}, \tag{2.38}$$

where f_{rev} represents a revolution frequency of the electron beam in the ATF damping ring ($f_{rev} = 2.16$ MHz). Fig.2.14 shows the differential count rate. In this calculation we used the following numerical values; $E_0 = 1.28$ GeV, $N_e = 10^{10}$, $\sigma_y = 10\mu$m, $k_0 = 2.33$eV (green: $\lambda = 532$nm), W=10W, $\xi = w_0/2 = 5\mu$m. As will be explained in detail in the next section, we installed in the actual setup a collimator with a circular bore to enhance signal-to-noise ratio. The actual bore size corresponds to $\theta < 0.2$ mrad(θ_{th}); this in turn corresponds to $k_s > 23$MeV. This limit is indicated by a dotted line in Fig.2.14. The total count rate above the line is estimated to be 1.1kHz.

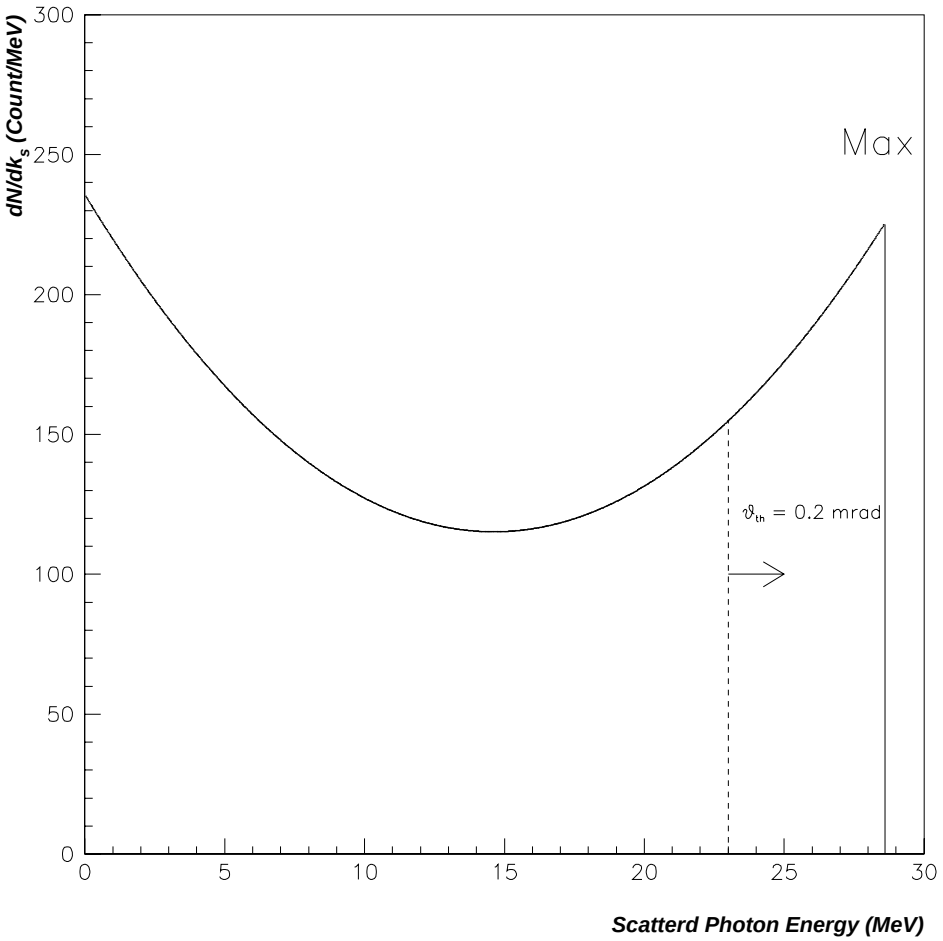

Figure 2.14: Differential count rate dN/dk$_s$ as a function of scattered photon energy k_s. Total count rate above θ_{th} (k_s >23MeV) is estimated to be 1.1kHz.

Chapter 3

Experiments

The experimental setup, shown in Fig.3.1, consists of two main components: a laser wire and a photon detector system. The laser wire system was installed at the north straight section of the ATF damping ring. It was mounted on a movable table, directing the wire perpendicular to the electron beam. The table was moved vertically to measure the vertical emittance. A picture viewing the laser wire setup is shown in Fig.3.2. Scattered photons were detected by a rectangular ($50 \times 50 \times 100$ mm^3) scintillator made of a pure CsI crystal. The location of the detector was 12.8 m downstream of the cavity.

In this chapter, we describe the experimental setup in detail. In Sec.3.1, we describe the ATF damping ring briefly. Then we explain the laser wire system in detail. In Sec.3.3, we describe the photon detector system. We discuss the alignment method of the damping ring in the following section. Finally we discuss about data taking logic for measurements.

3.1 ATF damping ring

3.1.1 Optics

First we explain the optics of the ATF damping ring. Fig.3.3 shows calculated values of the β function and dispersion function around the damping ring. The plot above shows the β function. The horizontal axis is the position of the ring and the vertical axis shows the square root of the β function. The plot below shows the dispersion function (η_x). The bottom figure shows the layout of the magnets. Neither calculation for β nor η includes magnet alignment errors.

The laser wire system was installed in the straight section between QM14R

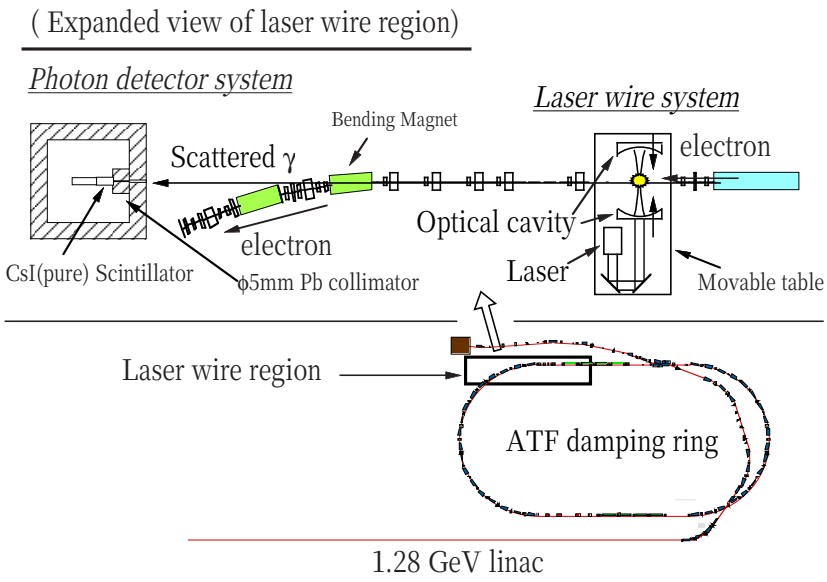

Figure 3.1: Experimental setup of the laser wire. The laser wire system is installed at the north straight section of the ATF damping ring.

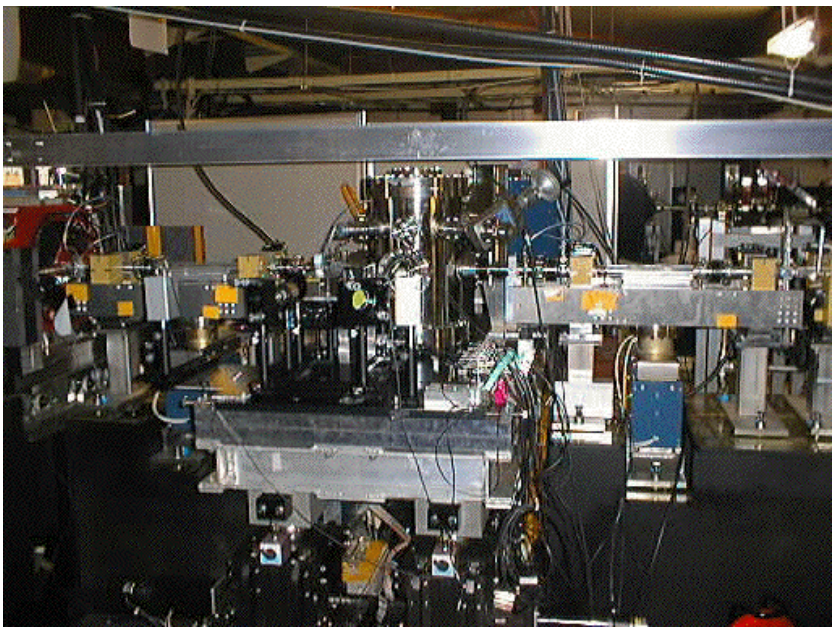

Figure 3.2: Picture of the laser wire system

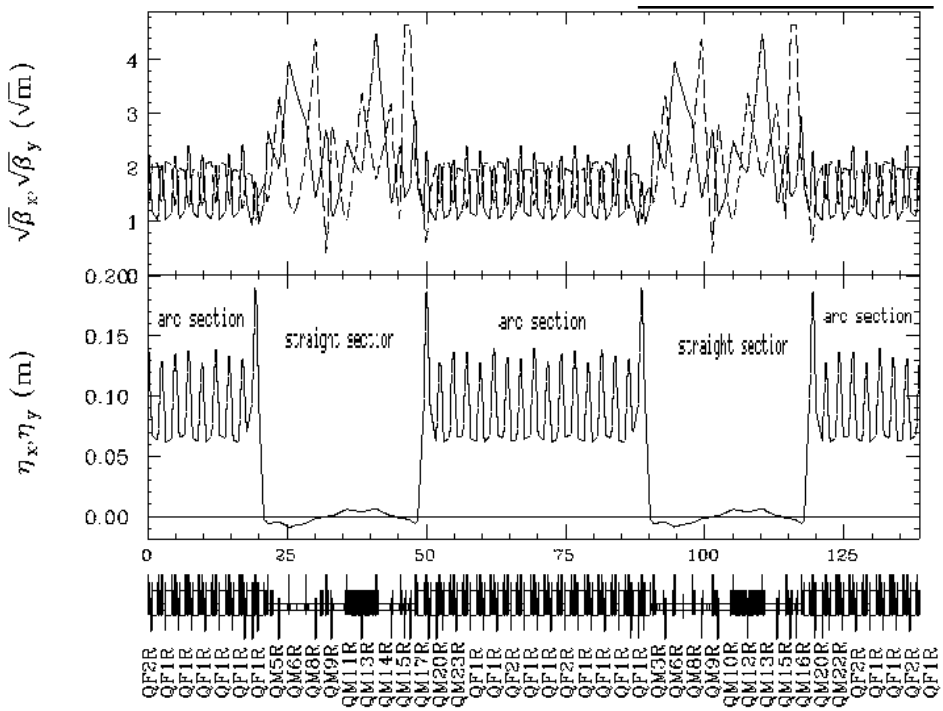

Figure 3.3: Optics of the damping ring. (Top) the square root of the β function. Solid (dashed) line shows the horizontal (vertical) β function. (Mid) the dispersion function (η_x). (Bottom) the lattice of the damping ring. Horizontal axis shows the position of the damping ring (m).

and QM15R. There are two merits to install the setup in a straight section. First β function at a straight section is larger than that of an arc section. This results in a larger beam size since emittance is constant (conserved) around the ring. A larger beam size will make measurement easier. Second, the dispersion at a straight section is much smaller than that of an arc section. As shown in Eq.(1.4), the beam size in the ring depends also upon beam's momentum dispersion. We can neglect this contribution if the dispersion function is small. Thus we determined to install the laser wire at the straight section. We should point out one demerit at the straight section; backgrounds (photons associated with an electron beam) are severe. It took us some time to overcome this problem.

3.1.2 Beam monitor

In order to measure the beam condition, various beam monitors are installed in the ATF damping ring. In this section we describe beam monitors

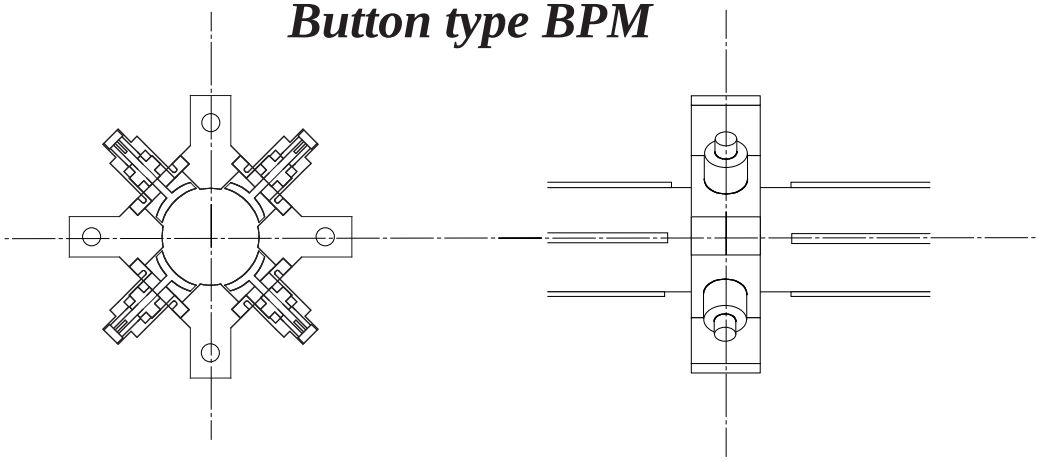

Figure 3.4: Schematics of the button type beam position monitor. (Left) the front view. Four electrodes are shown. (Right) the side view.

used in this experiment.

DC Current Transformer (DCCT) A DC current transformer (DCCT) is utilized to measure an electron beam current in the ATF damping ring. DCCT is made of a torus ferromagnetic material. If electrons pass through this torus, magnetic field is induced inside the ferromagnetic material and the induced signal can be picked up by a winding wire around this material. It is an essential monitor which can measure the absolute number of circulating electrons. The accuracy is measured to be $< 0.1\%$.

Beam Position Monitor (BPM) In order to monitor beam orbit, a device, called beam position monitor (BPM), is used in the ATF damping ring. Fig.3.4 shows a structure of the BPM schematically. They are button type electrodes sandwiching the beam passing through BPM. When electrons go through BPM, they induce mirror charges on the electrodes. The induced charge depends upon distance between the electron beam and electrodes. The average position of the beam can be represented by

$$x' = S_{x'}\frac{I_1 - I_3}{I_1 + I_3} \tag{3.1}$$

$$y' = S_{y'}\frac{I_2 - I_4}{I_2 + I_4}, \tag{3.2}$$

where x' and y' are the transverse coordinates associated with BPM, and I_i's are induced charges on the i-th electrode. (I_1 and I_3 make one pair facing

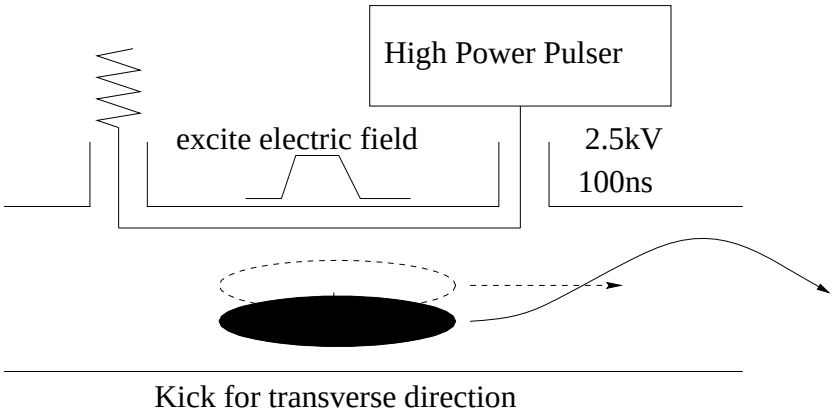

Figure 3.5: Schematic diagram of the beam exciter.

each other, and I_2 and I_4 make another pair.) The coefficients S'_x and S'_y are sensitivity of the monitor, and are determined by a separate calibration measurement on a test bench. The actual signals are read by ADC through a clipping circuits [20]. The position resolution of BPMs is typically 30μm for bunch population of 5×10^9 electrons. (See details in Ref. [20].) There are 96 BPMs installed in the ATF damping ring.

Beam exciter In order to determine emittance of the beam, we need to know the β-function. This in turn requires measurement of tune ν_x and ν_y. These are measured by observing transverse vibration frequency when an impulse perturbation is given to a beam. In practice, the electron beam is kicked by an apparatus called beam exciter in the transverse direction. Fig.3.5 shows a schematic diagram of the beam exciter. Excited electric field kicks the beam horizontally and/or vertically. Then the beam position is recorded every turn until the beam position becomes stable. Beam tune (ν_x, ν_y) can be obtained by Fourier analysis of the beam position vibration. Accuracy of the tune measurement is estimated to be $\sim 0.1\%$

3.1.3 Measurement method of β function

To evaluate the vertical emittance, we need to know the β function at the laser wire. In this subsection, we will present briefly its measurement method (See Appendix A for detail).

Motion of a beam in the ring is described by a matrix called transfer matrix. Given particle's displacement $y(s_1)$ from the central orbit and its direction $y'(s_1) = \frac{dy}{ds}(s_1)$ at $s = s_1$, it predicts those at $s = s_2$:

$$\begin{pmatrix} y(s_2) \\ y'(s_2) \end{pmatrix} = M(s_2, s_1) \begin{pmatrix} y(s_1) \\ y'(s_1) \end{pmatrix}, \tag{3.3}$$

where s denotes the position along the central orbit. A similar equation holds for the other coordinate x with a different transfer matrix. (Here, we have assumed that x and y motions are independent each other. This is approximately true for the ATF damping ring if it is well tuned. Thus we retain this assumption throughout this chapter.) It is known that the transfer matrix of one cycle C, starting from $s = s_0$ and ending at the same point, is expressed by

$$M(s_0, s_0 + C) = \begin{pmatrix} \cos 2\pi\nu_0 + \alpha(s_0) \cdot \sin 2\pi\nu_0 & \beta(s_0) \cdot \sin 2\pi\nu_0 \\ -\gamma(s_0) \cdot \sin 2\pi\nu_0 & \cos 2\pi\nu_0 - \alpha(s_0) \cdot \sin 2\pi\nu_0 \end{pmatrix},$$

where α, β, γ are called twiss parameters, and are determined by a lattice of the ring. The parameter ν_0 represents a phase advance of particle's transverse motion, and is referred to as "tune".

Now let's suppose that one of the quadrupole strength is changed from K to $K + \Delta K$. Suppose also its center position is $s = s_0$. This change is equivalent to adding a thin quadrupole at $s = s_0$ with a transfer matrix $\begin{pmatrix} 1 & 0 \\ \Delta K & 1 \end{pmatrix}$. Thus the new matrix is given by

$$M'(s_0, s_0 + C) \simeq M(s_0, s_0 + C) \begin{pmatrix} 1 & 0 \\ \Delta K & 1 \end{pmatrix} \tag{3.4}$$

$$= \begin{pmatrix} \cos\mu_0 + (\alpha(s_0) + \beta(s_0)\Delta K) \cdot \sin\mu_0 & \beta(s_0) \cdot \sin\mu_0 \\ \Delta K \cdot \cos\mu_0 - (\gamma(s_0) + \alpha(s_0)\Delta K) \cdot \sin\mu_0 & \cos\mu_0 - \alpha(s_0) \cdot \sin\mu_0 \end{pmatrix}$$

We have introduced a parameter μ_0 defined by $\mu_0 = 2\pi\nu_0$. On the other hand, the new matrix $M'(s_0, s_0 + C)$ should be expressed by new twiss parameters and a new tune ν ($\mu = 2\pi\nu$):

$$M'(s_0, s_0 + C) \equiv \begin{pmatrix} \cos\mu + \alpha'(s_0) \cdot \sin\mu & \beta'(s_0) \cdot \sin\mu \\ -\gamma'(s_0) \cdot \sin\mu & \cos\mu - \alpha'(s_0) \cdot \sin\mu \end{pmatrix} \tag{3.5}$$

Eq.(3.4) and Eq.(3.5) must be same. Thus we obtain, taking the trace of the matrix,

$$\cos\mu = \cos\mu_0 + \frac{1}{2}\beta(s_0) \cdot \Delta K \sin\mu_0 \tag{3.6}$$

This is the basic equation used in measuring the β-function. It indicates that, if we can measure μ on the left side of Eq.(3.6) for various ΔK, then we can determine $\beta(s_0)$ and μ_0 on the right hand side. The measurement of μ or ν is carried out by observing beam's transverse position with BPMs when an impulse perturbation is given by the beam exciter. Actual measurements and their results will be described in Sec.4.3.

3.1.4 Production of the low emittance beam

In an ideal case, beam emittance is determined by a lattice of a ring. This is approximately true for the horizontal emittance in ATF damping ring. However, the vertical emittance, which is much smaller than the horizontal one, is actually dominated by residial dispersion and/or x-y betatron coupling arising from misalignment of magnets. (See details in Appendix A) Thus, a low emittance beam, it is important to reduce these effects as much as possible. We will explain actual ring tuning procedures below [21].

At first, a beam orbit was measured with the 96 BPMs. If it did not go through the center of the ideal orbit, it is corrected with steering magnets. After the correction, the beam orbit settled down to within 1mm (2mm) of the ideal orbit vertically (horizontally).

Next we decreased the vertical dispersion function. We begin with explaining how to measure the dispersion function. In a storage ring, an equilibrium energy of the circulating beam is determined by a frequency of a RF source, which compensates the energy loss due to synchrotron radiation. When the RF frequency f_{RF} is altered, the relation between fractional changes in momentum and frequency is given by

$$\frac{\Delta p}{p} = -\frac{1}{\alpha_M}\frac{\Delta f_{RF}}{f_{RF}}, \tag{3.7}$$

where α_M is a momentum compaction factor. On the other hand, since the dispersion function is defined by

$$\Delta y = \eta_y \frac{\Delta p}{p}, \tag{3.8}$$

we obtain

$$\eta_y = -\alpha_M f_{RF}\frac{\Delta y}{\Delta f_{RF}}. \tag{3.9}$$

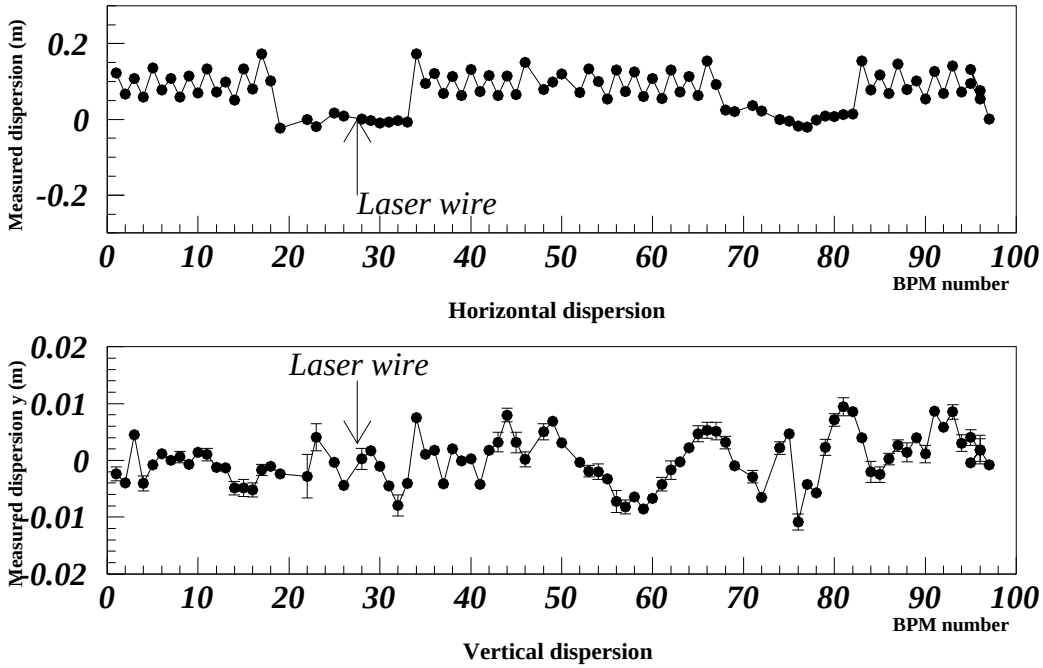

Figure 3.6: Measurement of dispersion after dispersion correction. (Top) the horizontal dispersion function. (Bottom) the vertical dispersion function. Horizontal axis shows the BPM number.

A similar relation holds for x.

Actually, displacement of the beam orbit for five frequency changes Δf_{RF} (+6kHz, +3kHz, 0kHz, -3kHz, -6kHz) was measured by the BPMs. Having determined η_y from Eq.(3.9), we then calculated a new orbit with smaller η_y by adjusting the steering magnets. This procedure was done with an aid of a computer code named SAD [22]. Fig.3.6 shows the measured horizontal and vertical dispersion functions after the correction. The vertical dispersion function could be set within $\pm$ 10mm peak to peak. In particular, at the laser wire, the vertical dispersion function decreased to $\pm$ 2mm.

Finally we applied correction by a skew corrector. If we have a x-y betatron coupling, the vertical emittance would be influenced by the large horizontal emittance. The skew corrector consists of small trim coils on main sextupole magnets. This magnetic field allows the electron beam to tilt transversely. To evaluate the x-y betatron coupling, we use two horizontal steering magnets which differs 90 degree in the betatron phase. If the ideal beam orbit is realized, the vertical beam orbit has no response to the change in the horizontal beam orbit. In practice, however, we usually see some response. To quantify the response, we use the following quantity, named response ratio:

$$\text{response ratio} \equiv \sqrt{\frac{\sum_{N_{steer}} \left(\frac{\sum_{BPM} \Delta y^2}{\sum_{BPM} \Delta x^2} \right)}{N_{steer}}}, \tag{3.10}$$

where N_{steer} is number of steering magnets and Δx and Δy are the observed displacements. In this case, $N_{steer} = 2$. The strategy of the skew correction is to reduce this response ratio by the skew correctors. After skew correction, we could reduce it from 8% to 4 % typically. Its achievable value is limited by the BPM resolution at present.

3.2 Laser wire system

The laser wire system is an elaborate system in order to realize a stable laser wire. This system consists of a laser, laser transport system, various monitors, an optical cavity, a feedback system and a movable table. Fig.3.7 shows a setup of the laser wire system. In the following section, we will explain each component in detail.

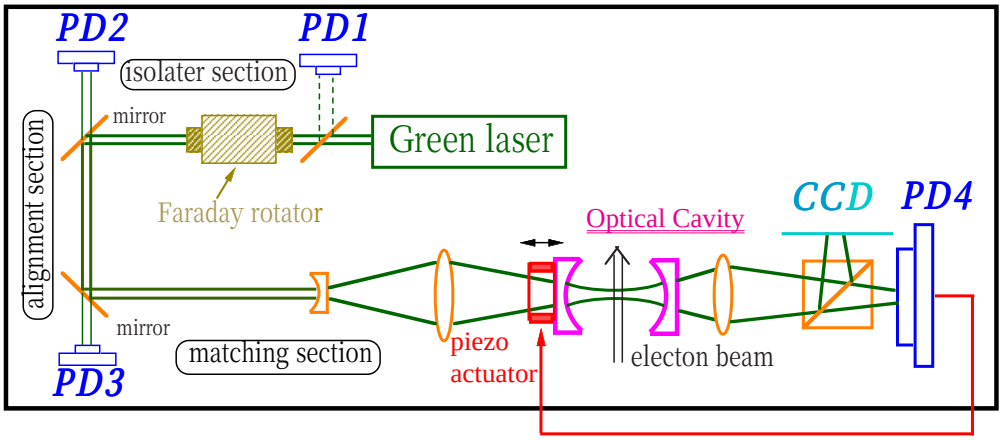

Figure 3.7: Setup of the laser wire system.

3.2.1 Laser

For our application, lasers are characterized by the parameters such as power, wave length, line width, stability, *etc* .

First, we will explain our requirements for these parameters. A green laser (λ=532nm) is chosen because of availability and easiness. If the wave length is shorter, control on the cavity length becomes severer to keep it on resonance. If the wave length is longer, tolerance on the cavity length becomes tighter to make a thin beam waist. A green laser is thus a good compromise. In addition, it is much safer to handle visible light than invisible one. Laser's line width is the next issue. The resonance width $\Delta\nu_{1/2}$ of our optical cavity is given by

$$\Delta\nu_{1/2} = \left(\frac{c}{2D}\right) \cdot \frac{1}{F} \quad , \tag{3.11}$$

where D is the cavity length and F is the finesse of the cavity [25]. Inserting D = 40mm and F = 313 into Eq.(3.11), we obtain $\Delta\nu_{1/2}$ = 12 MHz. (See Sec.3.2.4.) The third issue is laser's power. There is no clear criterion on the required laser power. Considering expected count rate ($\sim$ 1kHz) and cost, we selected 100mW as a good start.

Recently, technologies of high power and high coherent CW lasers have made much progress, especially in the field of diode-pumped solid state lasers. We have selected a diode-pumped solid state laser (Torus 532-100) whose wave length is 532nm [23]. This laser utilizes a YVO_4 crystal to generate 1064nm and a $KTiOPO_4$ (KTP) crystal [24] to generate its second-harmonic. The YVO_4 crystal is pumped by a diode laser. As shown in Table.3.1, this green laser satisfies requirements for both wattage (100mW) and narrow line width ($<$ 5MHz). In addition, its power is stable ($<$ 1% stability) and it gives TEM_{00} mode with a small M value ($M^2 < 1.1$). The former property is indispensable for a stable operation and clear signal identification while the latter is essential to excite the fundamental gauss mode in the cavity.

3.2.2 Laser light transport system

As shown in Fig.3.7, the transport system is composed of three sections. One is an isolator section, another is an alignment section, and the other is a matching section.

In the isolator section, a faraday rotator is installed between linear polarizers. The purpose of this section is to prevent reflected laser light from reentering the laser itself. Excessive amount of reflection would damage the laser. By this isolator, the reflection light is reduced to $\sim \frac{1}{10000}$. The alignment section consists of two precisely adjustable mirrors. When the laser light passes through the isolator section, the beam is shifted laterally. In order to compensate this shift, we use this alignment section. Finally we

Table 3.1: Specifications of the laser

parameter	value
Wavelength	532 nm
Output Power	100mW
Transverse mode	TEM_{00}
M^2	<1.1
Linewidth	< 5MHz
Beam Divergence	< 1.0mrad
Beam Diameter($1/e^2$)	< 1.0mm
Power Stability	< 1%
Pointing Stability	< 5μ rad
Noise(rms)	< 0.1%
Polarization ratio	> 100:1
Operating voltage	120/240 VAC or 100 VAC 50-60Hz

explain the matching section. This section consists of one convex and one concave lens. We mean by "matching" transformation of the laser light into TEM_{00} mode whose wave-front curvature coincides exactly with those of the cavity mirrors. If it does not match perfectly, not only TEM_{00} mode but also higher modes would be generated inside the cavity, leading to power loss [26]. Since the laser beam is TEM_{00} mode, procedure of the matching amounts to focus it at the cavity center with a specified curvature. There are several practical conditions to be satisfied. First of all, we want to fix distance from the laser to the optical cavity. We also need room for the isolator section and alignment section. Finally, we want to place two lenses outside a vacuum chamber, in which the cavity is installed. We optimized the focusing length and position of the lenses using the ABCD law [16], [27]. Fig.3.8 shows the optics of the transport system we employed.

It is found that aberration at the lenses in the matching section would cause partial mismatching of the injected mode with the cavity. This would lead to power loss inside the cavity. In order to remove aberration, we must use non-spherical lenses or make a spot size smaller at the lenses. The final optics shown in Fig.3.8 is a result of a compromise; we want to use available lenses and want to place them outside the vacuum chamber. By this optics, we can realize 70% efficiency in injecting laser intensity to the optical cavity. We refer this efficiency as "matching efficiency". Transmission of the laser power is 80% in this transport system.

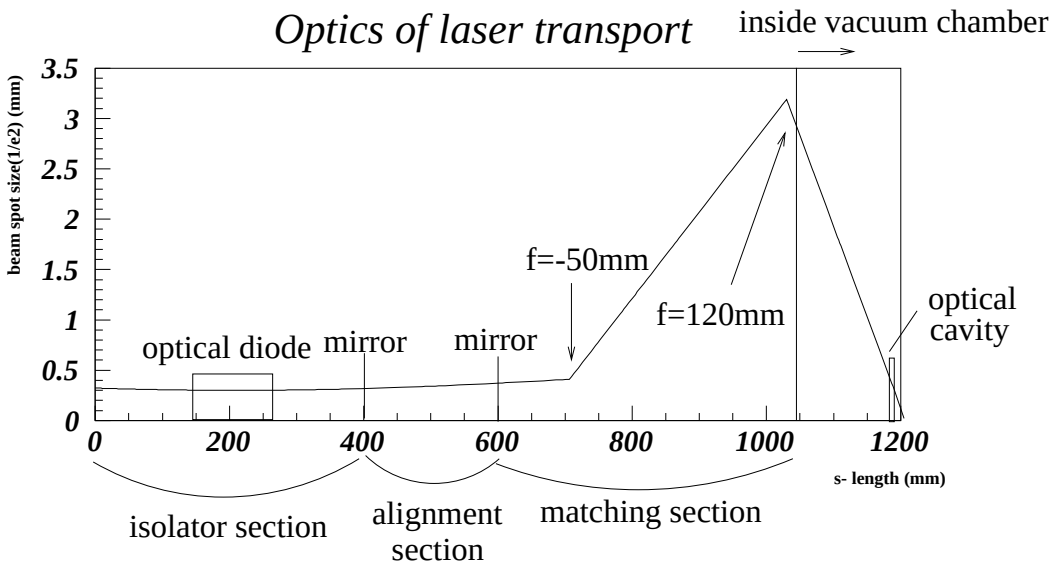

Figure 3.8: Optics of the laser transport system. The horizontal axis shows the position from the exit of the laser to the front of the optical cavity. The vertical axis shows the beam spot size $w(s)$. To realize thin beam waist inside the cavity, the beam spot size is once enlarged by concave lens and is focused by the convex lens. To decrease the effect of the aberration at the convex lens, the convex lens is placed as close as the vacuum chamber as possible.

3.2.3 Monitors

Laser light monitor As shown in Fig.3.7, there are 4 Si PIN photodiodes in the system. They are used to monitor original laser intensity (PD3), reflection intensity from the optical cavity (PD2), reflection intensity from the isolator (PD1), and transmission intensity through the optical cavity (PD4). Each photodiode is enclosed in an Aluminum box to reject stray room light and/or electrical noises. The signals are read by a current amplifier, as shown in Fig.3.9.

Profile monitor In order to observe a beam profile inside the cavity, we set a CCD camera at the rear exit of the optical cavity. This monitor is useful when the cavity is being tuned or during data taking to confirm the cavity mode. When the cavity is misaligned and higher modes other than TEM_{00} are excited, we can tell from its beam profile. Fig.3.10 and Fig.3.11 show examples of TEM_{00} and TEM_{10} mode observed by this monitor, respectively.

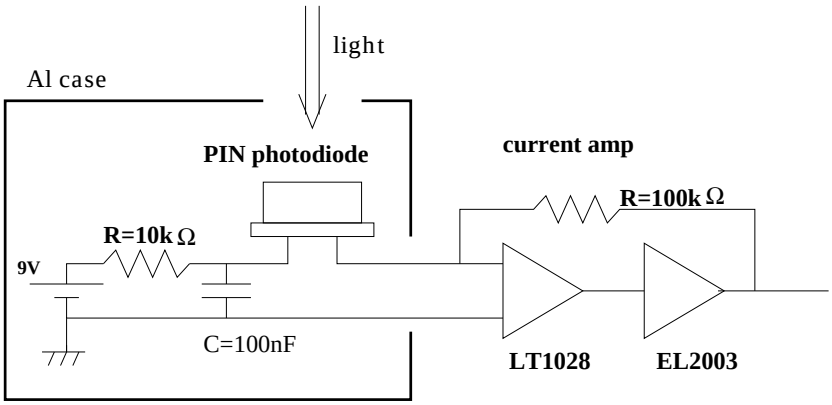

Figure 3.9: Diagram of a PIN photodiode laser intensity monitor.

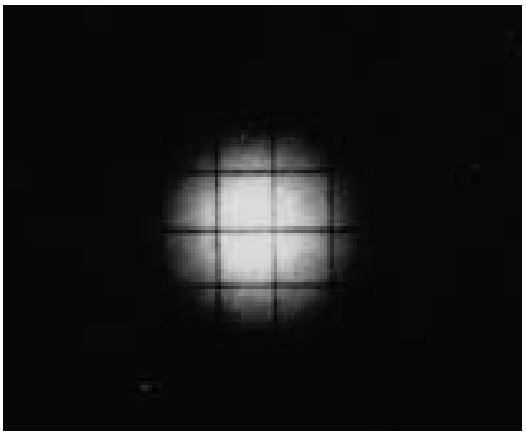

Figure 3.10: Picture of TEM_{00} mode

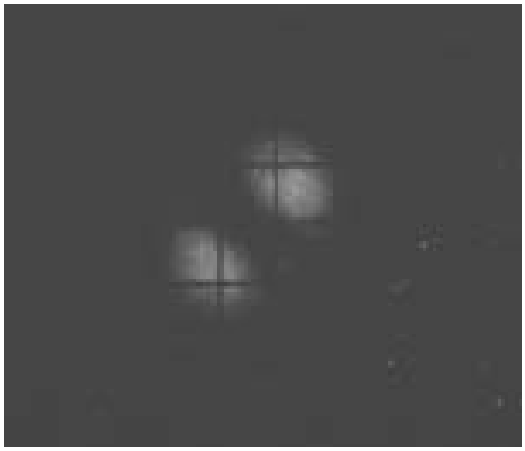

Figure 3.11: Picture of TEM_{10} mode

3.2.4 Optical Cavity

The heart of a laser wire system is an optical cavity. The optical cavity consists of two high reflectivity mirrors facing each other. These mirrors are housed in a harmetical structure made of SUS. In this section, we describe mechanical structure of the optical cavity and its optical properties.

Structure of the optical cavity

Fig.3.12 and Fig.3.13 show mechanical structure of the optical cavity. There are two mirrors sandwiching the beam pipe. Both mirrors are set on a mirror holder and these mirror holders are in turn connected by a cylinder.

In order to control the cavity length D, we utilize a hollow cylindrical

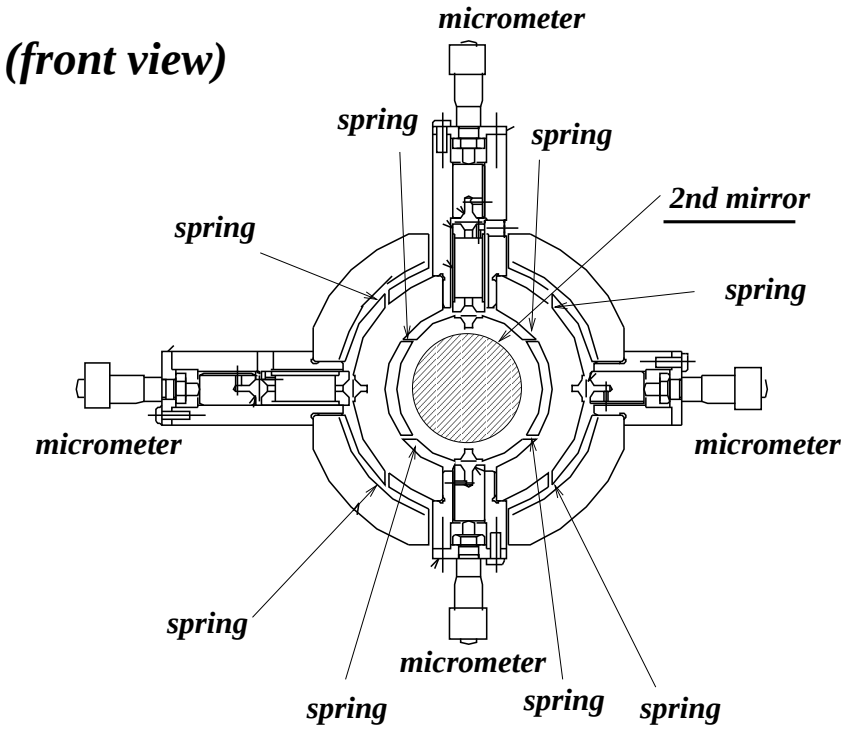

Figure 3.12: Structure of the optical cavity (front view). The position of the 2nd mirror is adjusted by the micrometers through plate springs. The micrometer is also used to fix the 2nd mirror.

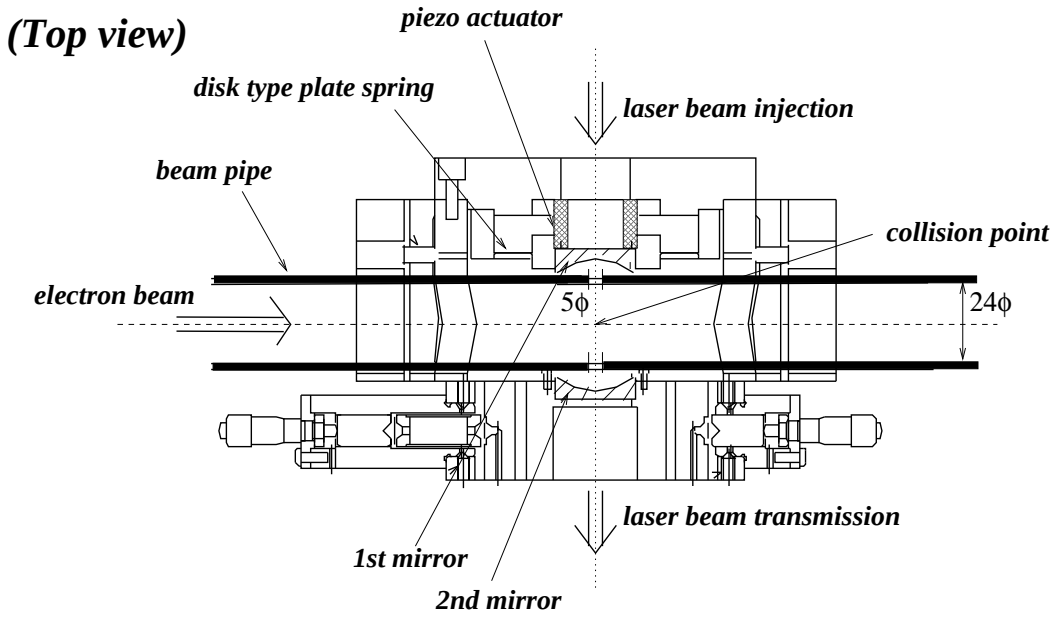

Figure 3.13: Structure of the optical cavity (top view). Meshed area shows the piezo actuator and slashed areas show mirrors. The piezo actuator supports the 1st mirror through a disk type plate spring. Beam pipe is inserted inside the optical cavity, and has a 5ϕ mm hole to make a laser beam go through the beam pipe and interact with electrons.

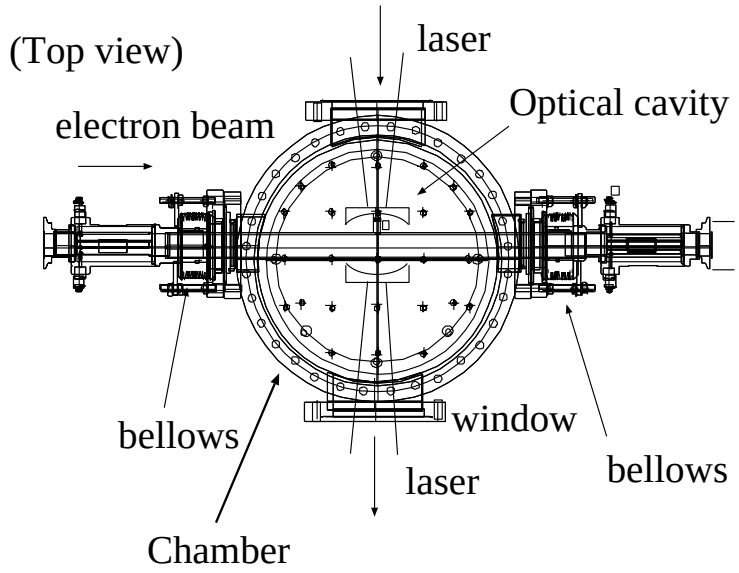

Figure 3.14: The laser wire vacuum chamber. The optical cavity is installed inside the vacuum chamber.

piezo actuator. This piezo actuator supports the 1st mirror through a disk type plate spring. To obtain high resistance to disturbance, we add a 10kg load to the piezo actuator using a plate spring. The mechanical resonance frequency of the first mirror is found to be about 800Hz. The piezo actuator controls the cavity length; its dynamic range is about 3μm with sensitivity of 3nm/V.

The transverse position of the second mirror is adjustable by micrometers through a plate spring as shown in Fig.3.12. By adjusting these micrometers, the cavity's optical axis is aligned to that of the laser input beam.

The beam pipe diameter is chosen to be 24mm; this is exactly the same as the other part of the ring. It should be noted that sudden change in the beam pipe size should be avoided because circulating electrons would "see" the change and generate wake fields.

The laser beam is injected and transmitted through BK7 windows on the chamber. All of the structure of the optical cavity, except for the beam pipe, are set on a movable table. The chamber is mechanically connected with the beam pipe via bellows to reduce the mechanical vibration coming from water flow for magnets.

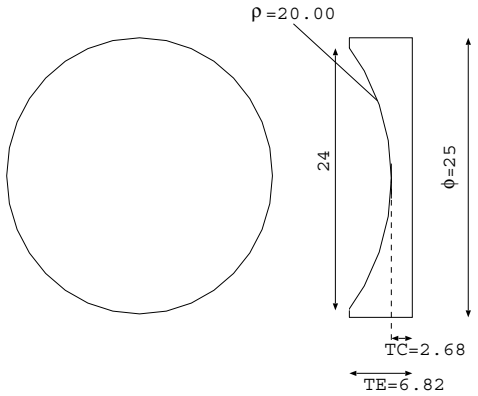

parameter	value	accuracy
ρ(radius)	20.00mm	0.5μm
TC(height of center)	2.68mm	0.01mm
TE(total height)	6.82mm	0.01mm
ϕ (diameter)	25.0mm	0.1mm
roughness (rms)		0.5nm

Figure 3.15: Parameters of the mirrors. Left figure shows the geometry of the mirror.

Geometrical dimensions of mirrors

Fig.3.15 shows the dimensions of our mirrors. Among their dimensions, the curvature ρ is most important, and is determined by the following consideration. In order to realize a very small waist, the optical cavity must be nearly concentric ($D \sim 2\rho$). Under this circumstance, the smaller is the curvature ρ, the looser is the tolerance on $(2\rho - D)$. The 24mm diameter beam pipe must, however, set inside the optical cavity. Thus, D must be bigger than 24mm. To be conservative, we select the mirrors with ρ=20mm.

Optical properties of mirrors and the power enhancement factor

In this subsection, we will explain how to determine optical parameters of mirrors, and a power enhancement factor of the cavity. We have two sets of mirrors. One set has 99% reflectivity (type α), the other has 99.9% reflectivity (type β). These values are nominal values, taken from manufacture's catalogue.

We first show the method to measure optical parameters of mirrors such as T, R and A, described in Sec.2.2.2. The setup shown in Fig.3.7 is used for this purpose. First of all, the cavity length was changed by the piezo actuator to observe several FSRs. The actuator was driven by a HV amplifier, which was in turn cycled by a triangle wave generator. Then we observed outputs of the photodiodes PD3 and PD4. Their wave forms are represented by Airy function, as discussed in Sec.2.2.2. Fig.3.16 shows the oscilloscope picture of PD4, the transmitted intensity from the cavity. When the resonance condition is satisfied, the output shows a sharp spike. The distance between the two peak is $\lambda/2$ (FSR). Fig.3.17 shows the expanded view of PD3 and PD4 near the resonance. In the figure, the amplitude (a) is the maximum of

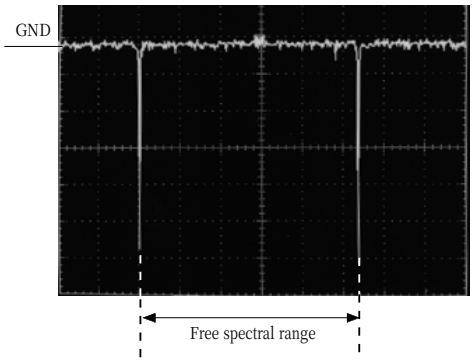

Figure 3.16: Picture of the Airy function. We can see the periodic condition, and measure the FSR.

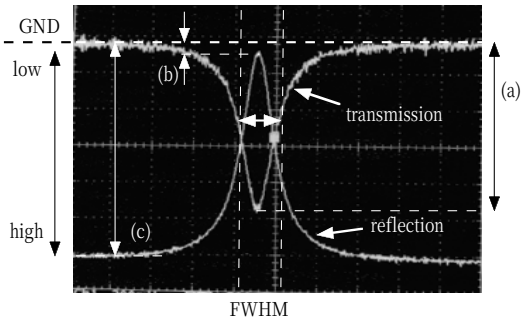

Figure 3.17: Picture of the transmission (a), reflection (b) the FWHM of the Airy function. By using the measured parameter (a), (b), (c), FWHM and injected laser, we estimate the parameter of the mirrors $(R_\alpha, T_\alpha, R_\beta, T_\beta)$

the transmitted power, (b) is the minimum of the reflected power, and (c) is the power reflected from the cavity when it is off resonance. We also measured the laser intensity before injecting the optical cavity by PD4. This intensity is denoted by (d). In addition, we determined FWHM of the resonance (2δD). From these measurements, we could determine three cavity parameters: $T_{res}^{(0)}$, $R_{res}^{(0)}$ and F. Specifically, the transmissivity ($T_{res}^{(0)}$) was obtained by (a)/(d), the reflectivity ($R_{res}^{(0)}$) by (b)/(c), and the finesse F by FWHM/FSR. We measured these quantities for all combinations of (α, α), (α, β), (β, α) and (β, β), and the results are summarized in Table.3.2.

Now we want to estimate the parameters $(R_i, T_i, A_i \ ; \ i = \alpha, \beta)$ of the mirrors from Eq.(2.24), Eq.(2.25) and Eq.(2.23). Actually, we searched the region of the parameter $(R_i, T_i, A_i \ ; \ i = \alpha, \beta)$ which satisfied all the results in Table.3.2. The resultant parameter values are listed in Table.3.3. It is found that the absorption is not negligible and the reflectivity is less than a catalogue value.

Finally, we calculated the enhancement factor from Eq.(2.26). Table.3.4 shows the result for each combination of the mirrors. To obtain the highest enhancement, we employed the combination of type α for 1st mirror and type β for 2nd mirror. We expect an enhancement factor of 220 for this combination.

Table 3.2: Results of the cavity parameter measurements for 4 mirror combinations.

Combination of mirror (1st,2nd)	Transmissivity	Reflectivity	Finesse
(α, α)	$60\% \pm 6\%$	$< 10\%$	310 ± 30
(β, β)	$4\% \pm 4\%$	$69\% \pm 7\%$	
(α, β)	$7.5\% \pm 2.5\%$	$< 10\%$	425 ± 75
(β, α)	$8\% \pm 2\%$	$80\% \pm 8\%$	425 ± 75

Table 3.3: The measured mirror parameters.

The type of mirror	Reflectivity R_i	Transmissivity T_i	Absorption A_i
α	0.9892 ± 0.0003	0.0083 ± 0.0003	0.0025 ± 0.0004
β	0.9935 ± 0.0004	0.00087 ± 0.00004	0.0056 ± 0.0004

Table 3.4: The summary of the enhancement factor measurements.

Combination (1st,2nd)	Enhancement factor
(α, α)	141 ± 6
(β, β)	41 ± 5
(α, β)	220 ± 20
(β, α)	23 ± 1

Beam waist measurement

Another important parameter in the cavity is its beam waist w_0. Its measurement methods and results are presented in Sec.4.2 for convenience. Here, we simply quote the final result: $w_0 = 14.5 \pm 0.45(\mu m)$

3.2.5 Feedback system

In order to keep the cavity on resonance, its length must be controlled with accuracy of less than 1nm. It is expected that external disturbances, such as temperature variation and/or acoustic noises, would easily influence the cavity length. Thus, an active feedback is necessary. It maximizes the transmission signal by changing the cavity length with a piezo actuator.

Fig.3.18 shows a schematic diagram of the actual feedback system. It generates a symmetric square wave of 1kHz frequency (See "clock" in Fig.3.18). The piezo actuator is modulated by a triangular wave with an amplitude much less than the value corresponding to the width of the peak. This is generated by integrating the basic square wave. The error signal is formed with the output signal of the transmitted light multiplied by the basic square wave, and then integrated over a certain period of time. In short, the error signal is a deviation of the transmitted signal with $\pm$ sign depending upon the phase of the modulation wave. For example, when the cavity is sitting at the top of Airy function, the contribution from positive and negative modulation parts cancel out since its deviation is same in sign and magnitude. On the other hand, if the cavity is sitting on a steep slope, the error signal would have non-zero value (See A or C in Fig.3.18).

In order to demonstrate the stability of the feedback system, we monitored the transmission light for a long time (See Fig3.19). The horizontal axis shows the elapsed time and the vertical axis shows the transmission intensity (See the top line). From the measurement, although it is not shown in Fig.3.19, we found this system remained stably on resonance for more than one day.

3.2.6 Movable table

The laser wire system is mounted on a movable table. This table is supported at three point, where stepping motors are independently set. The table is moved vertically with 1 μm accuracy. Its vertical position is monitored by a position monitor [28]. This position monitor is set on a long Al channel above the laser wire chamber as shown in Fig.3.20. This Al channel is supported by the nearest two quadrupole magnets.

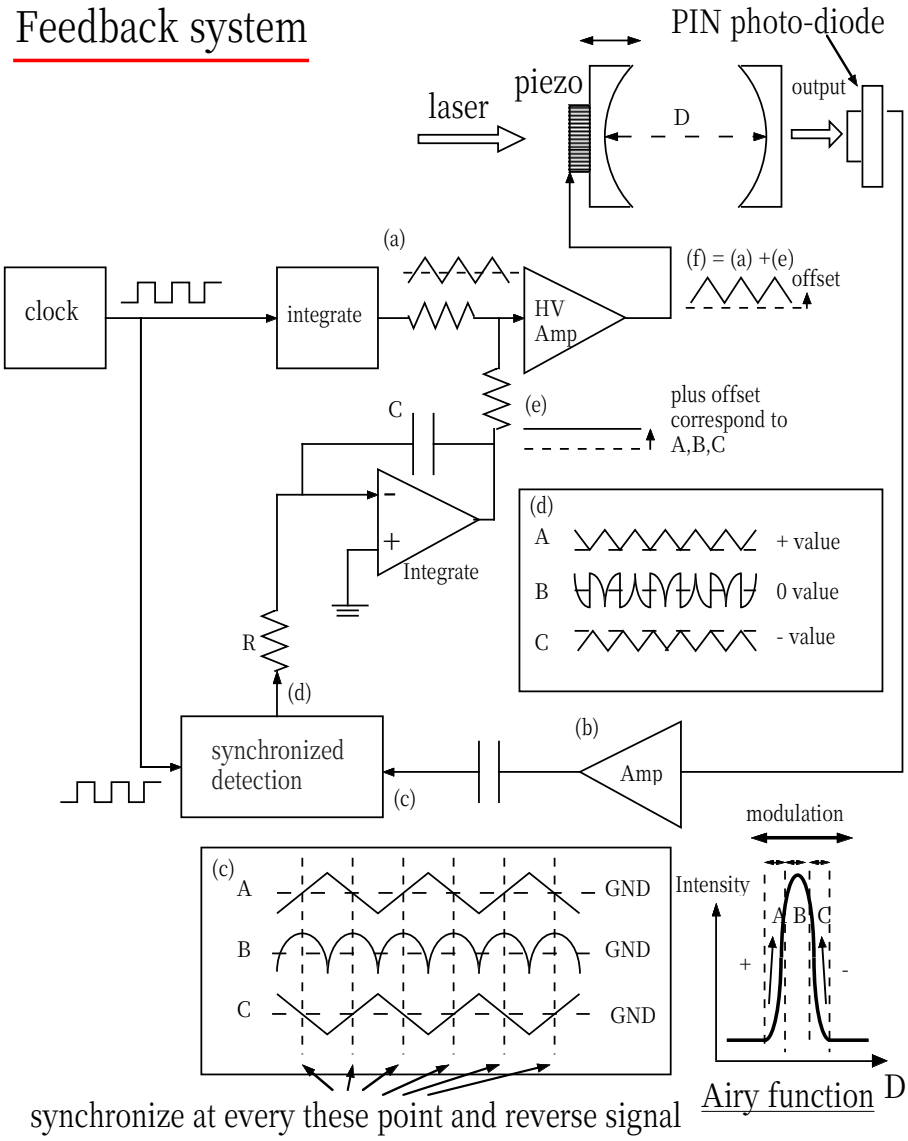

Figure 3.18: Schematic diagram of the feedback system. See the text for detail.

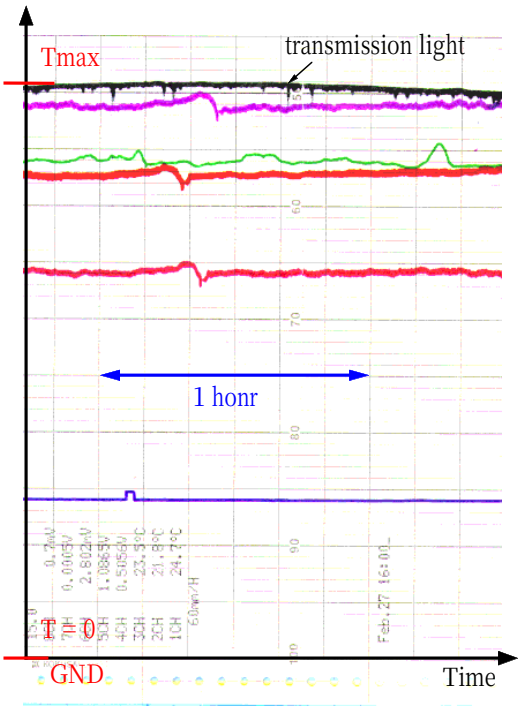

Figure 3.19: Long term stability of the transmitted light. The horizontal axis shows the elapsed time, while the vertical axis shows the intensity of the transmitted light. T_{max} corresponds to the peak of the Airy function.

The position stability was measured for one day and the results are shown in Fig.3.21. From this measurement, the vertical position was found to be stable within $\pm 1\mu$m.

3.3 Photon detector system

The scattered photons were detected by a photon detector system placed 12.8m downstream of the laser wire. Fig.3.22 shows the schematic diagram of the photon detector. We used a CsI(pure) scintillator and a 2" photomultiplier (PMT) to read its light. We selected CsI(pure) considering its fast response, a good light yield and compactness. Its size was 50mm $\times$ 50mm in cross section, and 100mm in length. To avoid the saturation due to its slow component, we inserted UV filter between the scintillator and PMT. In addition, we put a capacitor in a readout circuit to remove a DC component (See Fig.3.22). A 100mm thick lead collimator was installed in front of the CsI crystal; this was to reject unwanted backgrounds and to enhance signal-to-noise ratio.

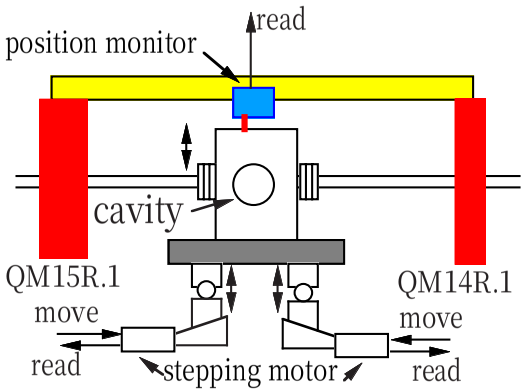

Figure 3.20: Structure of the movable table. The position monitor is also shown.

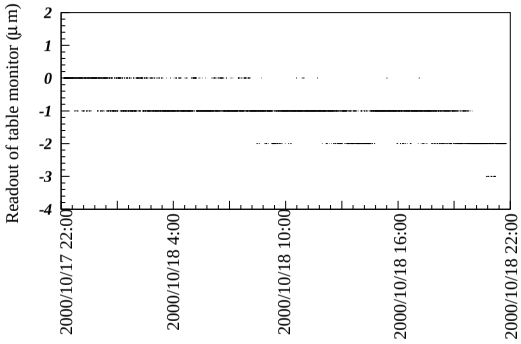

Figure 3.21: Plot showing the long term stability of the movable table.

Prior to the experiment, energy scale was calibrated with standard gamma sources of ^{22}Na (0.511MeV, 1.275MeV) and ^{137}Cs (0.662MeV). The linearity of detector responce was confirmed by these sources. The results are shown in Fig.3.23, in which the horizontal (vertical) axis is the gamma energy (ADC counts). We also used an LED light pulser. It provided a very convenient way to check PMT gain during the emittance measurement. It was also used to "connect" two energy regions: the source energy region($\sim$ 1MeV) and the Compton photon energy region (10-30 MeV). In order to see clearly the source's gamma rays, we had to raise PMT HV slightly. Thus the HV settings during the emittance measurement and during the source calibration differed slightly. By observing the LED pulse in both settings, we could scale the ADC unambiguously. Fig.3.24 shows the LED signal, which corresponds to 11.5 MeV, when observed with the source gamma rays.

Before the measurement, the background study was performed using the same setup to measure the beam size. It was found that the spatial distribution of the background was broader than that of the Compton scattered gamma. The detail of the background study is presented in Appendix B.

3.4 Alignment

Magnet alignment is crucially important to realize low vertical emittance. Fine alignment was performed by a 3-D mobile tracking system, Leica SMART 310 [29]. This monitor system could measure distance, polar angle and azimuthal angle to a target retro-reflector (so called as Cat's eye) by laser interferometry. The distance resolution is 1.3 μm and angular resolution is

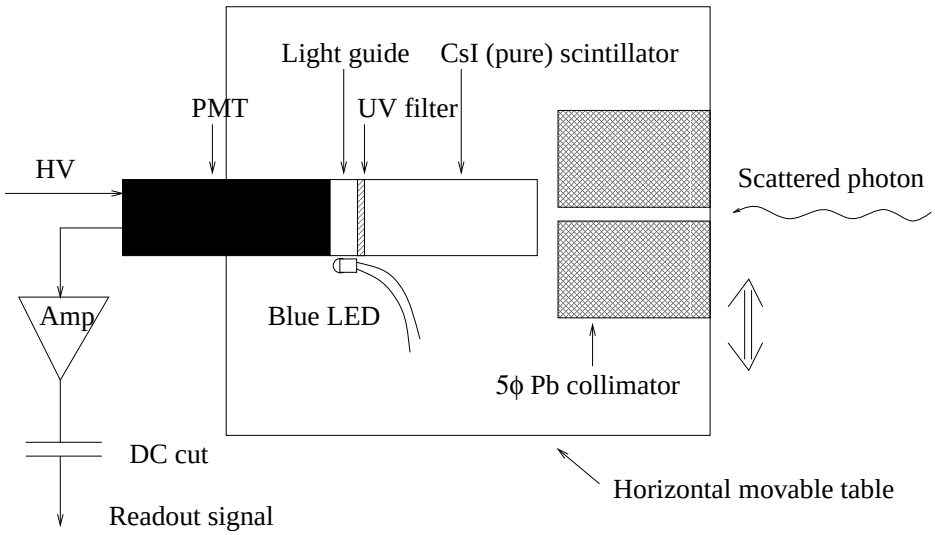

Figure 3.22: The schematic diagram of the photon detector system. Scattered photon is collimated with 5mm diameter lead, and detected with CsI(pure).

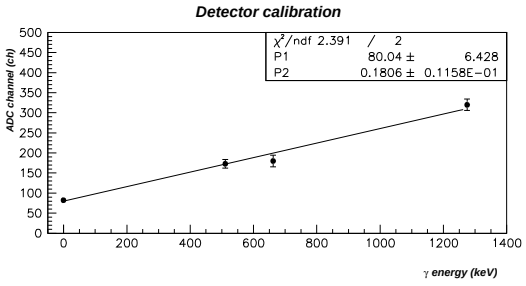

Figure 3.23: Energy calibration of the photon detector by using ^{22}Na and ^{137}Cs.

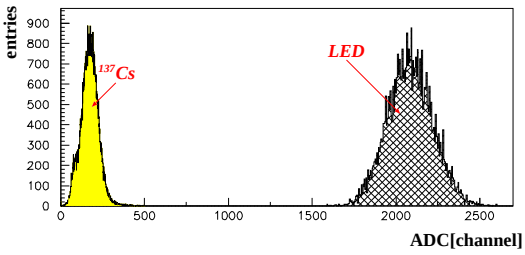

Figure 3.24: ADC spectrum showing both ^{137}Cs and LED peaks.

3.4 μrad according to the catalogue values. The Cats'eye was set on a reference level of each magnet. Results of position measurements after alignment are shown in Fig.3.25 and Fig.3.26. Fig.3.25 shows the horizontal(x) and vertical(y) deviations from ideal positions. Fig.3.26 shows the longitudinal deviations. The r.m.s position errors are found to be 39 μm and 28 μm for x and y directions, respectively. These values are within the tolerance of the design values listed in Table.A.1.

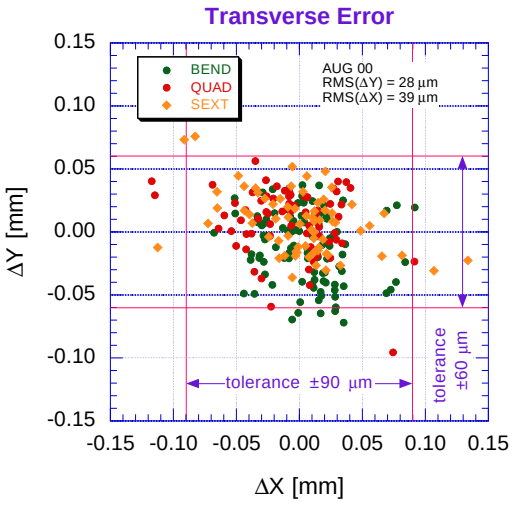

Figure 3.25: Transverse positioning error. Each dot represents horizontal (Δx) and vertical (Δy) displacements for each magnet.

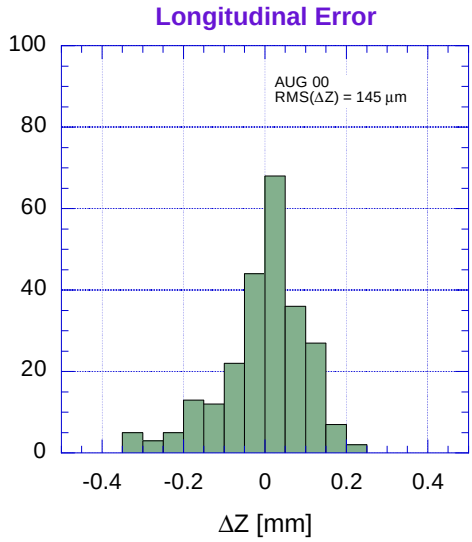

Figure 3.26: Distribution of longitudinal positioning errors.

The laser wire system also needs precise alignment. The collimator should precisely directed to the laser wire to detect scattered photons efficiently. Fig.3.27 shows the alignment system of the collimator. The beam line level was defined by center of the quadrupole magnets. We transfered the vertical level to the two target marks using a telescope. Horizontal reference was also transfered to two target marks by a theodolite. Finally the center of the collimator was aligned to the beam line by the telescope referring to the two target marks. The alignment error was estimated to be less than 0.1mm horizontally and 0.4mm vertically.

After the alignment, the position of the laser wire was confirmed by directly observing it through the collimator and beam pipe. Fig.3.28 shows the picture of the laser wire. The laser wire is estimated to be set within $\pm 50 \mu$m vertically and within 4mrad vertical tilting.

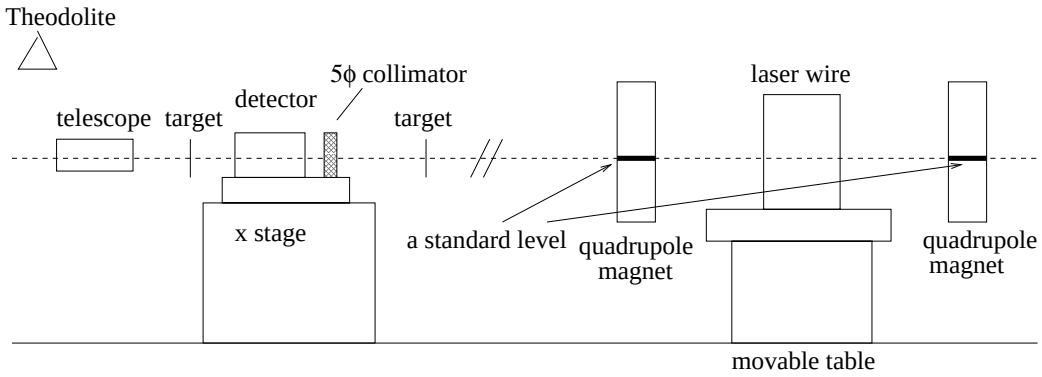

Figure 3.27: Side view of the alignment system. Standard level was set to the center of quadrupole magnets and transfered to two target marks by using theodolite and telescope. The center of collimator was aligned to the beam line by a telescope referring the two target.

3.5 Data taking logic

3.5.1 Laser Intensity Modulation

As is described in Appendix B and Sec.3.1.1, there existed rather severe backgrounds in this experiment, and they had to be subtracted out statistically to single out the genuine Compton signals. Thus, it was highly desirable to measure background count rate simultaneously with actual data taking. This required switching on and off the laser wire during the measurement. The laser-on data provided signal plus background counts while laser-off data gave background counts. In reality, the laser on/off system was realized by enlarging the modulation amplitude of the piezo actuator.

Fig.3.29 shows the transmitted laser intensity from the cavity, together with other relevant signals. The bottom signal is the 1kHz basic clock (square wave) signal, and the middle one is the triangle modulation signal to the piezo actuator. Its modulation amplitude was enlarged so that the cavity length covered one entire resonance peak. Thus the transmitted laser intensity swinged from zero to its maximum value.

Each event had to be taken together with laser intensity information. Actually, we read the transmitted laser intensity in the following way. The laser intensity, read by the photodiode, was classified into 5 laser intensity level by a multi-level comparator(MLC). Fig.3.30 shows the each comparator level with respect to the transmitted laser intensity. When the laser intensity is lower than the threshold level, each comparator level returns the NIM logic 'high'. Five scalers were prepared. Each scaler read counts only when the

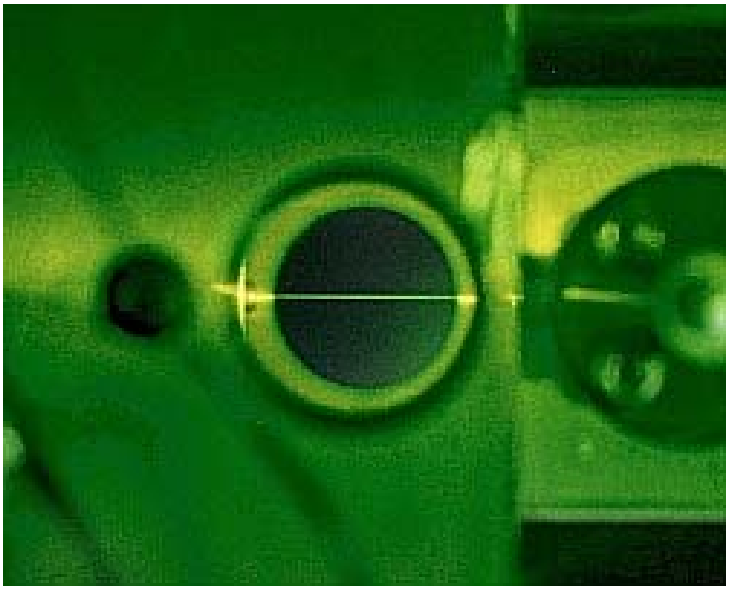

Figure 3.28: Side view of the laser wire inside the optical cavity.

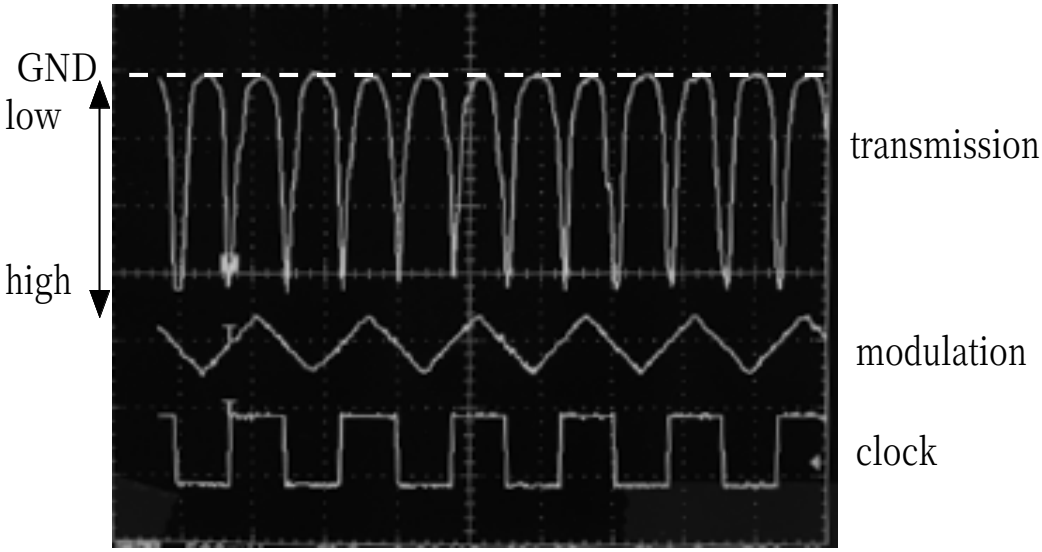

Figure 3.29: Laser modulation. (Top) The transmitted laser intensity. (Mid) The modulation signal to the piezo actuator. (Bottom) The basic clock.

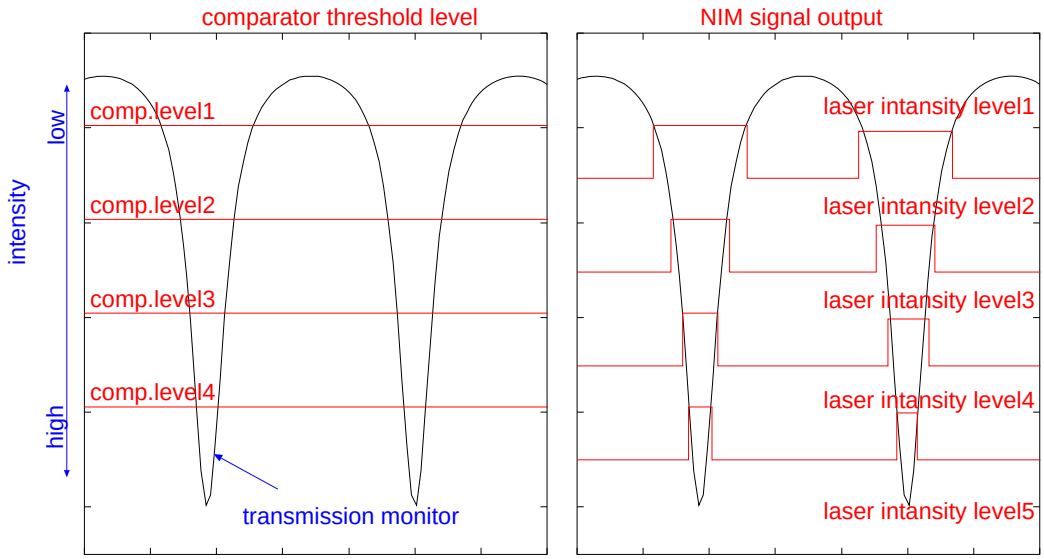

Figure 3.30: Transmitted laser intensity and comparator levels. (Left) the setting of each comparator level 1-4. (Right) the NIM output signal corresponding to the each comparator level.

laser intensity exceeded the corresponding comparator level. One scaler, however, always read counts irrespective of the laser intensity. After some arithmetic, we could classify scaler counts according to the 5 laser intensity levels (LL1 - LL5).

The stability of the incident as well as the transmitted laser intensity from the cavity was monitored and recorded by ADC. Fig.3.31(top) shows an example of the incident intensity; it remained stable within 0.5% of the average value. Fig.3.31(bottom) shows the transmitted intensity; the 5 different lines corresponds to 5 different laser intensity level (LL1 - LL5). This plot shows that each of the transmitted intensity was stable within a few %.

3.5.2 Data Acquisition System

Fig.3.32 shows the logic of the data taking system. The output from the photomultiplier was first amplified and divided into 4 signal. They were then discriminated with different threshold levels, corresponding to 5, 15, 25 and 35 MeV. Then outputs from the discriminators (MLD) were read by scalers. The linearity of the threshold energy was calibrated by using ADC within 4% resolution. All data from ADC and scalers were taken by a local computer via a CAMAC system. Trigger of the data taking was made by the

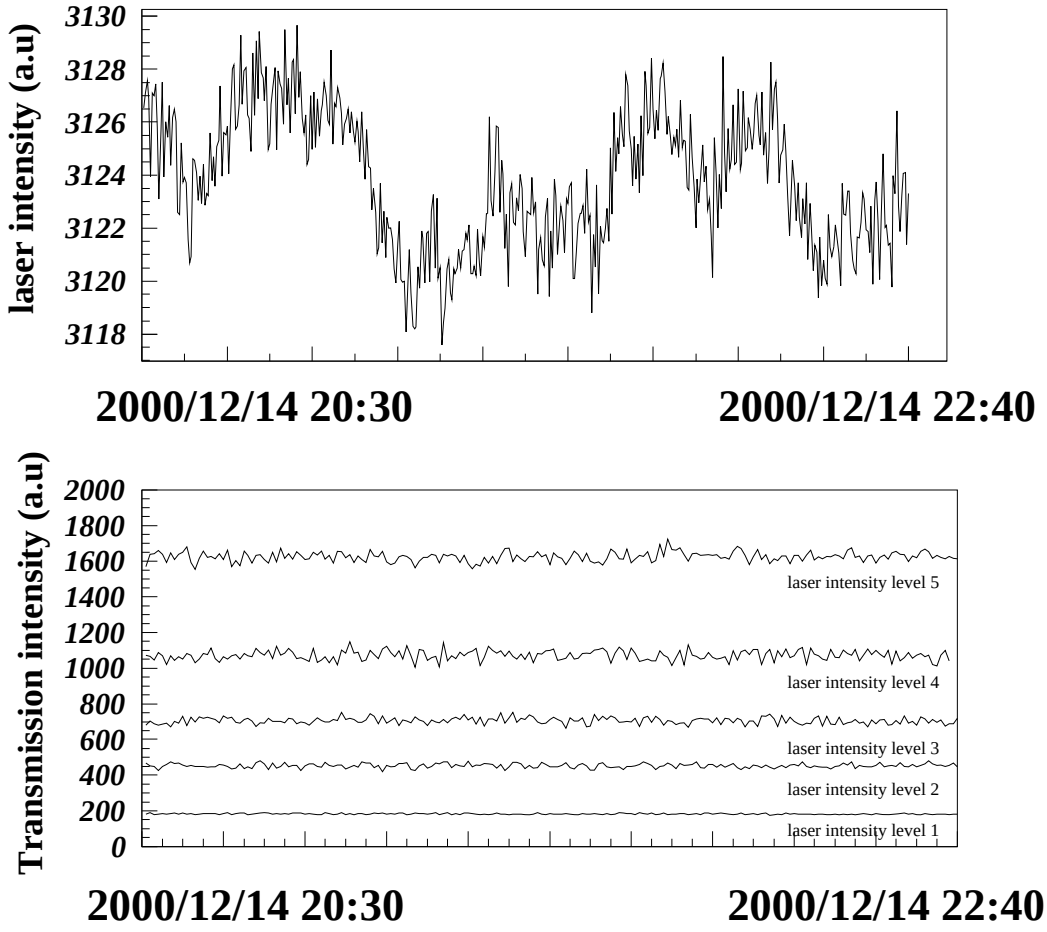

Figure 3.31: Stability of laser wire power. Top figure plots the laser intensity monitored at PD3 and bottom figure plots the transmission light intensity on each laser intensity level.

10Hz clock generator via Event LAM Register (ELR) [1]. Actual data taking was done every one second. All data of the scalers were read into the local computer and cleared. We also read a revolution clock of a damping ring (2.1645MHz) by each scaler.

Information of the position monitor, the electron current and the vacuum pressure was recorded, too. The position monitor was read from another local computer(atflw-2). The electron current and the vacuum pressure were read into another computer(atfaxp). Data on these computers were read into main computer (atflw-1) every second via a network, as shown in Fig.3.33.

[1] This module was developed to see the condition of the LAM. When an input signal come, LAM is set and busy output is issued from the front panel.

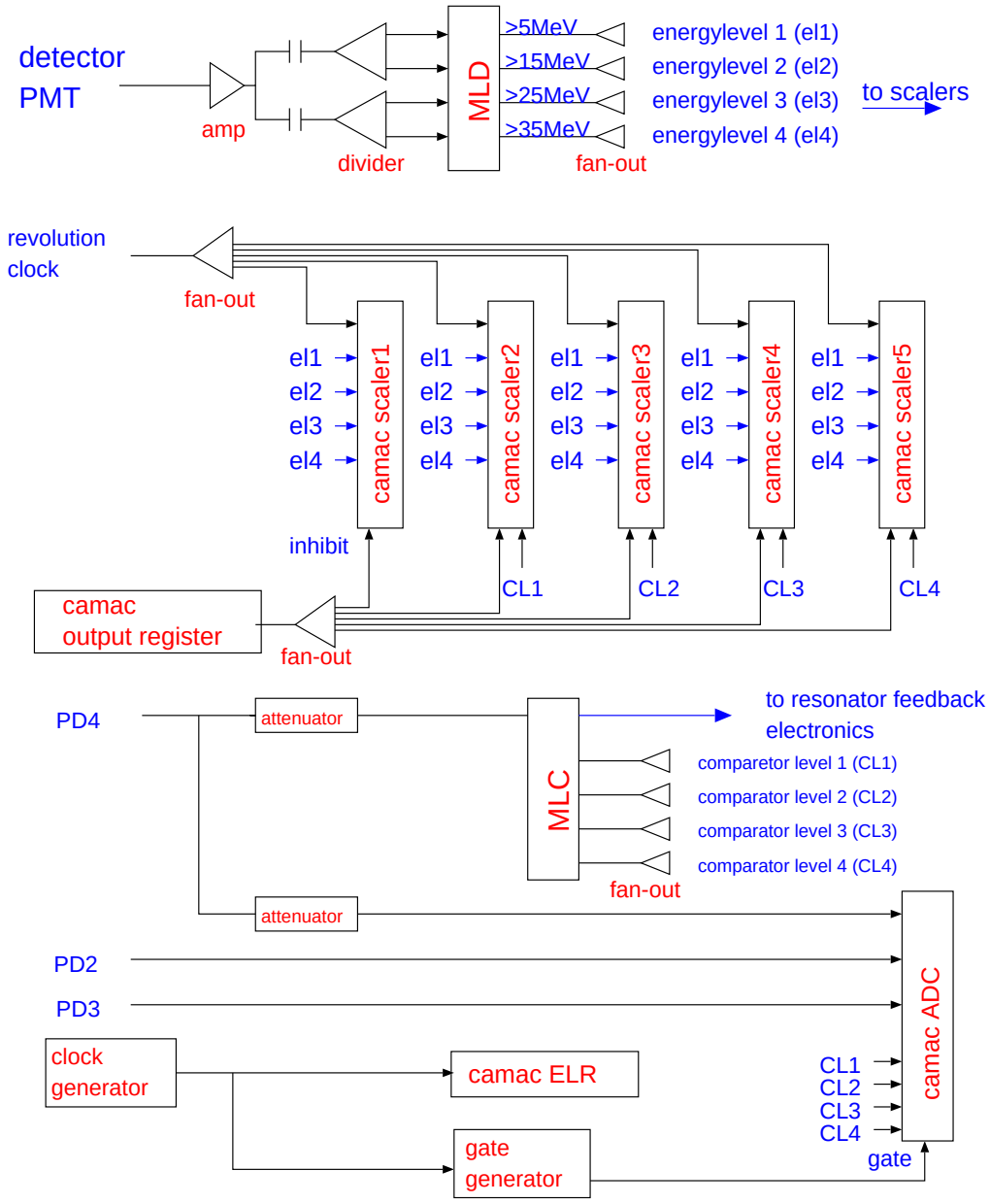

Figure 3.32: Schematic diagram of laser wire data taking logic

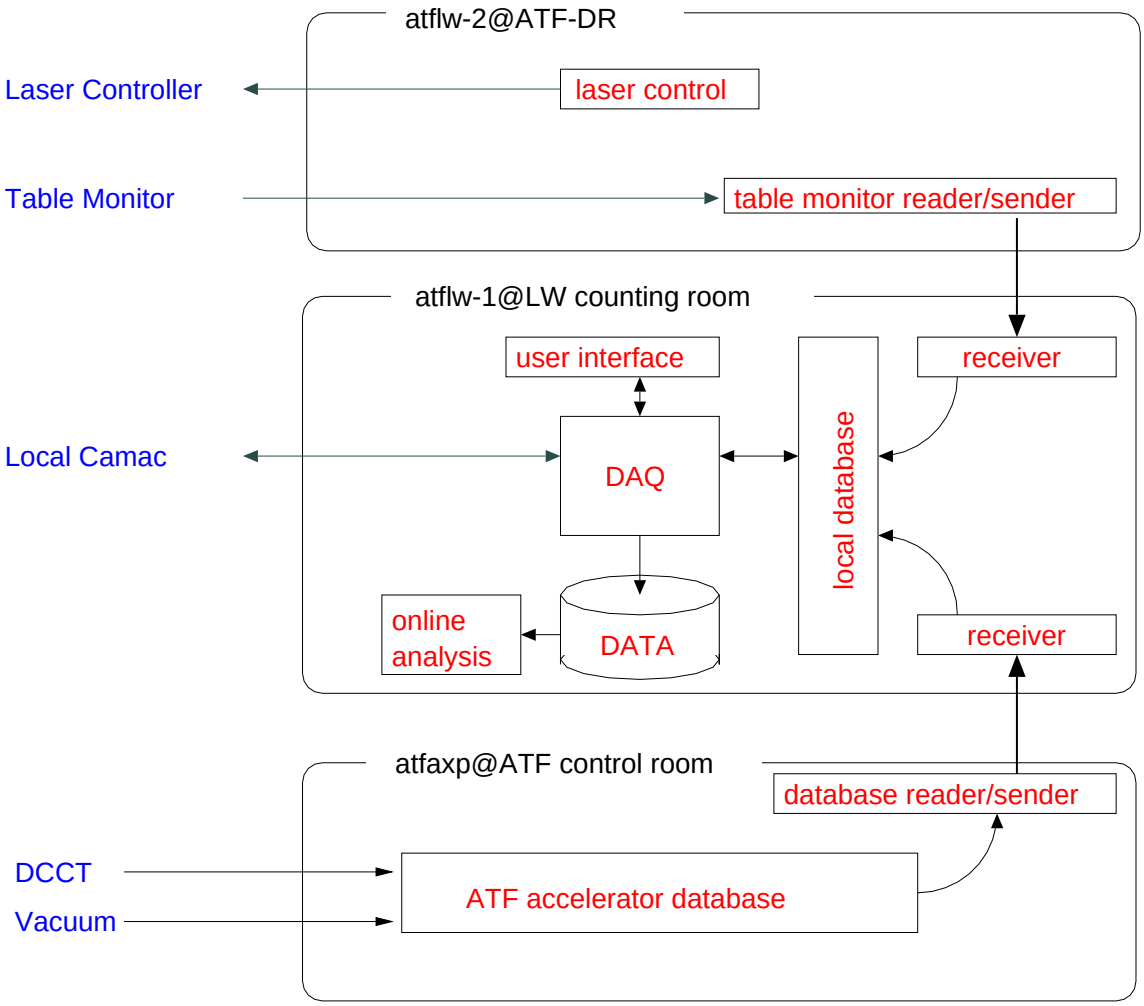

Figure 3.33: DAQ system

Chapter 4

Data Analysis and Results

We measured the vertical emittance three times with different damping ring conditions. Characteristics of the conditions and their particular purposes are summarized as follows.

1. We tuned the ring following the procedure described in Sec.3.1.4. In particular, the skew correction was carefully performed to make the vertical emittance as small as possible. The measurement was done on Dec.5th, 2000.

2. We skipped the skew correction on purpose, expecting large emittance due to the x-y betatron coupling. The measurement, done on Dec.7th, 2000, was to confirm this coupling effect and the response of the laser wire measurement to it.

3. The purpose of the 3rd measurement was to confirm the 1st one. However, as it will be described, the condition of the ring, especially its β function and tune ν, were turned out to be somewhat different from those in 1. The measurement was carried out on Dec.14th, 2000.

In this chapter, we describe the data analysis of these measurements and results in detail. There are three essential quantities to determine in measuring vertical emittance: electron's vertical beam size (σ_{obs}) as measured by the Compton process, laser wire beam waist(w_0), and β function. First we explain the measurements of the vertical beam size. Then, we describe the methods and results of laser wire beam waist measurement. Next we illustrate the β-function measurement in detail. Finally, we put these quantities together to calculate the vertical emittances. In the last subsection, we discuss about our final results, and comment on effect of intra-beam scattering. Future prospects are also included in this section.

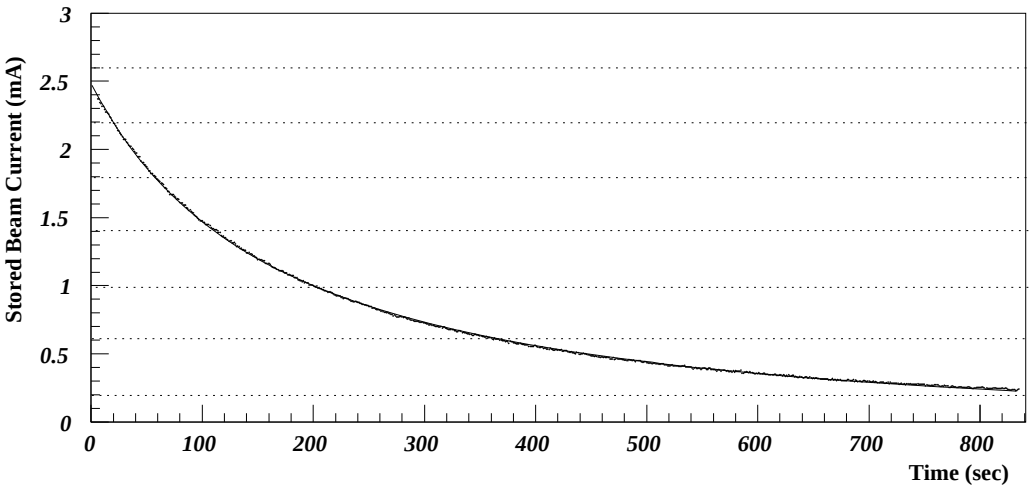

Figure 4.1: Electron beam current vs time for one fill. Dotted line show the current intervals used to classify scaler counts.

4.1 Measurements of the vertical beam size

4.1.1 Data taking procedure

In this section, we describe data taking procedure of vertical beam size measurements. First we searched for Compton signals by scanning the movable table. Having found the Compton signals, we then scanned horizontally the detector and collimator to maximize the signal rate. This was to align them to the line defined by the laser wire and electron's beam direction. As to the vertical alignment, we relied on the survey, described in Sec.3.4. Actual data was taken following the steps listed below:

1. Set laser wire position by moving the table.
2. Store an electron beam in the damping ring.
3. Take data every 1 second for 10-15 minutes.
4. Repeat the procedures 1.-3.

The procedures from 1. to 3. was defined as 1 run. These runs were continued until the laser wire scanned an entire electron beam profile.

Fig.4.1 shows a typical example of the electron beam current (I_e) in the damping ring in one run. The horizontal dotted lines in the figure will be explained later. In order to illustrate background-to-signal ratio in our experiment, examples of raw counts, corresponding to an energy range of 15-20

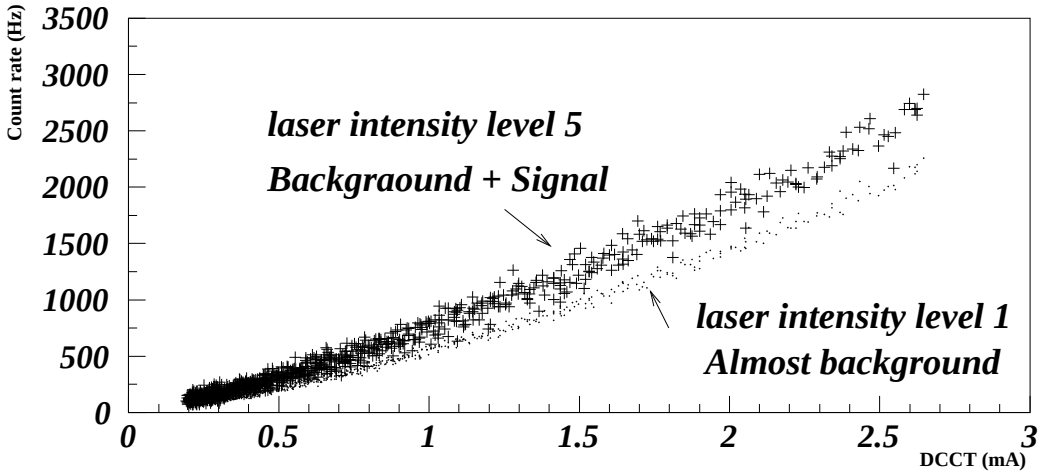

Figure 4.2: Raw count rate vs electron beam current. The cross points show laser-on data (laser intensity level 5), while the dotted points show laser-off data (laser intensity level 1).

MeV and taken when the laser wire was right on the electron beam, are plotted in Fig.4.2 as a function of the electron beam current. The cross points represent the laser-on (laser intensity level 5) data while the dotted points show the laser-off (level 1) data. Difference is clear but background is non-negligible.

4.1.2 Data reduction

As we explained in Sec.3.5, the number of scattered photons was counted by scalers. Separate scaler counts were collected according to the laser intensity level, scattered photon energy, current of electron beam (time), and position of movable table. The scaler count categories are summarized in Table.4.1. We obtained the vertical beam size (σ_{obs}) with the following procedure.

1. First we summed up each scaler count over a current interval of 0.4mA from 0.2mA to 3.0mA. Then we converted them to count per unit time (Hz). This procedure was done as follows. As mentioned in Sec.3.5, we counted the number of electron's revolution in the damping ring simultaneously. This gave actual data taking time since the revolution frequency was accurately known (2.1645MHz). Thus we divided the summed scaler counts by the data taking time determined in this way.

2. Next we plotted the count rate(Hz) as a function of the laser intensity level (LL1 - LL5). Fig.4.3 shows two examples of such plots. The par-

Table 4.1: Category of scaler count classification.

Item	Divisions	Intervals	Comments
Energy of scattered photons (MeV)	4	5-15 , 15-25 25-35 , 35-	taken simultaneously in one run
Electron current (mA)	7	0.4 interval from 0.2 to 3.0	at different time in one run
Laser intensity (a.u)	5	LL1, LL2, LL3 LL4, LL5	taken simultaneously in one run
Laser wire positions (μm)	20-21		in separate runs

ticular data, taken on (2000/12/05), correspond to the energy range of 15-25 MeV, and the electron current of 0.2-0.6mA. The left figure shows the plot with the laser wire on the electron beam while the right off the electron beam. Clear linear dependence of the count rate upon the laser intensity is seen. The solid lines in Fig.4.3 show the results of linear fit. These straight lines were extrapolated to the point corresponding to the laser maximum intensity, *i.e*, the cavity's maximum energy realized at the peak of Airy function. The arrows in Fig.4.3 indicate the extrapolation. Finally, the signal count rate was defined by the difference between the maximum count rate and the minimum count rate corresponding to the zero laser intensity.

3. Then the signal count rate(Hz) was normalized to the electron beam current. The resultant quantities are called normalized signal rate (Hz/mA).

4. Finally, we plotted the normalized signal rate(Hz/mA) as a function of the laser wire position.

The procedure 2 was needed to prove linear enhancement of the obtained count rate with laser intensity and also to retain the data's most of their statistical power. In order to check goodness of the linear fit in the procedure 2, we calculated the chi-square (χ^2) per degree of freedom (ν) for each run. The resultant values, very close to $\chi^2/\nu = 1$, indicate goodness of the fit as well as the data.

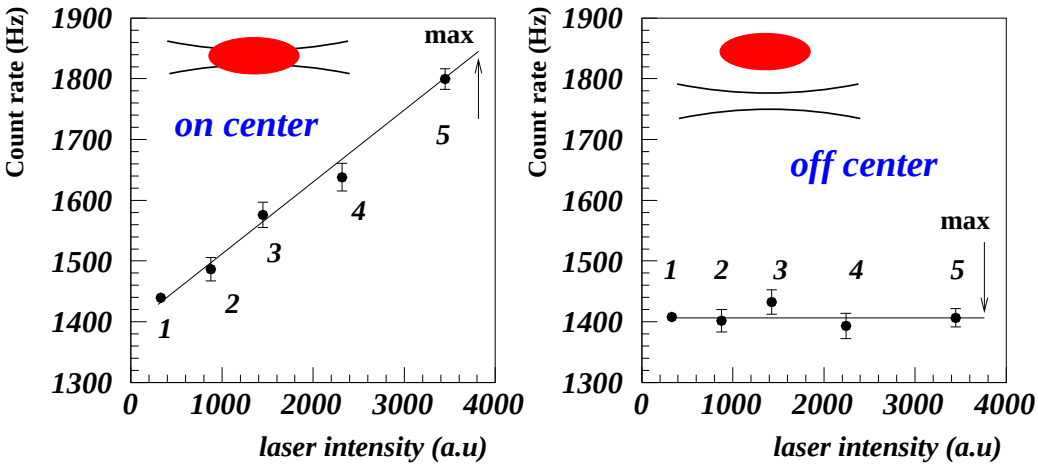

Figure 4.3: Count rate vs laser intensity. (Left) The laser wire on the electron beam. (Right) The laser wire off the electron beam.

4.1.3 Results of vertical beam size measurements

In the previous subsection, we obtained signal rates classified according to the electron beam current, detected photon energy, and laser wire position. In this subsection, we will obtain vertical beam sizes from these data. In order to illustrate the analysis procedure, we will take the data for 1.0-1.4 mA as an example. Fig.4.4, Fig.4.5 and Fig.4.6 show signal rates as a function of the laser wire vertical positions for 4 energy bins. The solid lines (gaussian fits) in the figures will be explained in Sec.4.1.4. As expected, the Compton signals are mainly seen in the energy interval of 5-15 MeV and 15-25 MeV. On the other hand, the signal rates above the Compton energy (35MeV -) are consistent with zero. The chi-square(χ^2) per degree of freedom (ν) resulted from the zero constant fitting for these data are $\chi^2/\nu = 16.59/21$ (2000/12/05), $\chi^2/\nu = 21.84/21$ (2000/12/07) and $\chi^2/\nu = 21.03/20$ (2000/12/14). Thus, they are statistically consistent with zero, as expected.

Having confirmed that the Compton signals were only seen in the 5-25 MeV range for all the data (at any electron currents), we combined the data in 5-15 MeV and 15-25 MeV regions. Then we fitted to the data a gauss function with a center, width and peak height being left as free parameters. Fig.4.7, Fig.4.8 and Fig.4.9 show the measured beam profiles obtained in this way. The solid curves are resulted gauss functions. We defined the vertical beam size (σ_{obs}) by the width of fitted gauss functions. Table.4.2 lists our final results for σ_{obs}. The errors in parentheses will be explained below. The figures on the left in Fig.4.10 shows σ_{obs} versus I_e. As expected, the beam size for the 2nd data set (2000/12/07) was significantly larger.

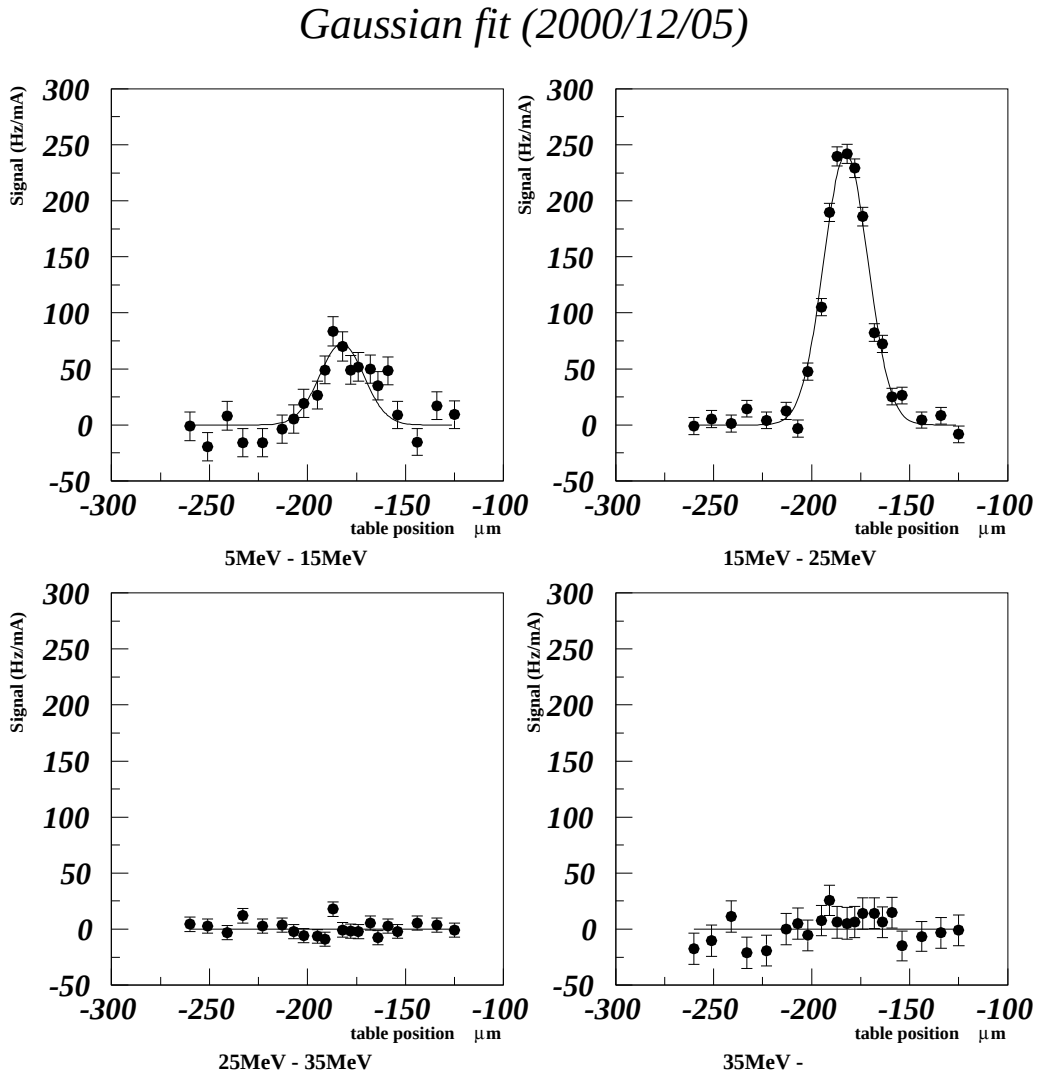

Figure 4.4: Normalized signal count vs the laser wire position. Plots for 4 different energy intervals labeled at the bottom with the same electron beam current [1.0 - 1.4mA]. Data from (2000/12/05)

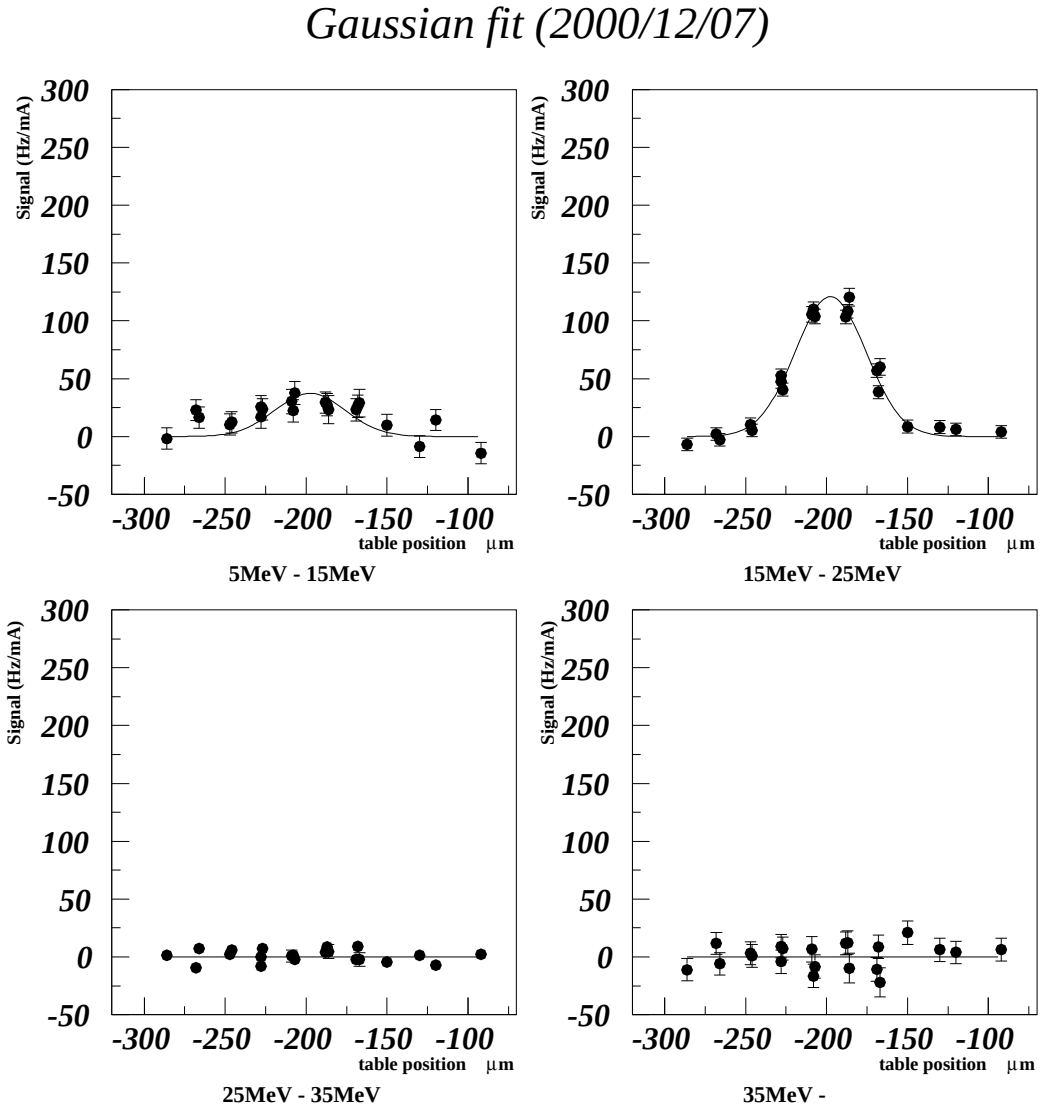

Figure 4.5: Normalized signal count vs the laser wire position. Plots for 4 different energy intervals labeled at the bottom with the same electron beam current [1.0 - 1.4mA]. Data from (2000/12/07)

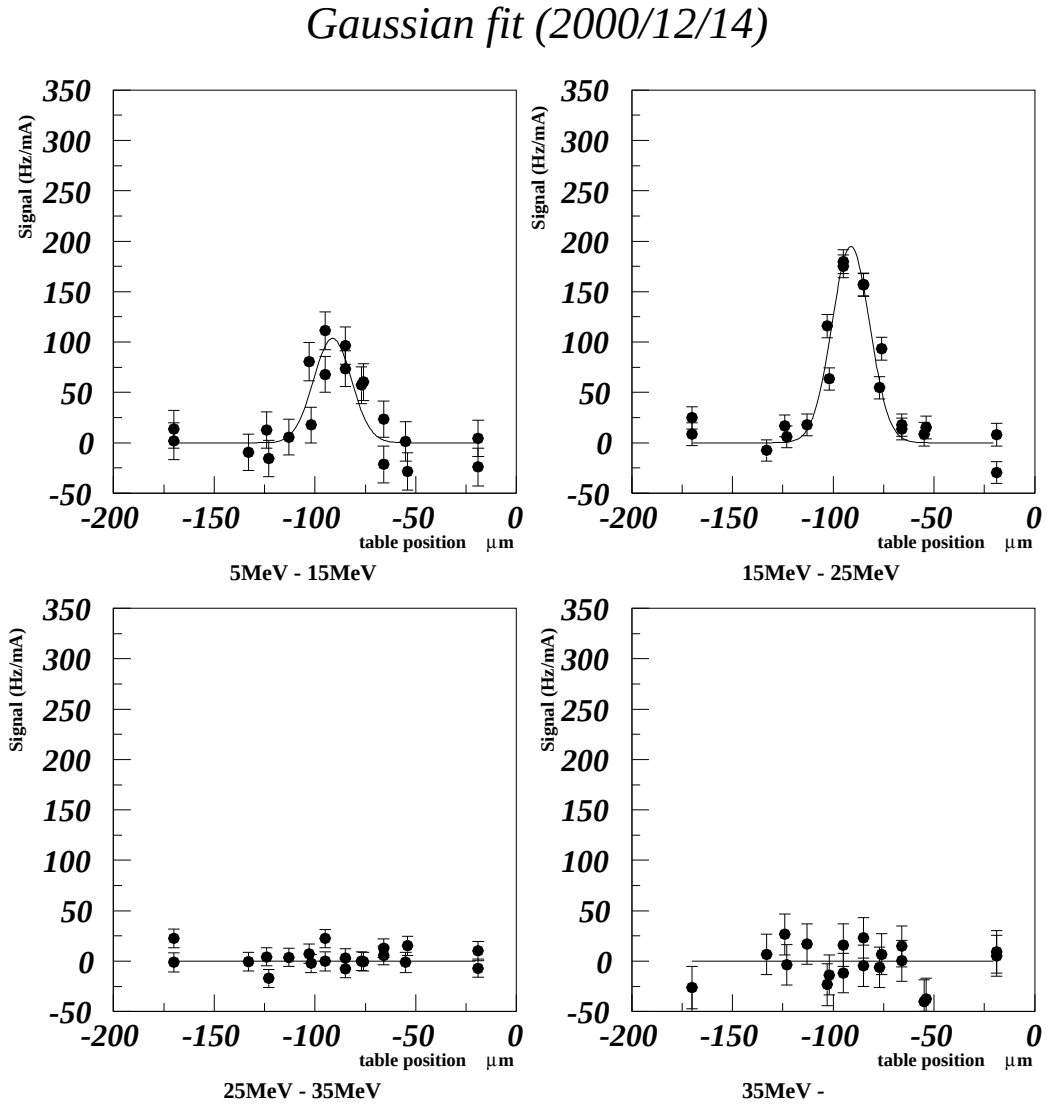

Figure 4.6: Normalized signal count vs the laser wire position. Plots for 4 different energy intervals labeled at the bottom with the same electron beam current [1.0 - 1.4mA]. Data from (2000/12/14)

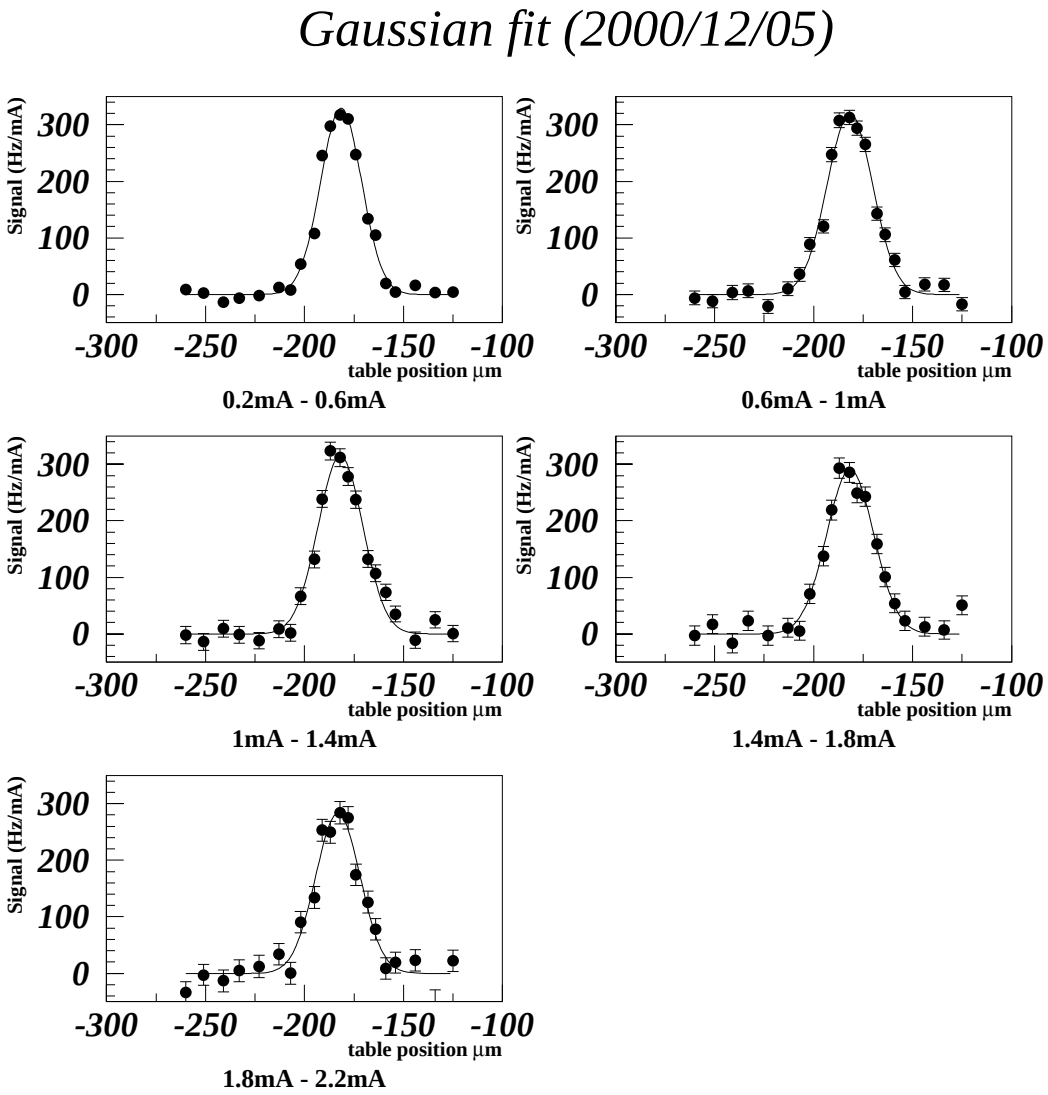

Figure 4.7: Normalized signal count vs the laser wire position. Plots for 5 different electron currents indicated by the subtitle. Each plot contains combined data of the energy interval 5 - 25 MeV. Data taken on (2000/12/05)

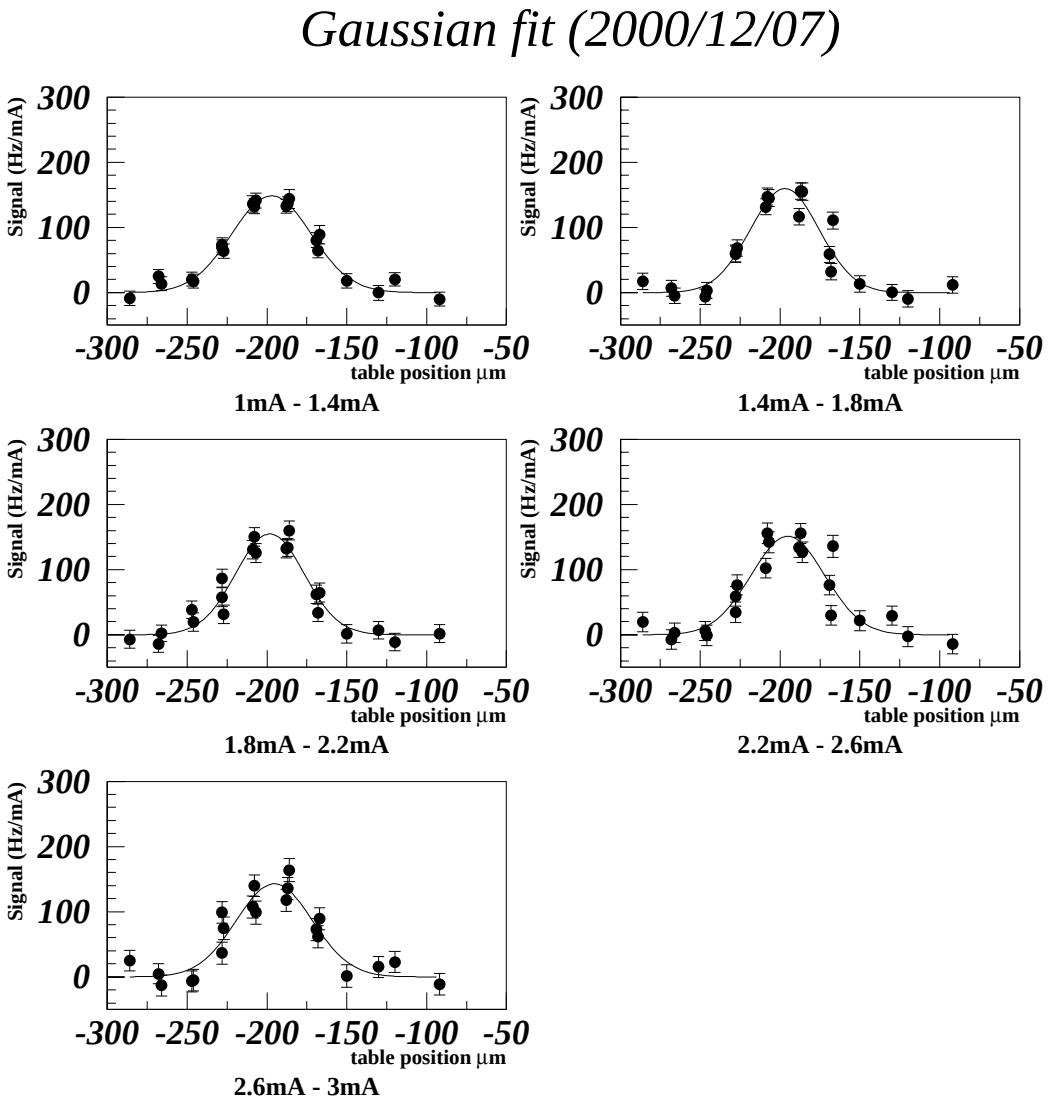

Figure 4.8: Normalized signal count vs the laser wire position. Plots for 5 different electron currents indicated by the subtitle. Each plot contains combined data of the energy interval 5 - 25 MeV. Data taken on (2000/12/07)

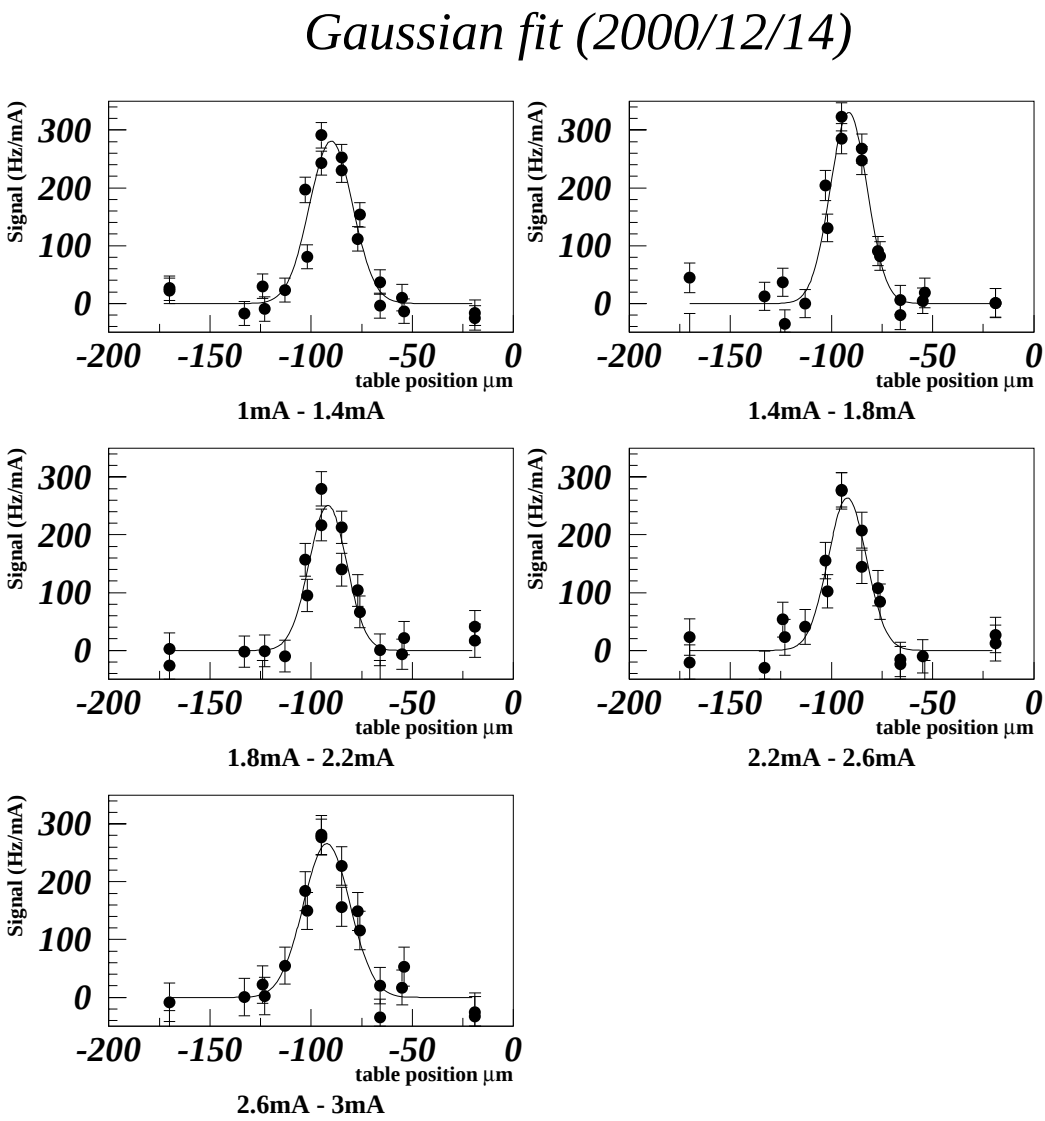

Figure 4.9: Normalized signal count vs the laser wire position. Plots for 5 different electron currents indicated by the subtitle. Each plot contains combined data of the energy interval 5 - 25 MeV. Data taken on (2000/12/14)

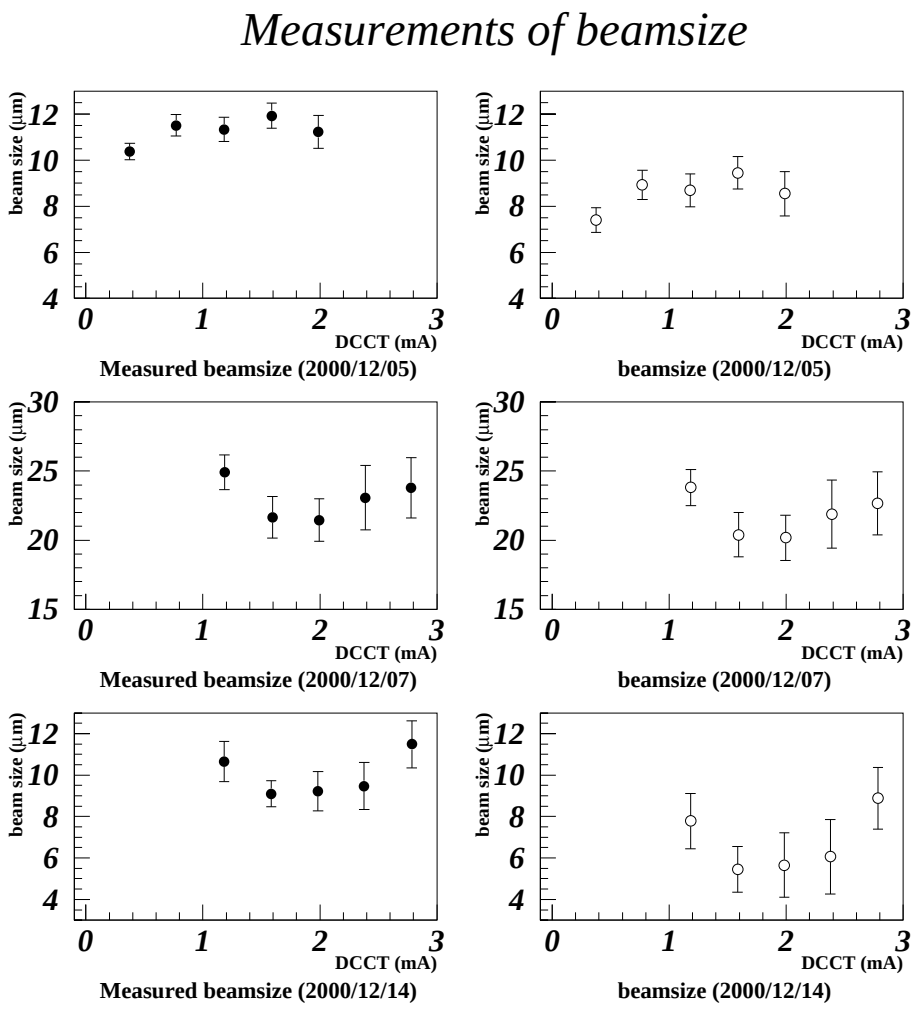

Figure 4.10: Beam size vs the electron current. Beam size σ_{obs} (left) and σ_y (right). Data taken on (2000/12/05) (top), (2000/12/07) (middle) and (2000/12/14) (bottom).

Table 4.2: Summary of the measurements of the beam size σ_{obs}

date	Current(mA)	beam size σ_{obs} (μm)	χ^2	ν
(2000/12/05)	0.4	10.38 $\pm$ 0.22 ($\pm$ 0.35)	46.6	18
	0.8	11.51 $\pm$ 0.32 ($\pm$ 0.47)	38.2	18
	1.2	11.34 $\pm$ 0.41 ($\pm$ 0.53)	31.0	18
	1.6	11.93 $\pm$ 0.48 ($\pm$ 0.55)	23.4	18
	2.0	11.23 $\pm$ 0.25 ($\pm$ 0.72)	29.3	18
(2000/12/07)	1.2	24.91 $\pm$ 1.25 ($\pm$ 1.25)	15.2	18
	1.6	21.65 $\pm$ 1.05 ($\pm$ 1.51)	37.4	18
	2.0	21.45 $\pm$ 1.28 ($\pm$ 1.53)	25.9	18
	2.4	23.07 $\pm$ 1.52 ($\pm$ 2.33)	41.9	18
	2.8	23.80 $\pm$ 1.67 ($\pm$ 2.17)	30.2	18
(2000/12/14)	1.2	10.65 $\pm$ 0.65 ($\pm$ 0.96)	36.6	17
	1.6	9.09 $\pm$ 0.56 ($\pm$ 0.63)	21.6	17
	2.0	9.22 $\pm$ 0.80 ($\pm$ 0.94)	23.1	17
	2.4	9.47 $\pm$ 1.03 ($\pm$ 1.14)	21.1	17
	2.8	11.48 $\pm$ 1.13 ($\pm$ 1.14)	17.3	17

In the gaussian fit, we did not include a constant term. This is because we removed, in principle, all the backgrounds in calculating the signal rates (the linear fit procedure described in Sec.4.1.2). In Table.4.2, the 4th and 5th columns are resultant χ^2 and ν for the fits. We expect these χ^2 values would distribute around ν if they obey statistics. In reality, however, χ^2/ν's are significantly larger than unit, indicating that there might be some systematic effects. They could be attributed to, for example, jitter and/or drift in the electron beam position. Since we have not identified their sources yet, we took a conservative way. Namely, we enlarged uniformly all error bars so that resultant χ^2/ν's became unit. New errors on σ_{obs} are listed in the parentheses in Table.4.2. We employ these values in the following analysis.

4.1.4 Energy spectrum

In this subsection, we will examine our data from the view point of the Compton process. The main purpose is to demonstrate that the observed signal rates and their energy spectrum are consistent with the expected ones.

To this end, we first fit a gauss function to the data shown in Fig.4.4 - Fig.4.6. In this case, the height of the gauss functions was the only free

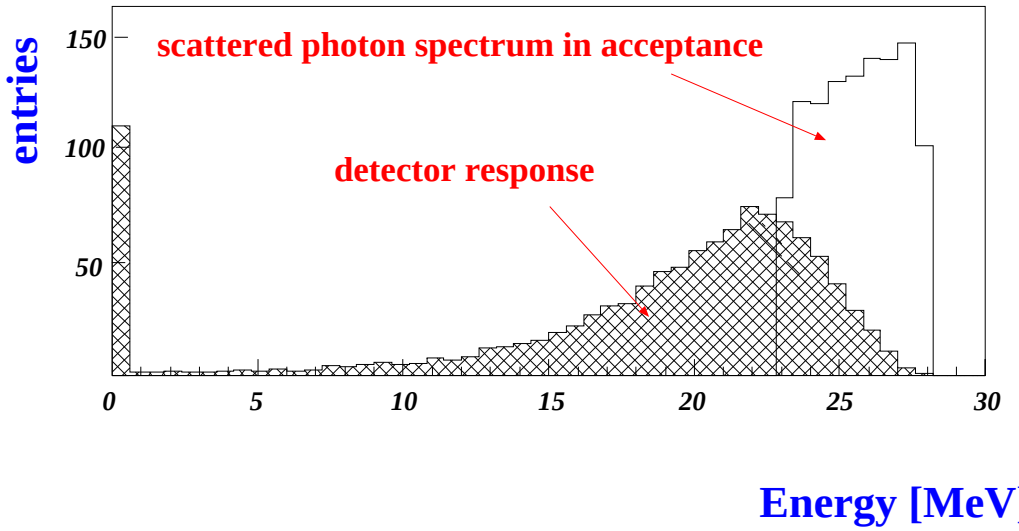

Figure 4.11: Expected energy spectrum. Unhatched histogram shows the expected energy spectrum of scattered photon through a 5mm bore collimator. Hatched histogram represents the deposit energy spectrum in the detector.

parameter, with the center and width being given by those obtained in Fig.4.7 - Fig.4.9. The Compton signal rate at each energy was defined by the peak value of the resultant gauss functions. Fig.4.12 shows the plot of the signal rate vs the energy region.

We now want to compare the observed energy spectrum with the calculated one. To this end, we must fold our detector response in the theoretical spectrum given by Eq.(2.38). We calculate experimental count rate $N_{exp}(k')$ by

$$\frac{dN_{exp}(k')}{dk'} = \int_{k_{th}}^{k_{max}} \frac{d\varepsilon(k_s)}{dk'} \cdot \frac{dN}{dk_s} dk_s, \tag{4.1}$$

where $\varepsilon(k_s)$ represents the detector response function to a photon with energy k_s, and k' means observed energy in the CsI(pure) scintillator. $\varepsilon(k_s)$ is simulated by a code named EGS4 [31]. Fig.4.11 shows both unfolded (unhatched) and folded (hatched) energy spectrum. The former is the expected energy spectrum of scattered photons passing through a 5mm bore collimator. The latter represents the deposit energy spectrum in the detector. The minimum energy $k_{th} = 23$ MeV is determined by the collimator's bore radius (5mm) and the maximum energy $k_{max} = 28.6$ MeV by Eq.(2.29). The following numerical values are used to calculate Eq.(4.1). The laser intensity W inside the cavity was estimated with the injected laser intensity of 72mW

and the enhancement factor of 220 ± 20, and the matching efficiency with the optical cavity of 0.7. We inserted the measured value $\sigma_{obs} = 11.34 \pm 0.53\mu$m (2000/12/05), $24.91 \pm 1.25\mu$m (2000/12/07) and $10.65 \pm 0.96\mu$m (2000/12/14) for $\sqrt{\sigma_y^2 + \xi^2}$ in Eq.(2.38). Finally, we used $N_e = 10^{10}$ with $\beta_e = 1$, and $k_0 = 2.33$eV. Uncertainty of the estimate came mainly from the laser power uncertainty and measured beam size error. In addition, we included alignment error of the collimator ($\pm 1mm$) and 10% error in the setting of the detector threshold. The hatched boxes in Fig.4.12 shows the expected count rate and its uncertainty range. The measured count rates are in good agreement with the expected ones.

4.2 Measurements of the beam waist

The laser's beam waist w_0 is one of the most important parameters in the cavity. We established three independent methods to measure w_0, and found that all agree well with each other [32]. In this experiment, however, we applied two of them to this optical cavity. One method was to measure beam divergence from the optical cavity (*beam divergence method*), while the other was to excite the higher order mode (*transverse method*) [33].

Actually, beam waists were measured twice before and after the measurements of the vertical emittance.

4.2.1 Beam divergence method

Principle The beam spot size $w(z)$ at the distance z from the center of the optical cavity is represented by $w(z) = w_0\sqrt{1 + (z/z_0)^2}$, where z_0 is the Reighly length. If $z \gg z_0$, we can approximate it as

$$w(z) = \frac{\lambda z}{\pi w_0} \tag{4.2}$$

Thus the beam waist can be determined by measuring the beam divergence $w(z)$ at various z positions. Fig.4.13 shows a schematic diagram of the beam divergence measurement. First, an intensity profile of the transmitted beam is measured by scanning a PIN photodiode with a narrow slit in front. The measurements are done at 4 different z positions ($z_1 \sim z_4$). Each profile should be a gaussian with a width of $w(z)/2$. We perform a simple gaussian fit to the measured profile to obtain an experimental width $\sigma(z)$. When $\sigma(z)$'s are plotted as a function z, they should satisfy the linear relation

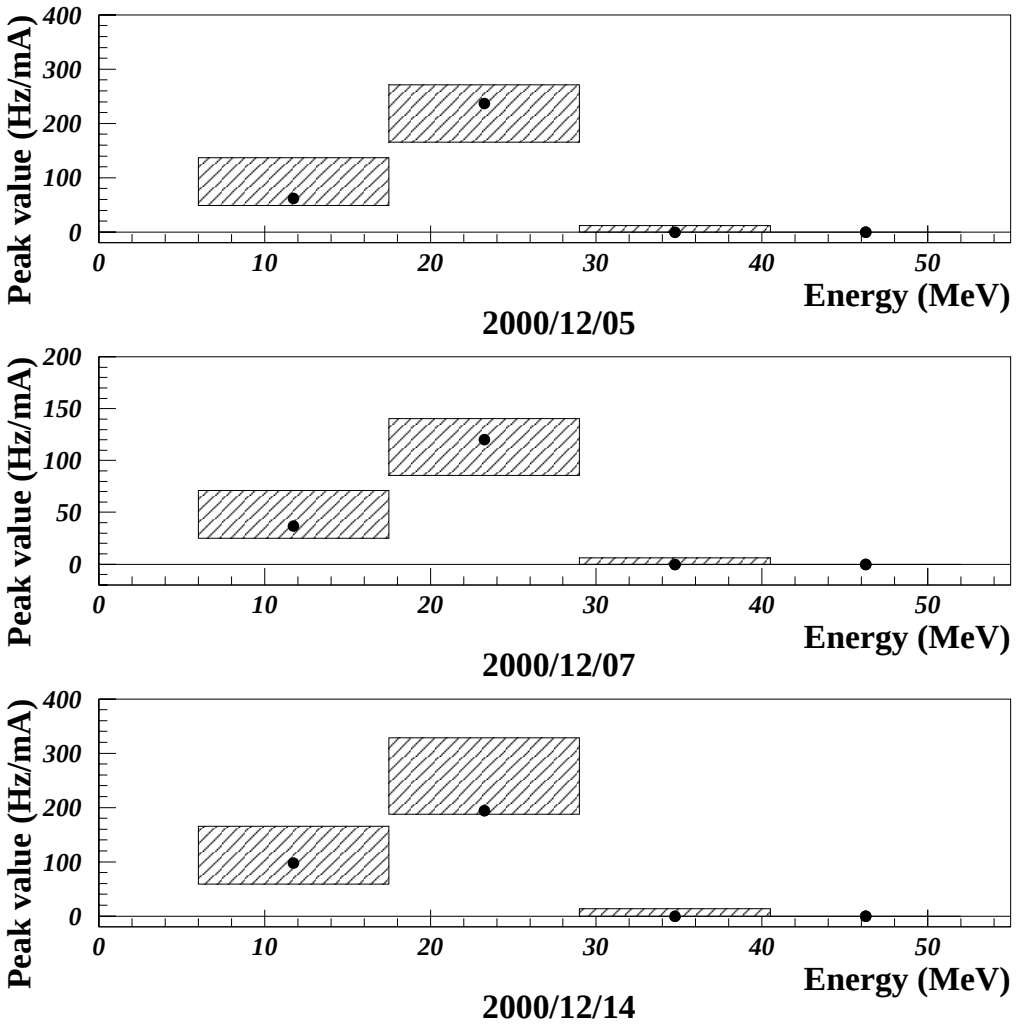

Figure 4.12: Normalized signal rate vs energy. Solid circles shows measured signal rate for each energy region. The hatched boxes shows the expected signal rate and its uncertainty range.

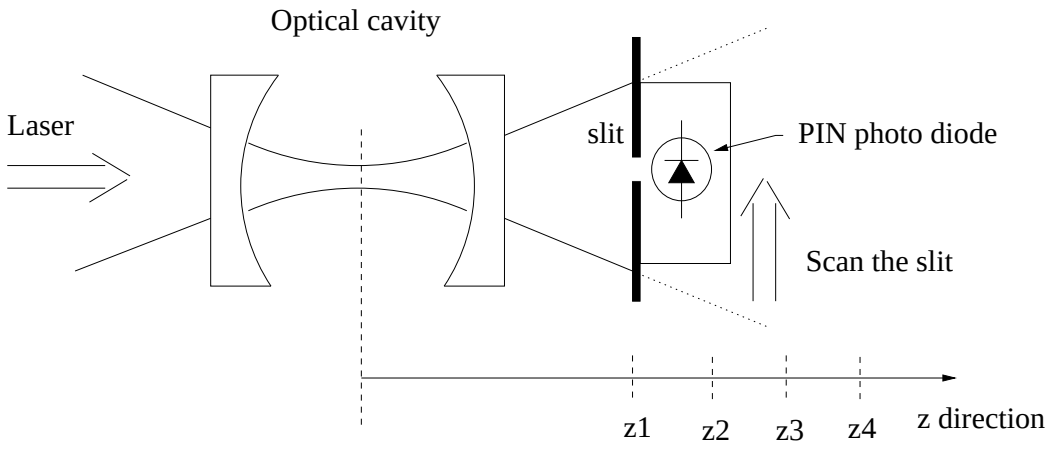

Figure 4.13: Schematics of beam divergence method. By moving the PIN photodiode perpendicular to the laser beam, we can measure the laser beam profile.

$$\sigma(z) \equiv \frac{w(z)}{2} = \frac{\lambda}{2\pi w_0} \times z \equiv a \times z \tag{4.3}$$

The beam waist parameter w_0 can be obtained from a slope of these plots. There is one minor detail in the measurement; since the cavity mirror acts as a concave lens, the beam divergence angle is altered. When this effect is taken into account, the slope now becomes

$$a = \frac{n\lambda}{2\pi w_0}, \tag{4.4}$$

where n is the index of the mirror ($n = 1.519$).

Results The actual measurements were carried out twice; before (2000/11/19) and after (2000/12/18) the emittance measurements. Fig.4.14 and Fig.4.15 show the beam profiles at each z position. Note that the nearest point to the cavity is defined to be $z = 0$ in this plot. (See below for justification.) The width $\sigma(z)$ was deduced from a fitted gauss function to the data points. The solid curves in Fig.4.14 and Fig.4.15 are the resultant gauss functions. We assigned an error on $\sigma(z)$ in the following manner. Since there were no errors assigned to the original PIN photodiode reading, a common error was given in such a way that $reduced-\chi^2$ (χ^2/ν) of the fit became unit. Fig.4.16 shows $\sigma(z)$ as a function z. We note that since we are interested in the slope of

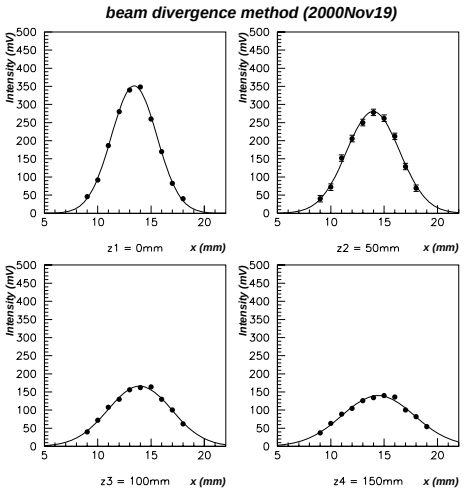

Figure 4.14: Measured beam profile for 4 different z position. Data taken on (2000/11/19). The data points are fitted with a simple gauss function.

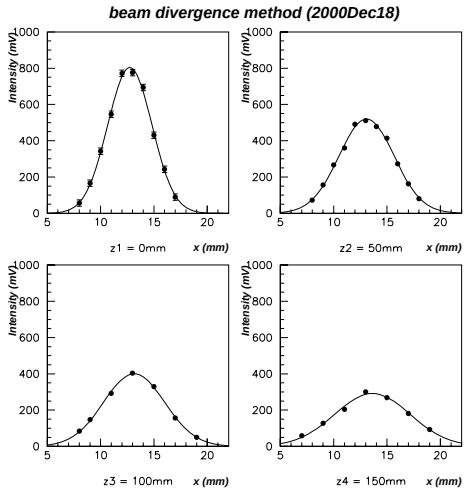

Figure 4.15: Measured beam profile for 4 different z position. Data taken on (2000/12/18). The data points are fitted with a simple gauss function.

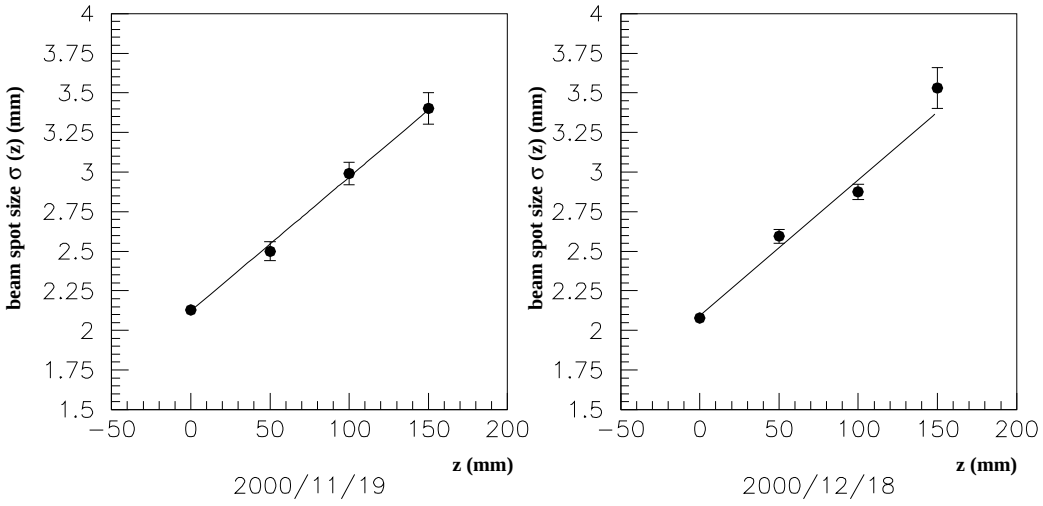

Figure 4.16: Beam width vs z position. Data taken on (2000/11/19) (left) and (2000/12/18) (right). Solid lines show the results of linear fits.

these plots, only relative distance matters between different z points. Finally w_0 was deduced from the relation $a = \frac{n\lambda}{2\pi w_0}$ with $n = 1.519$ and $\lambda = 532$nm. We summarize the obtained results in Table.4.3.

Table 4.3: Summary of beam waist measurements by the beam divergence method

date	measured beam waist w_0
2000/11/19	15.03 ± 0.91 μm
2000/12/18	15.22 ± 0.94 μm
average	15.12 ± 0.65 μm

We emphasize that the two measured values agree well with each other, indicating that the beam waist remained constant during the emittance measurements. Therefore we averaged over the two measurement results to obtain $w_0 = 15.12 \pm 0.65\mu$m.

4.2.2 Transverse method

Principle Next we describe another method to measure the beam waist. The beam waist w_0 is determined by, apart from the wave length λ, the mirror curvature ρ and the cavity length D, as given by Eq.(2.15). Among the two parameters, ρ is found to be $\rho = 20.0000$mm $\pm$ 0.5μm by a separate measurement. Now the measurement of w_0 amounts to the measurement of D. To this end, we consider higher transverse modes. The phase of a higher transverse mode $\mathrm{TEM_{mn}}$ is given by

$$\phi(z) = -\frac{2\pi}{\lambda} z + (m + n + 1)\,\Phi(z),$$

where $\Phi(z)$ is given by Eq.(2.13). The transverse mode in the cavity interferes constructively when the phases at the mirrors ($z = \pm D/2$) satisfy the resonance condition

$$\phi(-D/2) - \phi(D/2) = p\pi,$$

where p denotes an integer. A straightforward calculation shows that the condition above is equivalent to

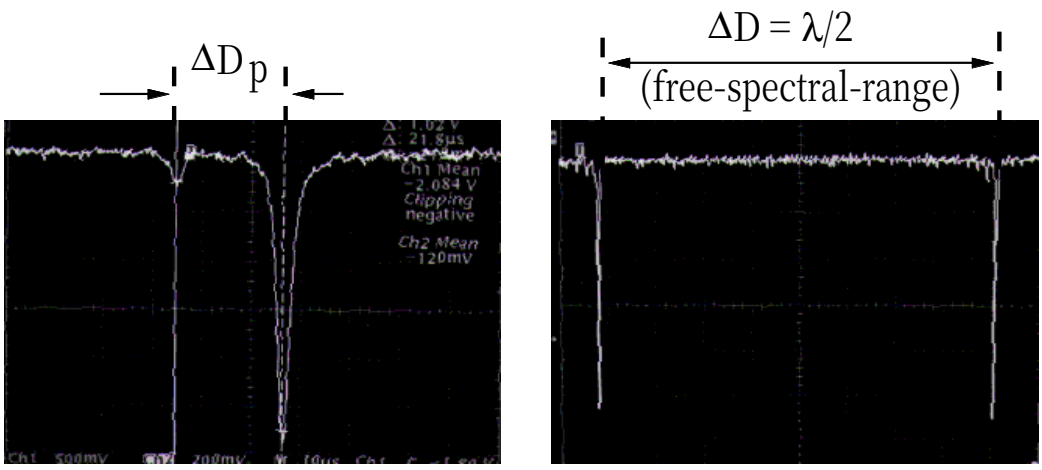

Figure 4.17: Transmitted laser intensity from the cavity. Two main peaks (right) and the main peak and sub-peak (left). They provide, respectively, ΔD and ΔD_p.

$$D_p = \frac{\lambda}{2}\left\{p + \frac{m+n+1}{\pi}\arccos\left(\frac{D_p}{\rho} - 1\right)\right\}. \tag{4.5}$$

The transmitted beam intensity also exhibits its maximum value when the resonance condition is met. Therefore, the spacing between the adjacent peaks belonging to the same p is given by

$$\Delta D_p = D_p(m+n=1) - D_p(m+n=0) = \frac{\lambda}{2}\left[\frac{1}{\pi}\arccos\left(\frac{D}{\rho} - 1\right)\right], \tag{4.6}$$

where the quantity D_p on the right hand side of Eq.(4.5) is replaced by a representative value D since its dependence is weak. Thus we can determine D by measuring the spacing ΔD_p of the two peaks. As represented in Eq.(4.6), we actually measured the spacing between the first excitation mode $(m+n=1)$ and the fundamental mode $(m+n=0)$.

These measurements were done by the same setup for the measurement of the finesse. After confirming the cavity to be in the fundamental TEM_{00} mode, we detuned the optical axis by shifting one of the matching section transversely to excite the transverse mode. Fig.4.17 shows a typical example of an output of fundamental and higher transverse modes. We determined the spacing between the main peak (the fundamental mode) and the adjacent peak (the first excitation mode), as shown on the left picture of Fig.4.17 as

Table 4.4: Summary of the beam waist measurement by the transverse method

date	beam waist w_0 on each airy function	average	r.m.s error
2000/11/19	14.58 μm		
	14.10 μm	13.86 μm	$\pm$ 0.74 μm
	12.63 μm		
	14.13 μm		
2000/12/18	14.16 μm		
	14.25 μm	14.23 μm	$\pm$ 0.05 μm
	14.27 μm		
average	14.02 $\pm$ 0.59 μm		

well as the spacing between two main peaks (FSR) as shown on the right picture in Fig.4.17. The spacing of FSR is equal to $\lambda/2$. Then we deduced the cavity length D via Eq.(4.6).

Results We could observe seven main peaks by modulating the piezo actuator with an amplitude of 3μm. Repeating the measurement for different main peaks (and sub-peaks), we obtained four values on (2000/11/19) and three values on (2000/12/18). Then we averaged these values, and calculated r.m.s deviations. The results are summarized in Table.4.4.

We notice that the r.m.s error for the (2000/11/19) data is much bigger than the other. This comes from one exceptionally small value (12.63μm) in the data. Although we cannot reject the possibility of a simple mistake in that data point, it is conservative to retain it and allow the error (r.m.s deviation) to become much larger that it would be without it. The two averaged value obtained different days agree well with each other. Thus, we conclude that the beam waist remained unchanged during the emittance measurements: the same conclusion from the divergence method. We simply average all the data to obtain a representative value: $w_0 = 14.02 \pm 0.59\mu$m. The error is a r.m.s deviation of all the measured values.

4.2.3 Summary of the beam waist measurements

The values for w_0 obtained by the two methods are

$$w_0 \quad = \quad 15.12 \pm 0.65(\mu m). \quad \text{(beam divergence)}$$

$$w_0 \;=\; 14.02 \pm 0.59(\mu m). \quad \text{(transverse method)}$$

Thus we conclude that they agree very well each other, and we can average the two. The result is

$$w_0 = 14.52 \pm 0.44(\mu m).$$

Hereafter, we used this value for w_0 and treat it to be constant throughout the emittance measurements.

4.3 Measurements of the β function and other damping ring parameters

4.3.1 β measurement at quadrupole magnets

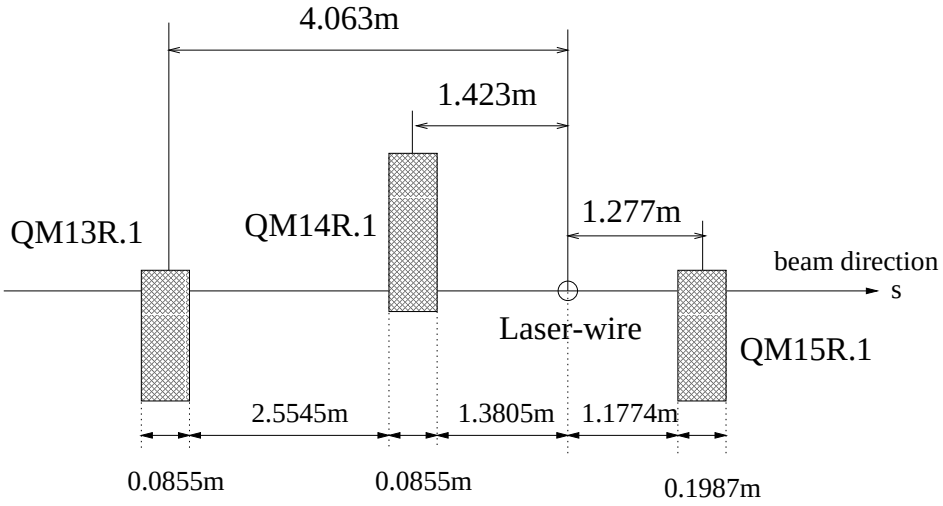

Figure 4.18: Layout of quadrupole magnets near the laser wire.

The β function were measured at the three quadrupole magnets near the laser wire. They are called 'QM13R.1', 'QM14R.1' and 'QM15R.1', respectively. Fig.4.18 shows the location of these magnets. Referring to the horizontal direction, 'QM14R.1' is a focusing magnet, and 'QM13R.1' and 'QM15R.1' are defocusing magnets. Their quadrupole strength K (k-value) are -0.5133, 0.5061, -1.1159, respectively.

Since the damping ring might have been tuned differently, we carried out the measurement simultaneously with the vertical emittance measurements.

Thus, in the following, we will present three sets of data. Fig.4.19, Fig.4.20 and Fig.4.21 show the results of these three measurements. The horizontal axis show the shift of k-value ΔK and the vertical axis is the value of $\cos\mu(\mu = 2\pi\nu)$. Plots on the left (right) show the horizontal(x) (vertical (y)) tune measurement.

Considering Eq.(3.6), we performed a linear fit of the form,

$$\cos\mu = A \cdot \Delta K + B, \tag{4.7}$$

where A and B are free parameters to be determined. From the relation, $A = \beta_0 \sin(2\pi\nu_0)/2$ and $B = \cos(2\pi\nu_0)$, we deduced β_0 and ν_0. The results are shown in Table.4.6 and Table.4.5. In the β-measurement, errors were assigned so that the resultant $\chi^2/\nu = 1$.

Table.4.5 shows the nominal tune of the measurements. We note the data of (2000/12/05) and (2000/12/07) agree very well with each other. However the data of (2000/12/14) are different from the other two. From the data, we conclude that the optics of the 3rd measurement is different from that of previous two.

Table 4.5: Measured nominal tune

tune	2000/12/05	2000/12/07	2000/12/14
ν_x	15.184	15.182	15.151
ν_y	8.5809	8.5845	8.5118

Table 4.6: Measured β function at each quadrupole magnet

date	measured β	QM13R.1	QM14R.1	QM15R.1
2000/12/05	β_x (m)	4.38 $\pm$ 0.42	24.3 $\pm$ 0.55	2.46 $\pm$ 0.05
2000/12/05	β_y (m)	9.41 $\pm$ 0.33	2.88 $\pm$ 0.19	9.97 $\pm$ 0.07
2000/12/07	β_x (m)	4.35 $\pm$ 0.55	24.4 $\pm$ 0.36	2.49 $\pm$ 0.08
2000/12/07	β_y (m)	9.09 $\pm$ 0.75	2.23 $\pm$ 0.12	10.4 $\pm$ 0.08
2000/12/14	β_x (m)	5.14 $\pm$ 0.62	27.5 $\pm$ 0.40	2.90 $\pm$ 0.06
2000/12/14	β_y (m)	11.6 $\pm$ 0.36	2.85 $\pm$ 0.60	6.91 $\pm$ 0.16

4.3.2 Determination of the β function at the laser wire

Next we determined the β function at the laser wire. Two sets of the twiss parameters α, β and γ at s_1 and s_2 on the ring are related to each other via

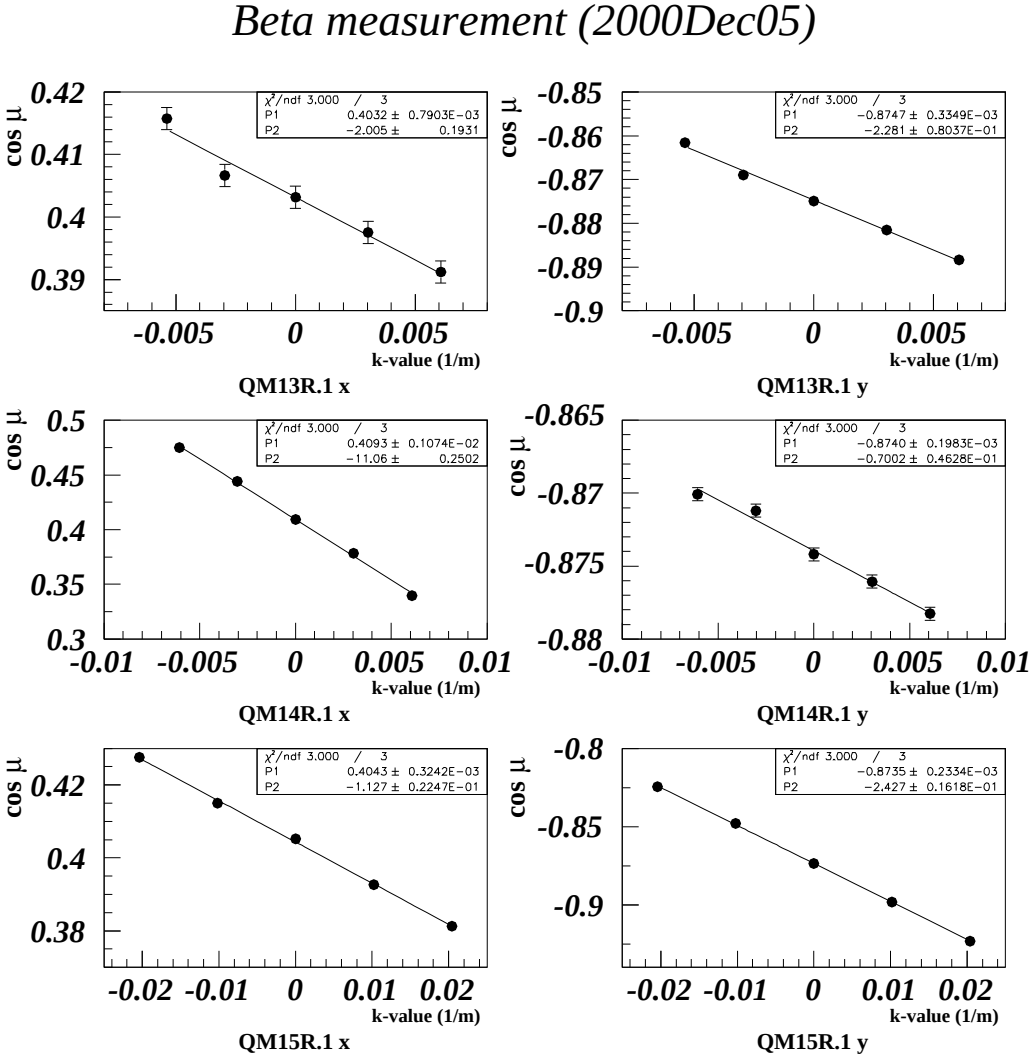

Figure 4.19: $\cos\mu$ vs ΔK. The linear fits to the data points, shown by the solid lines, give the β function. Subtitle of each plot represents the magnet and direction. Taken on (2000/12/05).

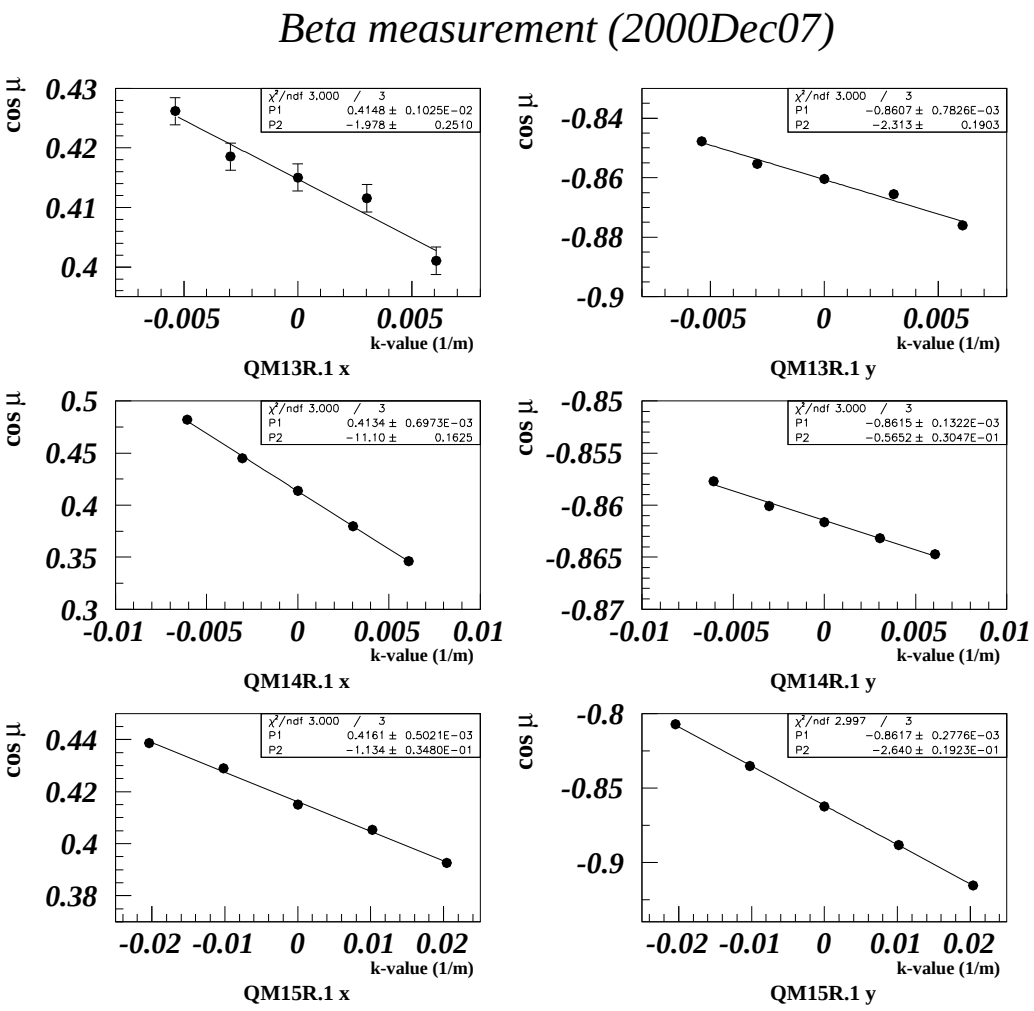

Figure 4.20: $\cos\mu$ vs ΔK. The linear fits to the data points, shown by the solid lines, give the β function. Subtitle of each plot represents the magnet and direction. Taken on (2000/12/07).

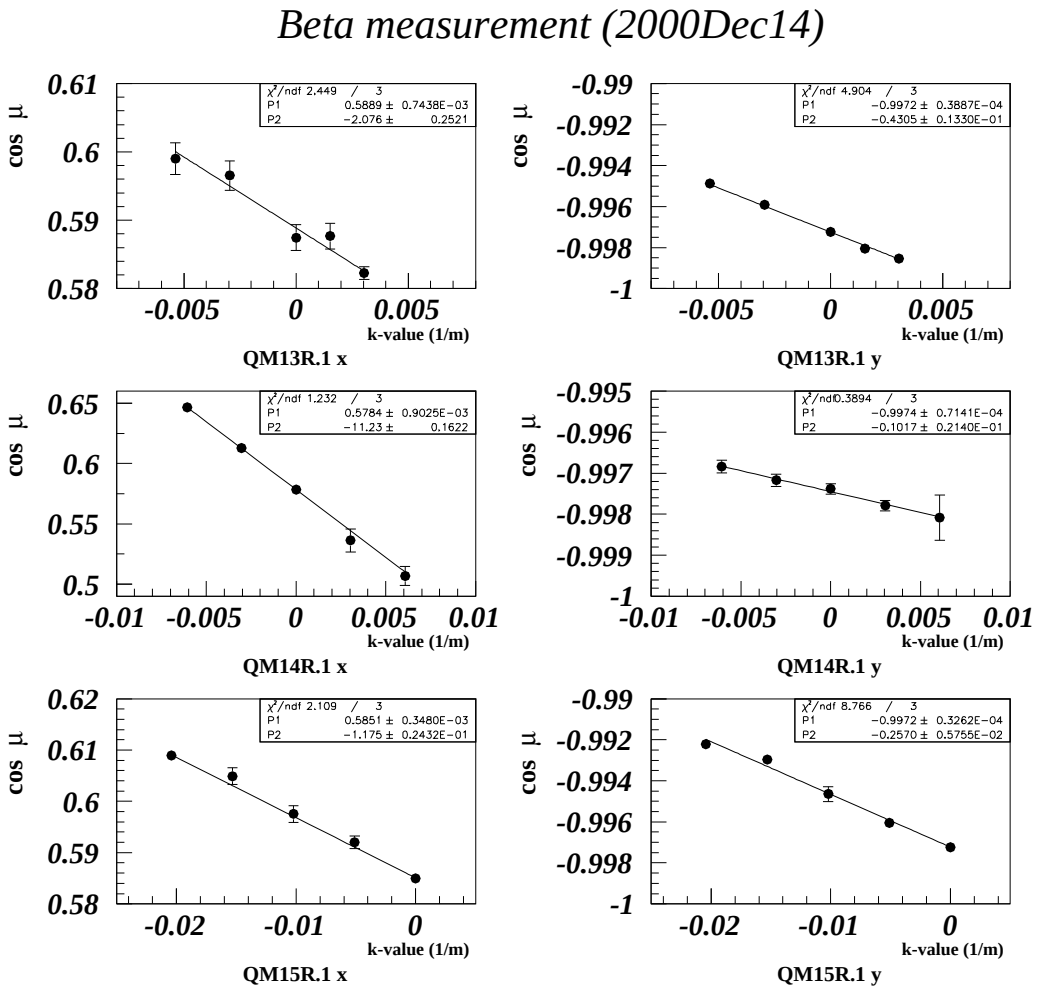

Figure 4.21: $\cos\mu$ vs ΔK. The linear fits to the data points, shown by the solid lines, give the β function. Subtitle of each plot represents the magnet and direction. Taken on (2000/12/14).

the transfer matrix $M(s_2, s_1)$. The relation, given explicitly by Eq.(A.26), can be rewritten as

$$\begin{pmatrix} \beta(s_2) \\ \alpha(s_2) \\ \gamma(s_2) \end{pmatrix} = \begin{pmatrix} M_{11}^2 & -2M_{11}M_{12} & M_{22}^2 \\ -M_{11}M_{21} & 1+2M_{12}M_{21} & -M_{12}M_{22} \\ M_{21}^2 & -2M_{22}M_{21} & M_{22}^2 \end{pmatrix} \begin{pmatrix} \beta(s_1) \\ \alpha(s_1) \\ \gamma(s_1). \end{pmatrix} \quad (4.8)$$

It indicates that, if we know the transfer matrix from one of the quadrupole magnets to the laser wire, we can determine the β function at the laser wire.

In reality, we did the opposite; given a set of the twiss parameters (α_{LW}, β_{LW}) at the laser wire, we predicted them at each quadrupole magnet, and compared them with the measured values. We defined chi-square (χ^2) by

$$\chi^2(\alpha_{LW}, \beta_{LW}) = \sum_{n=QM13}^{QM15} \left(\frac{\beta_{n,meas} - \beta_n(\alpha_{LW}, \beta_{LW})}{\sigma_{n,meas}} \right)^2, \quad (4.9)$$

where the suffix n specifies the quadrupole magnets and *meas* means the measured β functions with errors given in the previous paragraph. Fitting was carried out to minimize $\chi^2(\beta_{LW}, \alpha_{LW})$, and the results are presented in Table.4.7. Fig.4.22 shows the optics obtained in this way.

Table 4.7: Summary of the β function at laser wire.

date	direction	β_{LW} (m)	α_{LW}	χ^2
2000/12/05	x	9.71 $\pm$ 0.07	4.03 $\pm$ 0.04	2.35
2000/12/05	y	5.77 $\pm$ 0.07	-1.51 $\pm$ 0.02	1.84
2000/12/07	x	9.73 $\pm$ 0.10	4.02 $\pm$ 0.05	1.33
2000/12/07	y	5.65 $\pm$ 0.14	-1.67 $\pm$ 0.05	1.81
2000/12/14	x	11.1 $\pm$ 0.08	4.53 $\pm$ 0.04	3.67
2000/12/14	y	3.97 $\pm$ 0.17	-1.00 $\pm$ 0.03	1.35

4.3.3 Summary of the damping ring parameters

We summarize the measured parameters in the damping ring in Table.4.8. Momentum spread σ_p/p was measured at the extraction line using a screen monitor. Momentum compaction factor α_M is estimated from Eq.(A.63) by measuring synchrotron oscillation frequency f_s and RF voltage V_{RF}. η_x and η_y were also measured during the procedure of the dispersion correction. Due to poor resolution of the BPM, we can only set the upper limit of dispersion functions.

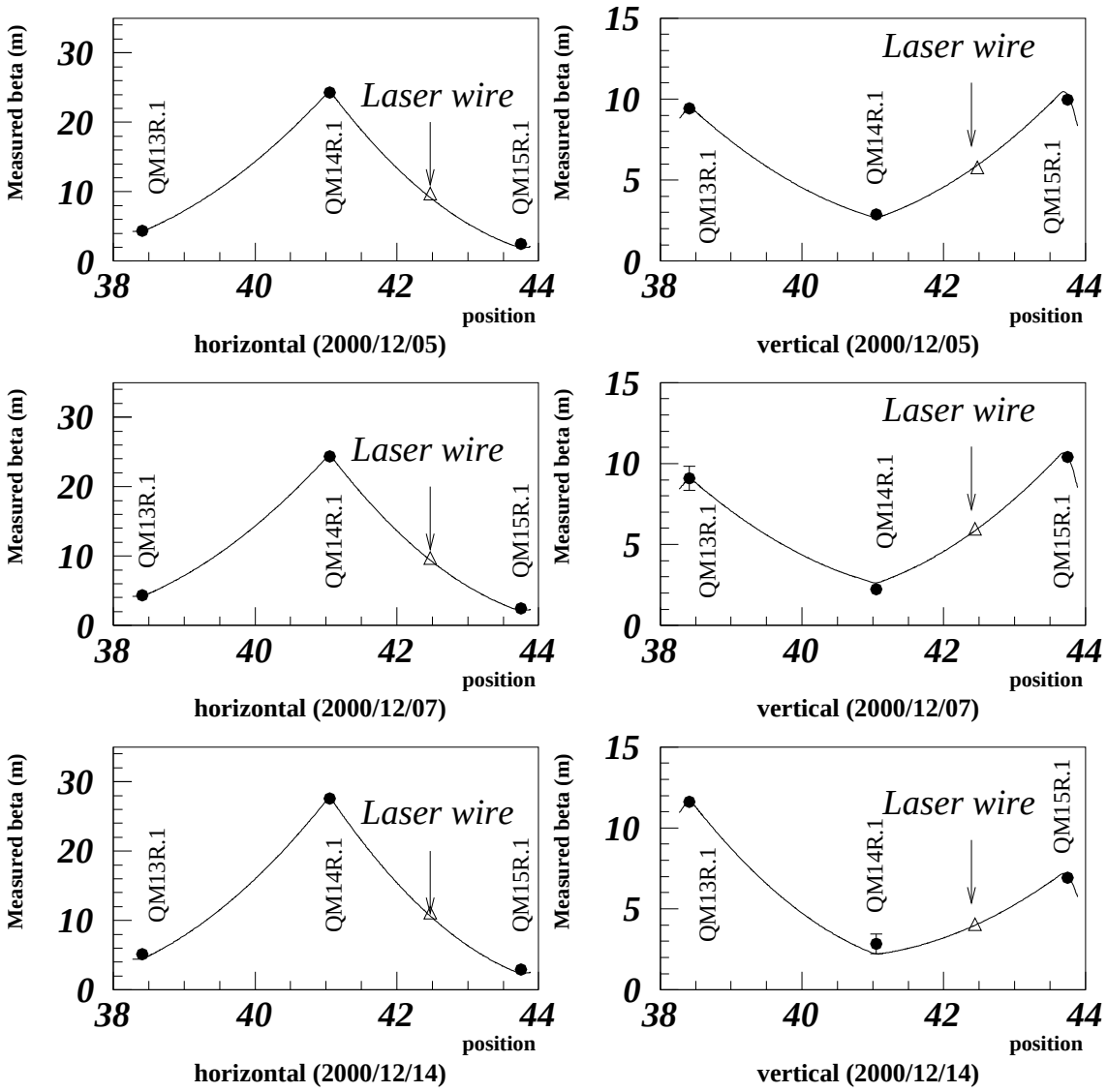

Figure 4.22: β function near the laser wire. Solid line as β function expected from the measurements. Subtitle of each plot represents each direction and measurement data.

Table 4.8: Summary of parameters of the damping ring (Measured value)

parameter of DR		sign	2000/12/05	2000/12/07	2000/12/14
Energy (GeV)		E_0	1.28		
Momentum spread		σ_p/p	$(8.0-5.5)\times 10^{-4}$		
RF voltage (kV)		V_{RF}	286		
RF frequency (MHz)		f_{RF}	714.005		
Momentum compaction		α_M	2.14×10^{-3}		
Tune	x	ν_x	15.18	15.18	15.15
	y	ν_y	8.58	8.58	8.51
β (m)	x	β_x	9.71 ± 0.07	9.73 ± 0.10	11.1 ± 0.08
at laser wire	y	β_y	5.77 ± 0.07	5.65 ± 0.14	3.97 ± 0.17
η (mm)	x	η_x	< 10		
at laser wire	y	η_y	< 2		

4.4 Results of vertical emittance measurement

We combine the measured values for σ_{obs}, w_0 and β to evaluate ε_y, the vertical emittance. The real electron beam size σ_y at the laser wire was evaluated by

$$\sigma_y = \sqrt{\sigma_{obs}^2 - \left(\frac{w_0}{2}\right)^2}. \tag{4.10}$$

The plots on the right in Fig.4.10 show the resultant σ_y. Then we calculated the vertical emittance ε_y by the relation

$$\sigma_y = \sqrt{\beta_y \varepsilon_y + \left(\eta_y \frac{\sigma_p}{p}\right)^2}. \tag{4.11}$$

We neglected the last term $\eta_y\,(\sigma_p/p)$ because it was found to be less than 1.6μm from Table.4.8. Fig.4.23 - Fig.4.25 show vertical emittance vs electron current for three measurements. As anticipated, the 2nd measurement (2000/12/07) shows significantly bigger emittance than the other two. In Fig.4.26, the 1st and 3rd measurement results are superposed. From this plot, we can draw several conclusions:

(1) The 1st and 3rd measurements agree well with each other, especially in the common beam current interval.

(2) As a whole, the results shows the designed goal of 1.2×10^{-11} m·rad is attained by the ATF damping ring. (See below for numerical details.)

(3) There is no obvious and clear dependence on the electron beam current.

To quantify the statements above, we averaged these results in several ways. The averaged emittance in the common current interval [1.0 - 2.2 mA] is $(1.38 \pm 0.14) \times 10^{-11}$ m·rad and $(0.91 \pm 0.23) \times 10^{-11}$ m·rad, respectively, for the 1st and 3rd measurement. They agree well with each other although they could be different because of the different ring optics. The vertical emittance averaged over the entire current region is $(1.21 \pm 0.09) \times 10^{-11}$ m·rad and $(1.00 \pm 0.20) \times 10^{-11}$ m·rad, respectively, for the 1st and 3rd measurement. Strictly speaking, we can't average the two values above since the measured current intervals as well as their ring optics were different. However, encouraged by the agreement in the common current interval, we averaged them to obtain $(1.17 \pm 0.08) \times 10^{-11}$ m·rad. This value should be interpreted as an upper limit of attainable emittance for 0.2 - 3.0 mA. As stated, this shows that the ATF damping ring has realized its target values for the vertical emittance. These results are summarized in Table.4.9, which includes 2nd measurement results for completeness.

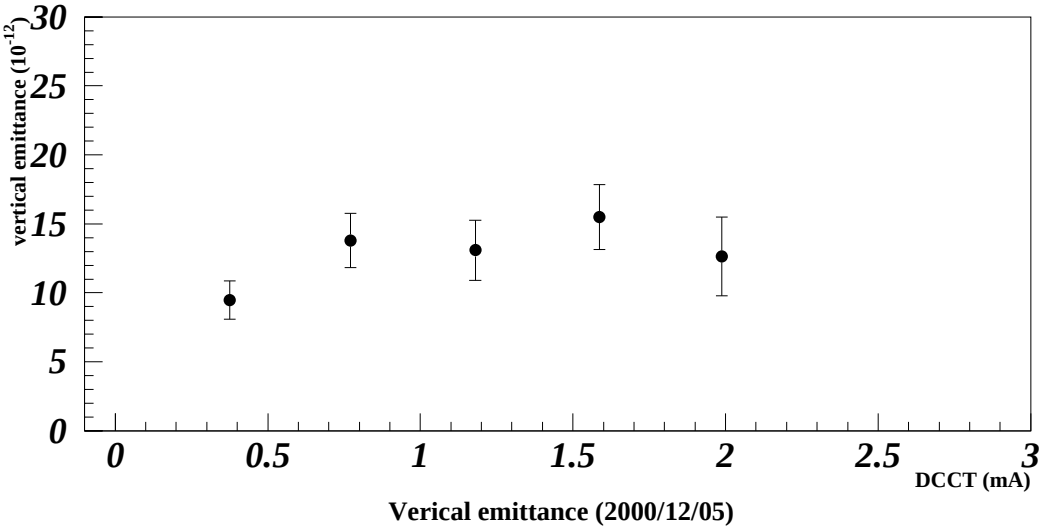

Figure 4.23: Vertical emittance vs the electron current. Taken on (2000/12/05).

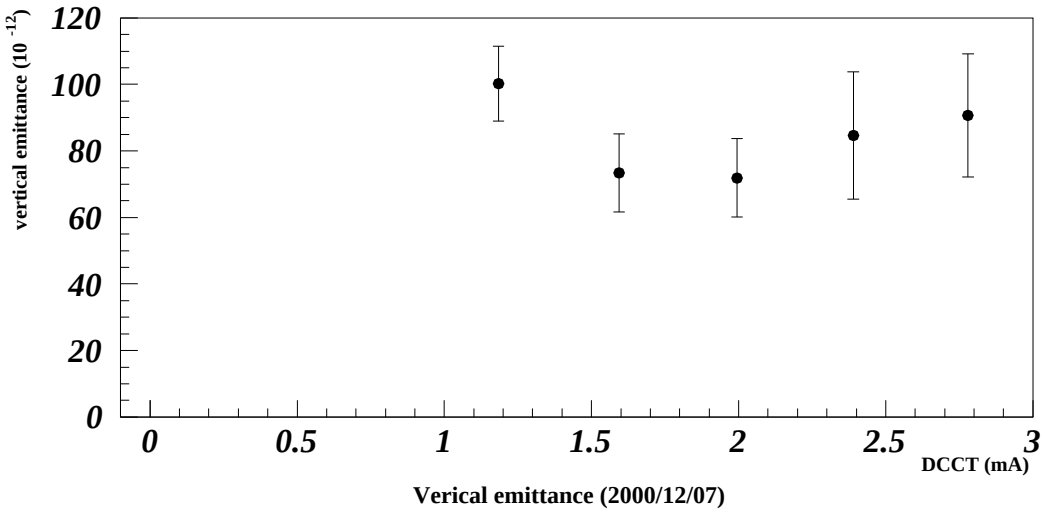

Figure 4.24: Vertical emittance vs the electron current. Taken on (2000/12/07).

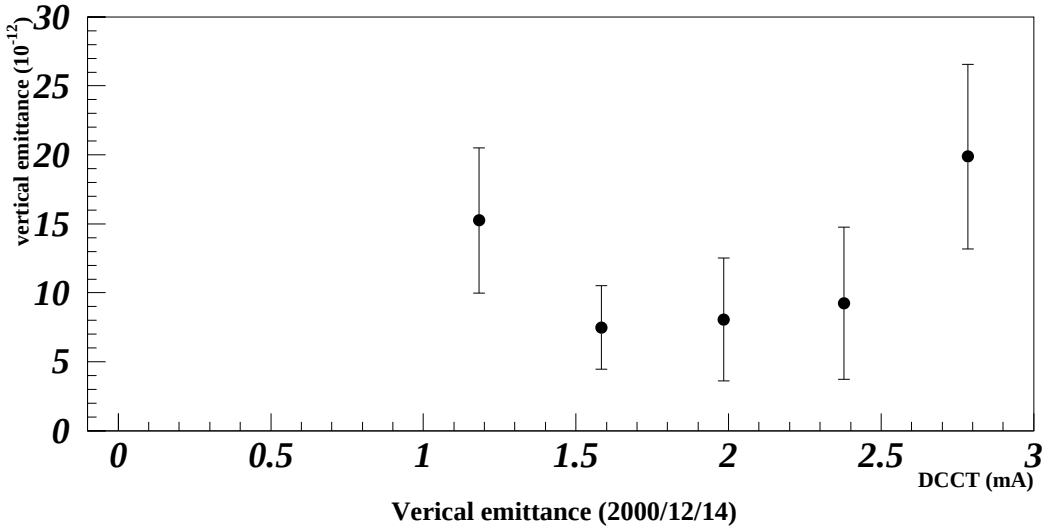

Figure 4.25: Vertical emittance vs the electron current. Taken on (2000/12/14).

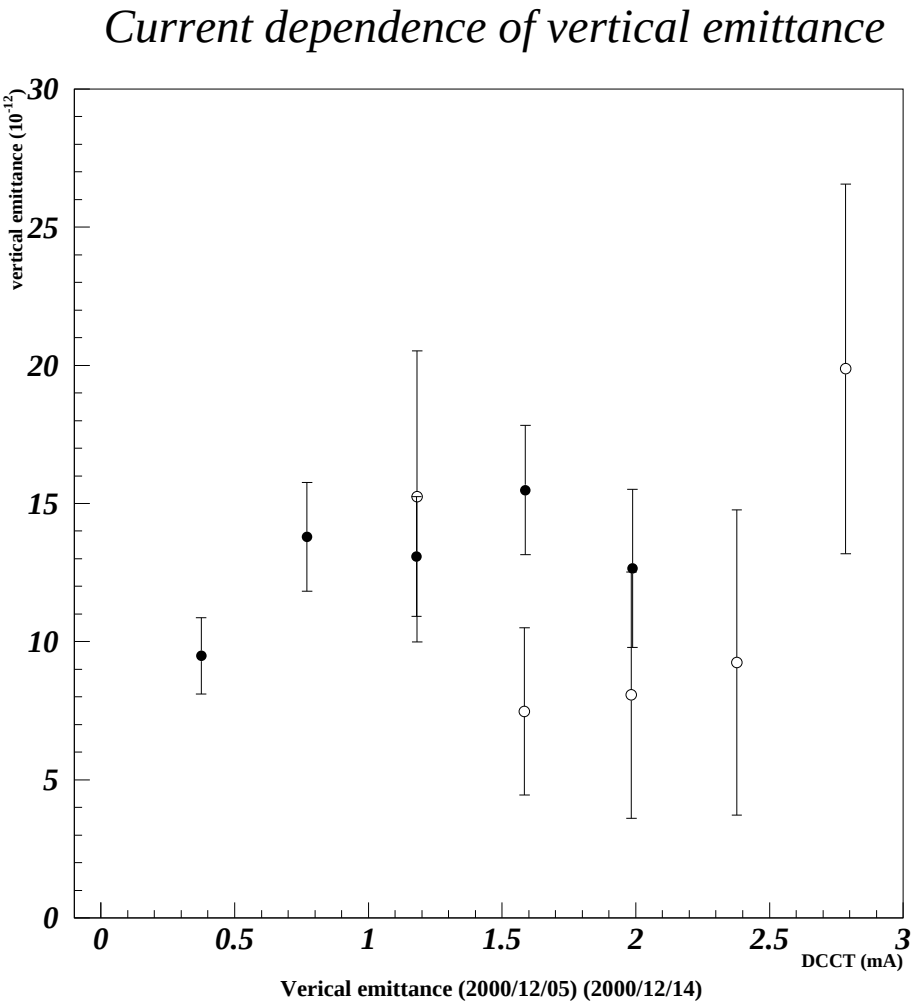

Figure 4.26: Superposition of the two measurements. Solid circles represent the results of data taken on (2000/12/05). Open circles on (2000/12/14).

Table 4.9: Summary of the vertical emittance measurements

date (unit)	ε_y (10^{-11} m $\cdot$ rad)	electron current (mA)	χ^2/ν	
2000/12/05	1.21 $\pm$ 0.09	0.2 - 2.2	6.63/4	(1)
	1.38 $\pm$ 0.14	1.0 - 2.2	0.79/2	
2000/12/07	8.34 $\pm$ 0.60	1.0 - 3.0	4.06/4	
	8.24 $\pm$ 0.67	1.0 - 2.2	3.88/2	
2000/12/14	1.00 $\pm$ 0.20	1.0 - 3.0	4.07/4	(2)
	0.91 $\pm$ 0.23	1.0 - 2.2	1.80/2	
attainable emittance	1.17 $\pm$ 0.08		10.7/8	average (1) & (2)

4.5 Discussion

4.5.1 Estimation of the vertical emittance

In a low emittance ring such as ours, the vertical emittance is mainly determined by coupling with much bigger horizontal emittance and/or residial vertical dispersion. The coupling in turn stems from skewed quadrupole components. In addition, other effects such as intra-beam scattering might be important, but they are ignored in this subsection.

In this subsection, we compare the measured emittance with a model calculation. It calculated all relevant ring parameters with given magnet parameters such as shape, position and current *etc*. In particular, it yielded the β functions, deviation from the ideal orbit (COD), dispersion functions, and emittance. The following steps were proceeded to obtain an estimate of the vertical emittance.

1. Set all the magnets at their measured position.

2. Allow random errors to their position as well as rotation angle. The position errors were considered to be 30μm based on the measured deviation (See Sec.3.4.), the rotation errors were assumed to be 0.3 mrad.

3. Set all the BPMs at their nominal position.

4. Allow random errors of 300μm to their position, and 20mrad to the rotation angle.

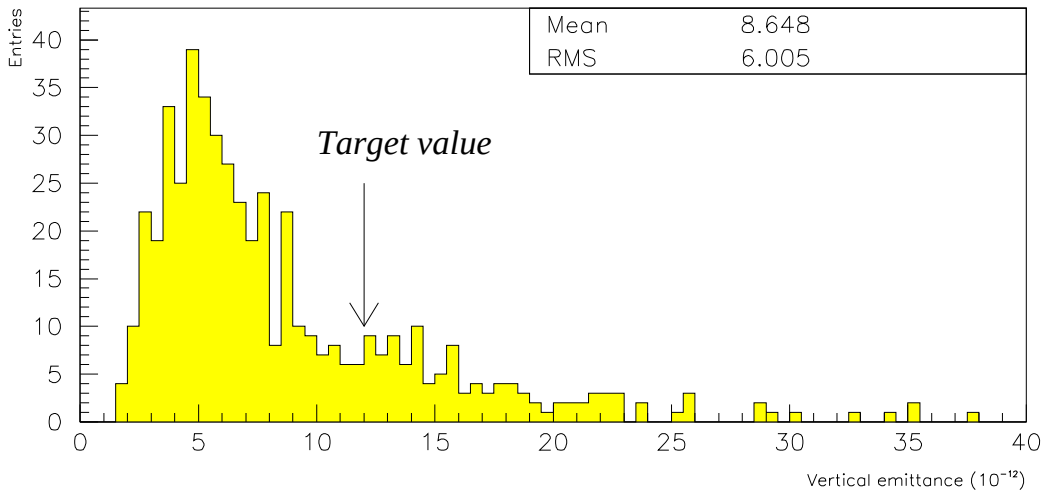

Figure 4.27: Estimate of vertical emittance at laser wire. This histogram is various values resulted from different random seeds for different magnetic settings.

After calculating the actual orbit in the ring and its deviation (COD), the correction procedures, similar to the actual process, were followed in the program.

5. The COD was reduced so that the deviations satisfied $|x| < 2mm$ and $|y| < 1mm$. This was done by adjusting the steering magnets.

6. The dispersion correction was made.

7. The skew correction was carried out by adjusting skew corrector, as was done actually.

8. The vertical emittance, among other quantities, was calculated.

The process 1-8 was repeated 500 times with a different random number seed. It changed the settings in step 2. and 4. Fig.4.27 shows the results of such a calculation. As shown in Fig.4.27, the most of tries resulted in the vertical emittance smaller than the target value of 1.2×10^{-11} m·rad. However, the distribution has a long tail toward a large emittance region. Thus there is a non-negligible chance of failing the target value. We conclude that our measured value is consistent with the expectation.

4.5.2 Effect of intra-beam scattering

Effects due to intra-beam scattering have attracted much attention recently as the number of low emittance rings increases. The ATF damping ring is expected to offer the best place to study such an effect. We have already seen effects due to intra-beam scattering in two places. One is the life time of the stored beam, and the other is the momentum spread.

If the intra-beam scattering is dominant in the ring, the life time can be expressed by the differential equation

$$\frac{dN(t)}{dt} = -\frac{N(t)}{\tau_{life}} - \frac{N^2(t)}{N_0 \tau_{tou}}, \tag{4.12}$$

where N_0 represents the initial number of electron, τ_{life} is the normal life time and τ_{tou} represents the other life time, which determines the effect of the intra-beam scattering [30], [34]. After integrating Eq.(4.12) with time t, the following formula is obtained:

$$N(t) = N_0 \frac{\frac{\tau_{tou}}{\tau_{life}} \exp\left(-\frac{t}{\tau_{life}}\right)}{1 - \exp\left(-\frac{t}{\tau_{life}}\right) + \frac{\tau_{tou}}{\tau_{life}}} \tag{4.13}$$

Fig.4.28 is an example of the measured beam life time shown in a logarithmic scale. The solid line on the left is a fit to the data by a simple exponential (straight line in the plot); it fails very badly. The solid line on the right is a fit to the data by Eq.(4.13) with N_0, τ_{life} and τ_{tou} left as free parameters. It shows that, if the intra-beam scattering effect is taken into account, the fit improves drastically.

The second evidence of the intra-beam scattering is the dependence of momentum spread upon the electron current. Fig.4.29 shows the momentum spread measured at the extraction line with a screen monitor [11]. The current dependence is clearly seen.

The vertical emittance is also expected to grow with the beam current. There are several theoretical studies on the intra-beam scattering [34], [35], [36]. However, magnitude of the effects varies from one model to another. At present, there is no firm prediction yet. As we already mentioned, there is no clear evidence of the emittance growth in the measured values either. Thus, this important phenomenon awaits further investigation from both theoretical and experimental sides.

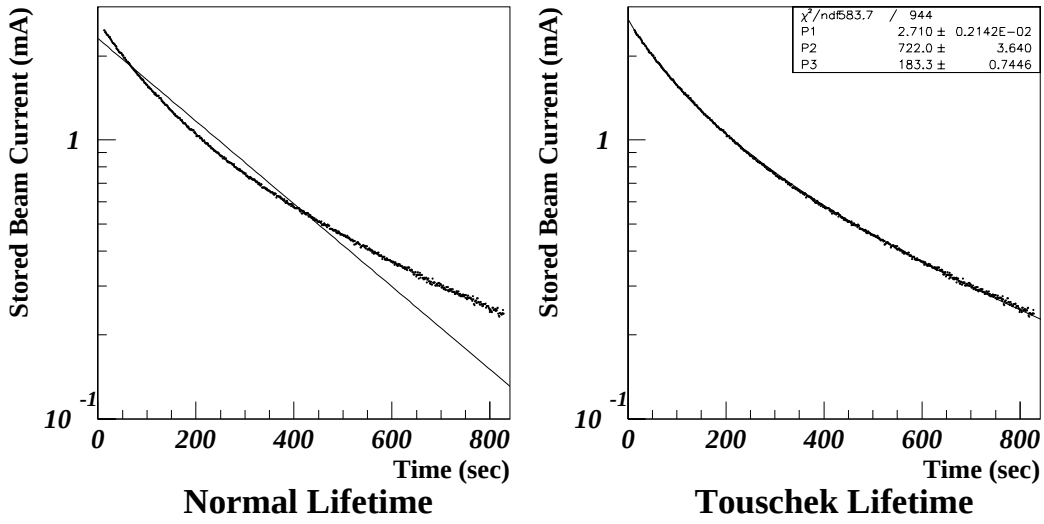

Figure 4.28: Stored electron current vs time in a logarithmic scale. Fits with τ_{life} above (left) and with τ_{life} plus τ_{tou} (right). Fitting parameters of P1, P2, and P3 represents N_0 (mA), τ_{life} and τ_{tou}, respectively.

4.5.3 Future Improvements

We want to discuss future prospects from two different view points. One is improvement in the laser wire system and its related hardware, and the other is study of low emittance beam dynamics. They are related to each other, but for convenience, we begin with the former.

The most important improvement is increase in an effective laser power inside the cavity. A brute-force method is to increase a laser power itself. The other option is to increase cavity's enhancement factor or finesse. We need mirrors with higher reflectivity and less loss. In accordance with the higher finesse, the feedback system (and/or mechanical stability of the cavity) must be refined. Also, the line width of laser should be narrowed, accordingly.

With hindsight, we should be able to improve signal-to-noise ratio with a bigger crystal. As shown in Fig.4.11, the energy resolution became worse due to leakage of a electro-magnetic shower from the present crystal.

We learned that the electron beam position might be drifting during our measurements. We should be able to monitor beam drift with beam position monitors (BPM). However, their accuracy is not good enough; we need to develop or improve a BPM system to reach resolution of $\sim 1\mu$m. Improvements mentioned above are now under way.

Now we want to comment on future beam studies. So far, the ATF damping ring was operated in a single-bunch mode. However, it recently started

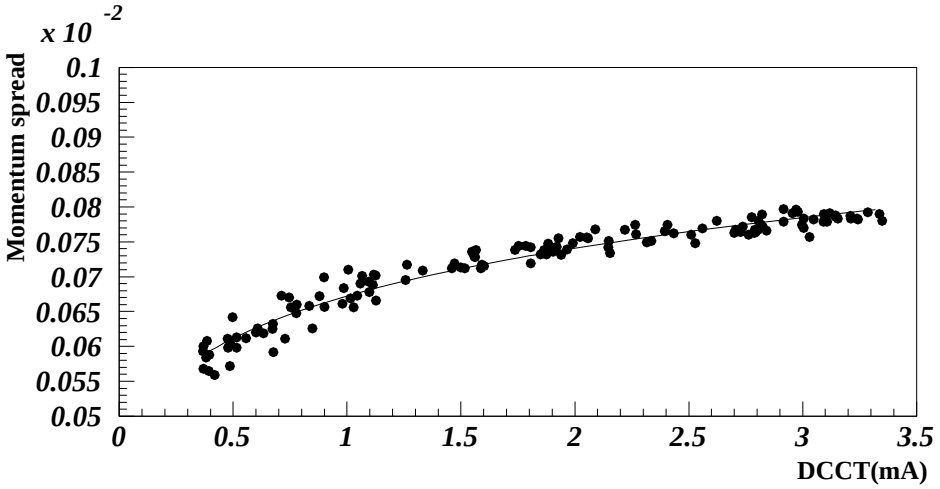

Figure 4.29: Current dependence of the momentum spread

multi-bunch operation. In this mode, 20 bunches, with a spacing of 2.8 ns, are accelerated and stored in the ring. Our main concern is whether or not each bunch can keep such low emittance that was established in the single-bunch mode. It is suggested that instability from a short-range wake field, for example, may cause emittance growth. We note that in JLC it is crucially important to retain low beam emittance even in a multi-bunch mode. Thus it's confirmation or disproof is necessary. Another interest in beam dynamics is the current dependence of the vertical emittance. As mentioned, increase in the effective laser power inside the cavity would improve measurement accuracy. Together with the improvement in BPM, we might be able to see emittance growth due to intra-beam scattering effect.

Chapter 5

Conclusion

In this thesis, we have described vertical emittance measurements of the ATF damping ring with a newly developed beam profile monitor. This monitor, dubbed as *laser wire beam profile monitor*, is based upon Compton scattering off a laser beam target. Energetic photons emitted in the forward direction are detected, and a count rate profile is measured by scanning a laser wire position. An electron beam size is deduced from its count rate shape. In order to achieve a thin and intense laser beam, a Fabry-Perot optical cavity is employed. A beam waist of $14.5 \pm 0.4\mu$m was realized with nearly concentric configuration. By keeping the cavity on resonance, which demanded less than 1nm accuracy in the cavity length, a power enhancement factor of 220 ± 20 was stably archived. A CW laser ($\lambda = 532$nm) with an output power of 100mW was used in the actual measurements. Taking several power losses into account, an effective power inside the cavity exceeded 11W.

This monitor was installed at the straight section of the ATF damping ring. We carried out emittance measurements three times with different ring conditions. The observed signals were unambiguously identified as the Compton photons; the counting rate as well as its energy spectrum agreed well with their expected value and shape. When the ring optics was tuned for low emittance, it was confirmed that a vertical emittance of $\varepsilon_y = (1.17 \pm 0.08) \times 10^{-11}$ rad·m was achieved. This value satisfies the emittance requirement set for JLC ($\varepsilon_y = 1.2 \times 10^{-11}$ rad·m); the confirmation is a major step toward realization of high energy linear colliders.

It is expected that vertical emittance of the ATF damping ring may grow due to an intra-beam scattering as the beam current increases effect. However, no clear current dependence was observed in the measurements. We note that, however, there is no convincing prediction on the magnitude of emittance growth. Thus it is much too early to draw any conclusion from

the present measurements alone. Thus improvement of accuracy is definitely needed. Statistical errors can be reduced by increasing an effective laser power inside the optical cavity with a more powerful laser and/or mirrors with higher reflectivity. Systematic errors due to a beam position jitter and/or drift may be reduced by monitoring its beam position with a precision BPM. Improvement works on the laser wire as well as the BPM are now under way.

So far, ATF was operated in a single-bunch mode; recently it started a multi-bunch operation. This technique is essential in achieving a required luminosity in JLC. It is planned to measure vertical emittance of a multi-bunch beam with this monitor.

In conclusion, we could successfully develop a new type of a beam profile monitor for a low emittance electron beam, and confirmed the vertical emittance of the ATF damping ring to satisfy the target value set for JLC. The advent of the laser wire monitor will certainly open up a new era in studying beam dynamics of low emittance electron rings envisioned by JLC, FEL and 4th generation SOR.

Appendix A

Beam Dynamics

We describe the beam dynamics [37].

A.1 Betatron Oscillation

A.1.1 Equation of motion

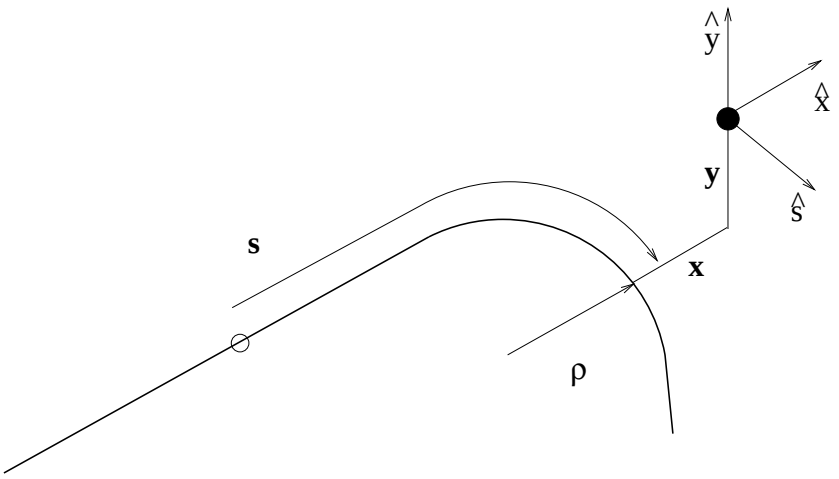

Figure A.1: Frenet Serret coordinate system

Hamiltonian The Hamiltonian $H_t(x, p_x, y, p_y, s, p_s, t)$ for a particle of charge e, mass m in an electro magnetic fields is expressed by electro magnetic potential ϕ_{em} and $\vec{A}_{em}$ [38] as

$$H_t(x, p_x, y, p_y, s, p_s; t) = e\phi_{em} + T \tag{A.1}$$

,where

$$T = c\left[m^2c^2 + (p_x - eA_x)^2 + (p_y - eA_y)^2 + \left(\frac{p_s - eA_s}{1+\frac{x}{\rho_0}}\right)^2\right]^{1/2} = \gamma mc^2 \quad \text{(A.2)}$$

is the kinematic energy. The coordinates (x,y,s) are shown in Fig.A.1. The canonical vector potentials are

$$\begin{aligned} A_x &= \hat{x}\cdot\vec{A}_{em} \\ A_y &= \hat{y}\cdot\vec{A}_{em} \\ A_s &= \left(1+\frac{x}{\rho_0}\right)\hat{s}\cdot\vec{A}_{em}. \end{aligned} \quad \text{(A.3)}$$

With s as the independent variable, the Hamiltonian can be written by

$$H_s(x, p_x, y, p_y, t, -E; s) = -eA_s - \left(1+\frac{x}{\rho_0}\right)P_s, \quad \text{(A.4)}$$

where $-E$ is the momentum conjugate to the coordinate t and

$$P_s = \left[\left(\frac{E - e\phi_{em}}{c}\right)^2 - (p_x - eA_x)^2 - (p_y - eA_y)^2 - m^2c^2\right]^{1/2} \quad \text{(A.5)}$$

is the kinematic momentum in the s direction. We only consider the transverse motion, the Hamiltonian H_{sT} for transverse motion can be expressed by

$$\begin{aligned} H_{sT}(x, p_x, y, p_y; s) &= -\frac{eA_s}{p} - \left(1+\frac{x}{\rho_0}\right)\left[1 - p_x^2 - p_y^2\right]^{1/2} \\ &= -\left(1-\frac{\Delta p}{p}\right)\frac{eA_s}{p_0} - \left(1+\frac{x}{\rho_0}\right)\left[1 - p_x^2 - p_y^2\right]^{1/2} \end{aligned} \quad \text{(A.6)}$$

where ρ_0 is the radius of the design particle, p is the kinematic momentum ,the momentum offset $\frac{\Delta p}{p}$ is defined by $\frac{\Delta p}{p} = (p - p_0)/p$ The canonical potential for magnetic lattice elements, expanded to 2nd order in x and y are: [39]

$$\frac{e}{p}A_{s,Drift} = 0 \tag{A.7}$$

$$\frac{e}{p}A_{s,Bend} = \frac{1}{2}\left(1+\frac{x}{\rho_0}\right)^2 \tag{A.8}$$

$$\frac{e}{p}A_{s,Quad} = \frac{K}{2}(x^2-y^2) \tag{A.9}$$

K is called k-value and denotes the strength of the focusing effect with electron beam ($K = \frac{1}{B\rho_0}\frac{\partial B_y}{\partial x}$). The expansion of Eq.(A.6) to 2rd order in x, y, p_x and p_y is [40]

$$H_{s,Drift} = \frac{1}{2}p_x^2 + \frac{1}{2}p_y^2 \tag{A.10}$$

$$H_{s,Bend} = \frac{1}{2}p_x^2 + \frac{1}{2}p_y^2 + \frac{xp_x^2}{2\rho_0} + \frac{xp_y^2}{2\rho_0} - \frac{\Delta p}{p}\left[\frac{x}{\rho_0}+\frac{x^2}{2\rho_0^2}\right] \tag{A.11}$$

$$H_{s,Quad} = \frac{1}{2}p_x^2 + \frac{1}{2}p_y^2 + (1-\frac{\Delta p}{p})\frac{K(x^2-y^2)}{2}, \tag{A.12}$$

where each suffixes *Drift*, *Bend* and *Quad* show the 'Drift space', 'Separate bending magnet', and 'Quadrupole magnet', respectively. Then each magnetic field

The equation of motion Hamiltonian equation of these canonical conjugate x, p_x and y, p_y drawn by

$$\frac{dz}{ds} = \frac{\partial H_{s,T}}{\partial p_z} \ , \ \frac{dp_z}{ds} = -\frac{\partial H_{s,T}}{\partial z} \ , \ (z = x, y) \tag{A.13}$$

First we assume the ideal case ($\frac{\Delta p}{p} = 0$). From Eq.(A.10) - (A.12), we obtain the below equations :

$$\frac{d^2z}{ds} + K_z(s)z = 0 \ , \ (z = x, y) \tag{A.14}$$

$$K_x = K + \frac{1}{\rho_0} \ , \ K_y = -K \tag{A.15}$$

By solving the above equations, following solutions are obtained;

$$
\begin{aligned}
z(s) &= A\sqrt{\beta(s)}\cos(\psi(s)+\psi_0) \\
z'(s) &= -\frac{A}{\sqrt{\beta(s)}}\left[\alpha(s)\cos(\psi(s)+\psi_0)+\sin(\psi(s)+\psi_0)\right], \qquad \text{(A.16)}
\end{aligned}
$$

where A and ψ_0 are constants of integration, $\alpha(s) \equiv -\beta'(s)/2$. The β-function satisfies the following relations

$$
\begin{aligned}
2\beta\beta'' - \beta'^2 + 4\beta^2 K_z &= 4 \qquad \text{(A.17)} \\
d\psi/ds &= 1/\beta \qquad \text{(A.18)} \\
& \qquad \text{(A.19)}
\end{aligned}
$$

with phase advances $\psi(s)$.

A.1.2 Twiss parameter and Courant Snyder Invariant

Phase space The motions of the electron beam are described in Eq.(A.16). To explain the beam motion more simply, but in general, the motions are described on the phase space. This is because we can obtain the invariant value on the phase space described as:

$$
A^2 = \frac{1}{\beta}\left[z^2 + (\alpha z + \beta z')^2\right] = \gamma z^2 + 2\alpha z z' + \beta z'^2 \equiv W_z, \qquad \text{(A.20)}
$$

where $\gamma \equiv \frac{1+\alpha^2}{\beta}$. We call W_z as *Courant-Snyder Invariant.* These values determine the motion of beam in the phase space. (α, β, γ) are called as *twiss parameter*, and determine the beam orbit of the phase space. Fig.A.2 shows the twiss parameter of the phase space.

Transfer Matrix From Eq.(A.16),we can write down the relation between s_1 and s_2 on the beam line with the matrix formula.

$$
\begin{pmatrix} z(s_2) \\ z'(s_2) \end{pmatrix} = M(s_2, s_1) \begin{pmatrix} z(s_1) \\ z'(s_1) \end{pmatrix} \qquad \text{(A.21)}
$$

$$
M_{11} = \sqrt{\frac{\beta_2}{\beta_1}}(\cos\Delta\psi + \alpha_1 \sin\Delta\psi) \qquad \text{(A.22)}
$$

$$
M_{12} = \sqrt{\beta_1\beta_2}\sin\Delta\psi \qquad \text{(A.23)}
$$

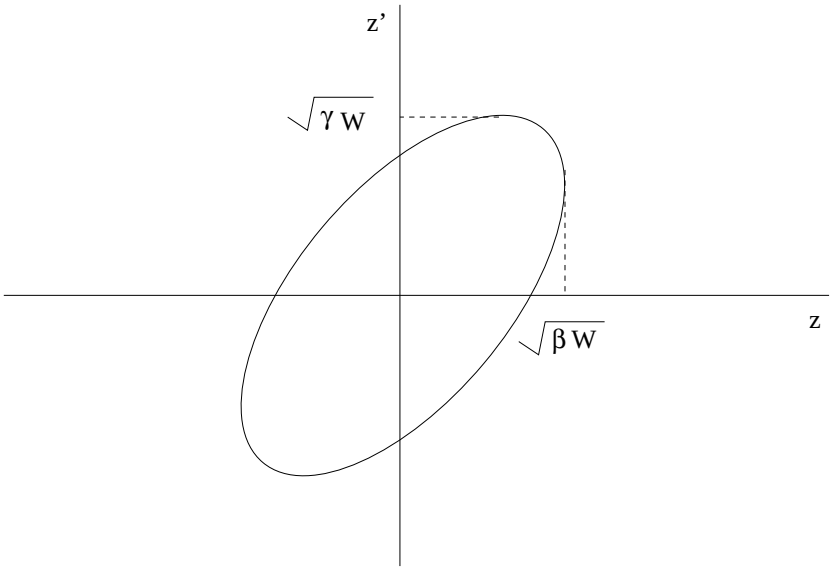

Figure A.2: Schematic diagram of the motion of one particle in the phase space (z,z')

$$M_{21} = \frac{\alpha_1 - \alpha_2}{\sqrt{\beta_1\beta_2}} \cos\Delta\psi - \frac{1+\alpha_1\alpha_2}{\sqrt{\beta_1\beta_2}} \sin\Delta\psi \tag{A.24}$$

$$M_{22} = \sqrt{\frac{\beta_1}{\beta_2}}(\cos\Delta\psi - \alpha_2 \sin\Delta\psi), \tag{A.25}$$

where suffixes show the function of the s_1 and s_2, and $\Delta\psi = \psi_2 - \psi_1$. We call this matrix $M(s_2, s_1)$ as transfer matrix. Furthermore from Eq.(A.22) - Eq.(A.25), we have relations corresponding to the twiss parameters on s_1 and s_2.

$$\begin{pmatrix} \alpha(s_2) & \beta(s_2) \\ -\gamma(s_2) & -\alpha(s_2) \end{pmatrix} = M(s_2,s_1) \begin{pmatrix} \alpha(s_1) & \beta(s_1) \\ -\gamma(s_1) & -\alpha(s_1) \end{pmatrix} M^{-1}(s_2,s_1), \tag{A.26}$$

where $\alpha(s_{1,2})$, $\beta(s_{1,2})$ and $\gamma(s_{1,2})$ are twiss parameters on the point of $s_{1,2}$. These transfer matrixs are determined by the component of magnet as described on the Table.?? and are solved bxy using Eq.(A.19).

$$K_z > 0 \qquad M(s_2,s_1) = \begin{pmatrix} \cos\sqrt{K_z}L_s & \frac{1}{\sqrt{K_z}}\sin\sqrt{K_z}L_s \\ -\sqrt{K_z}\sin\sqrt{K_z}L_s & \cos\sqrt{K_z}L_s \end{pmatrix} \tag{A.27}$$

$$K_z = 0 \qquad M(s_2,s_1) = \begin{pmatrix} 1 & L_s \\ 0 & 1 \end{pmatrix} \tag{A.28}$$

$$K_z < 0 \qquad M(s_2, s_1) = \begin{pmatrix} \cosh\sqrt{-K_z}L_s & \frac{1}{\sqrt{-K_z}}\sinh\sqrt{-K_z}L_s \\ \sqrt{-K_z}\sinh\sqrt{-K_z}L_s & \cosh\sqrt{-K_z}L_s \end{pmatrix} \quad \text{(A.29)}$$

with $L_s = s_2 - s_1$, the path length of the beam line. If we know a set of the twiss parameter of the one particle and the Transfer Matrix though the beam line, we can trace the particle orbit.

In addition, if the periodic condition of the k-value satisfys the condition $K_z(s) = K_z(s + C)$, the *beta* function also has a periodic condition $\beta(s) = \beta(s + C)$.

$$M(s, s + C) = \begin{pmatrix} \cos\psi + \alpha\sin\psi & \beta\sin\psi \\ -\gamma\sin\psi & \cos\psi - \alpha\sin\psi \end{pmatrix} \quad \text{(A.30)}$$

We emphasize that we can obtain twiss parameter everywhere in the ring by utilizing the Transfer Matrix in Eq.A.30

A.1.3 Dispersion function

On the previous section, we consider the design motion. However in general the particle doesn't go through the ideal path. The particle has the momentum offset $\frac{\Delta p}{p}$. The equations of motion with $\frac{\Delta p}{p} \neq 0$ are obtained from Eq.(A.10) - Eq.(A.13)

$$\frac{d^2x}{ds^2} + K_x x = \left(K_x x + \frac{1}{\rho_0}\right)\frac{\Delta p}{p} \quad \text{(A.31)}$$

$$\frac{d^2y}{ds^2} + K_y y = K_y y\frac{\Delta p}{p} \quad \text{(A.32)}$$

We separate the x, y with the betatron motion described as above and the off momentum part.

$$x(s) = x_\beta(s) + \eta_x(s)\frac{\Delta p}{p} \quad \text{(A.33)}$$

$$y(s) = y_\beta(s) + \eta_y(s)\frac{\Delta p}{p}, \quad \text{(A.34)}$$

where suffix β denotes the solution of the betatron motion on the ideal path, and $\eta_{x,y}$ is called as dispersion function. The equation of motion can be written by using the 1st order of $\frac{\Delta p}{p}$:

$$\left(\frac{d^2x_\beta}{ds^2} + K_x x_\beta\right) + \frac{\Delta p}{p}\left(\frac{d^2\eta_x}{ds^2} + K_x\eta_x - \frac{1}{\rho_0}\right) = 0 \qquad \text{(A.35)}$$

$$\left(\frac{d^2y_\beta}{ds^2} + K_y y_\beta\right) + \frac{\Delta p}{p}\left(\frac{d^2\eta_y}{ds^2} + K_y\eta_y\right) = 0, \qquad \text{(A.36)}$$

where x, y and η_y behave with the same way as the betatron motion and can be described by the transfer matrix. If η_y and η_y' is equal to 0 on the initial point, η_y must be 0 at all point. On the other hand, η_x changes according to the motion due to the term of $1/\rho_0$. First we consider $\eta_x(0) = \eta_x'(0) = 0$, and we replace the function $D_x(s) = \eta(s)$ and $D_x'(s) = \eta'(s)$ at the solution of $s = 0$. $D_x(s)$ and $D_x'(s)$ can be expressed as

$$K_x > 0 \qquad D_x(s) = \frac{1 - \cos\sqrt{K_x}s}{\rho_0 K_x} \ , \ D_x'(s) = \frac{\sin\sqrt{K_x}s}{\rho_0\sqrt{K_x}} \qquad \text{(A.37)}$$

$$K_x = 0 \qquad D_x(s) = \frac{s^2}{2\rho_0} \ , \ D_x'(s) = \frac{s}{\rho_0} \qquad \text{(A.38)}$$

$$K_x < 0 \qquad D_x(s) = \frac{1 - \cosh\sqrt{-K_x}s}{\rho_0 K_x} \ , \ D_x'(s) = \frac{\sinh\sqrt{-K_x}s}{\rho_0\sqrt{-K_x}} \qquad \text{(A.39)}$$

Accordingly, the dispersion function $\eta_x(s)$ can be described by using transfer matrix and the function $D_x(s)$ and $D_x'(s)$ from s_1 to s_2,

$$\begin{pmatrix} \eta_x(s_2) \\ \eta_x'(s_2) \end{pmatrix} = M(s_2, s_1)\begin{pmatrix} \eta_x(s_1) \\ \eta_x'(s_1) \end{pmatrix} + \begin{pmatrix} D_x(s_1) \\ D_x'(s_1) \end{pmatrix} \qquad \text{(A.40)}$$

A.1.4 Emittance

On the previous section, we assume the motion of only one particle. However , in practice, many particles are accelerated and circulated in the ring. In this section, we consider the motion of the many particles. Assumed the many particle are distributed with gauss function on a phase space as shown in Fig.A.3. This gaussian distribution function $F(z', z)$ can be discirbed by the same twiss parameters by

$$F(z', z)dz'dz = \frac{1}{2\pi\sigma_W^2}\exp\left[-\frac{\gamma_z z^2 + 2\alpha_z zz' + \beta_z z'^2}{2\sigma_W^2}\right]dz'dz \qquad \text{(A.41)}$$

From Eq.(A.41), we obtain the following relations.

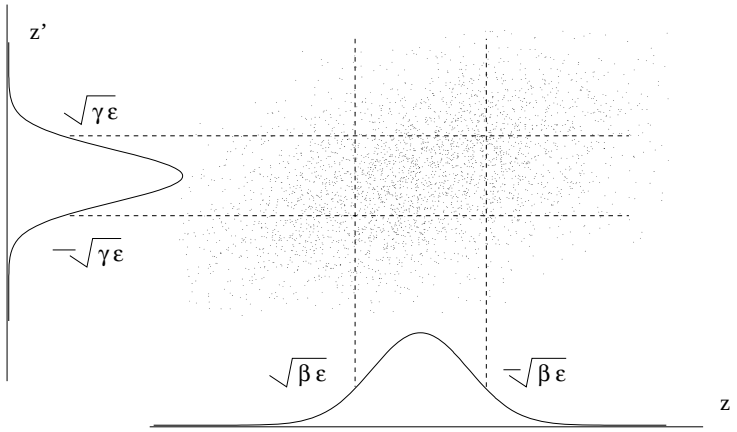

Figure A.3: The distribution of many particles on phase space

$$\sigma_z = \sqrt{< z^2 > - < z >^2} = \sqrt{\beta_z \varepsilon_z} \quad \text{(A.42)}$$

$$\sigma_{z'} = \sqrt{< z'^2 > - < z' >^2} = \sqrt{\gamma_z \varepsilon_z} \quad \text{(A.43)}$$

$$< z z' > = -\alpha_z \varepsilon_z \quad \text{(A.44)}$$

$$\varepsilon_z \equiv \sigma_W^2 =< W_z > /2, \quad \text{(A.45)}$$

where ε_z is called as *emittance* [1]. and determine the spread of the distribution of the particles on a phase space. Then, the motion of the beam is expressed by twiss parameter and the emittance. In general, the emittance is also invariant like the Courant-Snyder invariant in the transport line.

A.2 Equilibrium beam emittances

In the damping ring, the emittance is not invariant and reduced by the damping process. In this section, first, we describe the synchrotron oscillation. Especially the two important processes are explained to reduce the emittance. One is the radiation damping and another is the quantum excitation. After the explanations, we describe the equilibrium condition of the emittance.

[1] Concerning the emittance, the definition of proton and ion beam is different from that of the electron beam

A.2.1 Synchrotron Oscillation

We go back to the discussion of the motion of only one particle system to explain the longitudinal motion.

Radiation integral Beam parameters in a ring are modified by the emission process of synchrotron radiation. These effects are governed by a radiation integrals [40], [41].

$$I_1 \equiv \oint ds \frac{\eta_x(s)}{\rho_0(s)} \tag{A.46}$$

$$I_2 \equiv \oint ds \frac{1}{\rho_0^2(s)} \tag{A.47}$$

$$I_3 \equiv \oint ds \frac{1}{|\rho_0(s)|^3} \tag{A.48}$$

$$I_4 \equiv \oint ds \frac{\eta_x(s)}{\rho_0^3(s)} \left(1 + \rho_0^2(s) K_x(s)\right) \tag{A.49}$$

$$I_5 \equiv \oint ds \frac{H_x(s)}{|\rho_0(s)|^3}, \tag{A.50}$$

where $H_x(s) \equiv (\gamma_x \eta_x^2 + 2\alpha_x \eta_x \eta_x' + \beta_x \eta_x'^2)$. We can ignore the vertical integral, because $\rho_0 \to \infty$ on the vertical plane.

Equation of longitudinal motion When the electron beam circulates in the storage ring, the synchrotron radiation is emitted, this energy loss per second P can be written by

$$P = \frac{2}{3} \frac{e^2 r_e}{(m_e c^2)^3} \frac{E^4}{\rho^2} = \frac{2}{3} \frac{e^2 r_e c^3}{(m_e c^2)^3} E^2 B_y^2. \tag{A.51}$$

For the sake of the loss caused by the synchrotron radiation, the momentum of particle is shifted by $\frac{\Delta p}{p}$. This shift affects the transverse shift Δx, magnetic field B_y and the difference of a path length through the field of the bending magnet dl as follows.

$$\Delta x = \eta_x \frac{\Delta p}{p} \tag{A.52}$$

$$E = E_0 (1 + \frac{\Delta p}{p}) \tag{A.53}$$

$$B_y \simeq B_{y,0} + \frac{\partial B_y}{\partial x}\eta_x \frac{\Delta p}{p} = \frac{E_0}{ec}\left(\frac{1}{\rho_0} + \eta_x K \frac{\Delta p}{p}\right) \tag{A.54}$$

$$dl = \frac{\rho_0 + \Delta x}{\rho_0} ds = \left(1 + \frac{\eta_x}{\rho_0}\frac{\Delta p}{p}\right) \tag{A.55}$$

From Eq.(A.52) - Eq.(A.55), the radiation loss per turn $U(\frac{\Delta p}{p})$ can be written by

$$\begin{aligned} U(\frac{\Delta p}{p}) &= \oint^C \frac{dl}{c} P = \frac{2}{3}\frac{e^2 r_e c^2 E_0^2}{(mc^2)^3}\frac{E_0^2}{e^2c^2}\oint^C ds \left(1 + \frac{\eta_x}{\rho_0}\frac{\Delta p}{p}\right)(1 + \frac{\Delta p}{p})^2 \left(\frac{1}{\rho_0} + \eta_x k \frac{\Delta p}{p}\right)^2 \\ &\simeq \frac{2}{3} r_e \gamma^3 E_0 \left[I_2 + (2I_2 + I_4)\frac{\Delta p}{p}\right] \equiv U_0 + U_1 \frac{\Delta p}{p} \end{aligned} \tag{A.56}$$

To compensate the energy loss, we supply the power from a RF cavity. V_{RF} is the voltage of the acceleration, f_{RF} is the RF frequency, and τ is defined by the shift of the time from synchronous phase ϕ_0

$$\phi_0 = \sin^{-1}\left(\frac{U_0}{eV_{RF}}\right) \tag{A.57}$$

When a particle goes through the RF cavity at once, it can obtain the energy $E_{RF}(\tau)$

$$\begin{aligned} E_{RF}(\tau) &= eV_{RF}\sin(\phi_0 - 2\pi f_{RF}\tau) \\ &\simeq U_0 - \tau 2\pi f_{RF} e V_{RF}\sqrt{1 - \left(\frac{U_0}{eV_{RF}}\right)^2} \equiv U_0 - E_1\tau \end{aligned} \tag{A.58}$$

The shift of energy per one turn ΔE is obtained by

$$\Delta E = E_{RF}(\tau) - U(\frac{\Delta p}{p}) = -E_1\tau - U_1\frac{\Delta p}{p} \tag{A.59}$$

Energy shift slower than the time of one turn. We can describe

$$\frac{d\frac{\Delta p}{p}}{dt} \simeq \frac{1}{E_0}\frac{c\Delta E}{C} = -\frac{c}{CE_0}\left(E_1\tau + U_1\frac{\Delta p}{p}\right) \tag{A.60}$$

Similarly we consider τ.

$$\frac{d\tau}{dt} = \frac{\Delta C}{C} = \frac{1}{C}\left[\oint dl - \oint ds\right] = \frac{I_1}{C}\frac{\Delta p}{p} \equiv \alpha_M \frac{\Delta p}{p}, \tag{A.61}$$

where α_M is the momentum compaction factor. From Eq.(A.60) and Eq.(A.61), we can obtain the following equation.

$$\frac{d^2\zeta}{dt^2} + \frac{2}{\tau_s}\frac{d\zeta}{dt} - (2\pi f_s)^2\zeta = 0 \ , \ (\zeta = \frac{\Delta p}{p}, \tau) \tag{A.62}$$

$$f_s^2 = \frac{eV_{RF}\alpha_M c f_{RF}}{2\pi C E_0}\sqrt{1 - \left(\frac{U_0}{eV_{RF}}\right)} \tag{A.63}$$

$$\frac{1}{\tau_s} = \frac{cU_1}{2CE_0} = \frac{r_e c\gamma_e^3}{3C}(2I_2 + I_4), \tag{A.64}$$

where $\gamma_e = E_0/m_e$. From these relations, we solve the longitudinal motion, with the momentum spread $\frac{\Delta p}{p}$, which makes the damping oscillation from Eq.(A.62). This oscillation is called as synchrotron oscillation.

A.2.2 Radiation damping

On the previous section, we discuss the radiation loss on the longitudinal motion. On the other hand, since there are the damping effects on the transverse motion, we go back to discuss the betatron motion including the radiation loss.

Transverse beam motions are determined by the Courant Synder invariant. For example, the average of z^2, zz', z'^2,(z = x,y) can be written by

$$< z^2 > \ = \ \frac{W_z\beta_z}{2} \tag{A.65}$$

$$< zz' > \ = \ -\frac{W_z\alpha_z}{2} \tag{A.66}$$

$$< z'^2 > \ = \ \frac{W_z\gamma_z}{2} \tag{A.67}$$

We can explain about the damping mechanism of the transverse motion with the shift of Courant Synder Invariant.

Radiation damping from RF cavity First we explain the dependence of the damping from the RF cavity. If the particle moves through the RF cavity, the longitudinal momentum is enhanced with Δp by the RF acceleration. ($c\Delta p = E_{RF}(\tau)$) On the other hand, the transverse momentum is not changed. The shift of transverse motion Δz and $\Delta z'$ are expressed, when the particle moves through the RF cavity.

$$\Delta z = 0 \tag{A.68}$$

$$\Delta z' = \left(\frac{p_z}{p+\Delta p} - \frac{p_z}{p}\right) \simeq -z'\frac{E_{RF}(\tau)}{cp} \tag{A.69}$$

From this shift, we can deduce the shift of Courant Snyder invariant.

$$\begin{aligned}\frac{dW_{z,RF}}{dt} &= 2 < \gamma_z z\Delta z + \alpha_z(z\Delta z' + \Delta z z') + \beta_z z'\Delta z' > \frac{c}{C} \\ &\simeq -2(\alpha_z < zz' > + \beta_z < z'^2 >)\frac{U_0}{pC} \\ &= \frac{(-\alpha_z^2 + \beta_z\gamma_z)U_0}{pC}W_z = -\frac{2r_e c\gamma^3}{3C}I_2 W_z \end{aligned} \tag{A.70}$$

Radiation damping from synchrotron radiation Synchrotron radiation mainly occurs when the particle is bent by the bending magnet. When we discuss about the effect of radiation damping from the synchrotron radiation, we only consider the transverse motion on the horizontal plane.

When the particle emits the synchrotron radiation and momentum is shifted by Δp_{sync}, we have a little shift of the transverse motion Δx_{sync} and $\Delta x'_{sync}$.

$$\Delta x_{sync} = -\eta_x\frac{\Delta p_{sync}}{p} \tag{A.71}$$

$$\Delta x'_{sync} = -\eta'_x\frac{\Delta p_{sync}}{p} \tag{A.72}$$

The Courant Snyder invariant is also changed by the synchrotron radiation.

$$\begin{aligned}\Delta W_{x,sync} &= -2\left[\gamma_x x\Delta x_{sync} + \alpha_x(x\Delta x'_{sync} + x'\Delta x_{sync}) + \beta_x x'\Delta x'_{sync}\right] \\ &= -2\left[(\gamma_x\eta_x + \alpha_x\eta'_x)x + (\alpha_x\eta_x + \beta_x\eta'_x)x'\right]\frac{\Delta p_{sync}}{p} \end{aligned} \tag{A.73}$$

Next we consider the momentum shift Δp_{sync}, which is the function of the position of x. If the particle moves through the path length Δs in the bending field, $\Delta p_{sync}(x)$ is a little shifted with

$$\begin{aligned}\Delta p_{sync}(x) &= \frac{P}{c}\Delta l = \left(P_0 + \frac{\partial P}{\partial B_y}\frac{\partial B_y}{\partial x}x\right)\left(1+\frac{x}{\rho_0}\right)\frac{\Delta s}{c} \\ &= -\frac{P_0}{c}\left[1+\left(\frac{1}{\rho_0}+2\rho_0 K_x\right)x + 2K_x x^2\right]\Delta s \qquad \text{(A.74)}\end{aligned}$$

We rewrite the Courant Snyder invariant as

$$\begin{aligned}\Delta W_{x,sync} &= \frac{2P_0}{cp}\left[1+\left(\frac{1}{\rho_0}+2\rho_0 K_x\right)x + 2K_x x^2\right] \\ &\times \left[(\gamma_x\eta_x+\alpha_x\eta_x')x + (\alpha_x\eta_x+\beta_x\eta_x')x'\right]\Delta s \\ &= \Delta s\frac{2P_0}{cp}\left(\frac{1}{\rho_0}+2\rho_0 K_x\right) \\ &\times \left[(\gamma_x\eta_x+\alpha_x\eta_x')x^2 + (\alpha_x\eta_x+\beta_x\eta_x')xx'\right] \qquad \text{(A.75)}\end{aligned}$$

From Eq.(A.75), the ratio of the Courant Snyder invariant shift can be denoted by

$$\frac{dW_{x,sync}}{dt} = \frac{4r_e\gamma_e^3}{3}\oint ds\frac{1}{\rho_0^2}\left(\frac{1}{\rho_0}+2\rho_0 K_x\right)\frac{\eta_x W_x c}{2C} = \frac{2r_e c\gamma_e^3}{3C}I_4 W_x \qquad \text{(A.76)}$$

Damping ratio From Eq.(A.70) and Eq.(A.76),

$$\begin{aligned}\frac{dW_x}{dt} &= \frac{dW_{x,RF}}{dt} + \frac{dW_{x,sync}}{dt} = -\frac{2r_e c\gamma_e^3}{3C}(I_2 - I_4)W_x \qquad \text{(A.77)} \\ \frac{dW_y}{dt} &= \frac{dW_{x,RF}}{dt} = -\frac{2r_e c\gamma_e^3}{3C}I_2 W_x \qquad \text{(A.78)}\end{aligned}$$

And the betatron amplitude is described by $z = \sqrt{\beta_z W_z}$. The damping ratio of the transverse motion can be written by

$$\frac{dz}{dt} = \sqrt{\beta_z}\frac{d\sqrt{W_z}}{dt} = \frac{1}{2}\sqrt{\frac{\beta_z}{W_z}}\frac{dW_z}{dt} = -\frac{1}{\tau_z}z \qquad \text{(A.79)}$$

From Eq.(A.64) and Eq.(A.79), we can summarize the damping ratio on three dimensions by using the parameter $J_i (i = x, y, s)$.

$$\frac{1}{\tau_i} = -\frac{r_e c \gamma_e^3}{3C} I_2 J_i \tag{A.80}$$

$$J_x = 1 - \frac{I_4}{I_2} \ , \ J_y = 1 \ , \ J_s = 2 + \frac{I_4}{I_2} \tag{A.81}$$

We obtain the relation of the three parameter $J_x + J_y + J_s = 4$. This relation is called as Robinson's sum. Even if there are vertical bending magnets on the transverse motion, the Robinson's sum is realized.

A.2.3 Quantum excitation

The excitation of transverse motion is occurred by the quantum emission process, and this effect is called as quantum excitation. To consider the statistical process, we argue the transverse motion of many particles and the statistical distribution of the beam.

The time of damping process is longer than one revolution time of the damping ring. If we ignore the damping term on the Eq.(A.62), longitudinal motion can be written as the simple oscillation. Moreover, we assume that each particle emits the photon by the synchrotron oscillation independently and the momenta of the photons have the distribution with $n(p_{rad})$. Then the amplitude of the momentum can be shifted with $\Delta \left(\sigma_{p_{ex}}\right)^2$ when the particle moves around the ring on one turn.

$$\Delta \left(\frac{\sigma_{p_{ex}}}{p}\right)^2 = \frac{1}{2} \sum_i \left(\frac{\Delta p_{rad}}{p}\right)_i^2 = \frac{1}{2p^2 c} \oint ds \int_0^\infty dp_{rad} n(p_{rad}) p_{rad}^2 \tag{A.82}$$

The distribution can be integrated from [37]

$$\int_0^\infty dp_{rad} n(p_{rad}) p_{rad}^2 = \frac{55}{24\sqrt{3}} r_e \hbar m_e c^2 \frac{\gamma_e^7}{|\rho_0|^3}. \tag{A.83}$$

We obtain the enhancement of momentum spread by one turn.

$$\Delta \left(\frac{\sigma_{p_{ex}}}{p}\right)^2 = \frac{55 r_e \hbar \gamma_e^5}{48\sqrt{3} m_e c} \oint ds \frac{1}{|\rho_0|^3} = \frac{2 r_e}{3} C_q \gamma_e^5 I_3 \tag{A.84}$$

$$, C_q \equiv \frac{55}{32\sqrt{3}} \frac{\hbar}{m_e c} = 3.84 \times 10^{-13} (m) \tag{A.85}$$

This result means that $(\sigma_p/p)^2$ is enhanced every one turn. Similarly, we can express the discussion of the transverse motion, if we consider the shift of the Courant Snyder invariant by quantum excitation.

When the photon with transverse momentum $\Delta p_z (z = x, y)$ is emitted by the synchrotron radiation, the shift of Courant Snyder invariant $\Delta W_{z,rad}$ is expressed by

$$\Delta W_{z,rad} = \beta_z \left(\frac{\Delta p_z}{p} \right)^2 = \beta_z \left(\frac{\Delta p \theta_z}{p} \right)^2 . \tag{A.86}$$

We consider that the angular distribution of the emitted photon has the gaussian distribution $\theta_z^2 = 1/\gamma_e^2$, which is independent with the momentum of the photon. Then we can obtain the enhancement of Courant Snyder invariant $\Delta(\sigma_W^2)_{ex,rad}$:

$$\begin{aligned} \Delta(\sigma_W^2)_{ex,rad} &= \frac{1}{2p^2 c\gamma_e^2} \oint ds \beta_z(s) \int_0^\infty dp_{rad} n(p_{rad}) p_{rad}^2 \\ &= \frac{55 r_e \hbar \gamma_e^3}{48\sqrt{3} m_e c} \oint ds \frac{\beta_z(s)}{|\rho_0|^3} = \frac{2r_e}{3} C_q \gamma_e^3 I_{\beta,z} \qquad \text{(A.87)} \\ I_{\beta,z} &\equiv \oint ds \frac{\beta_z(s)}{|\rho_0|^3} \qquad \text{(A.88)} \end{aligned}$$

Similarly we can obtain the shift of Courant Snyder invariant $\Delta W_{x,disp}$ where the dispersion function exists. From Eq.(A.71) and Eq.(A.72),

$$\Delta W_{x,disp} = \left(\gamma_x \eta_x^2 + 2\alpha_x \eta_x \eta_x' + \beta_x \eta_x'^2 \right) \left(\frac{\Delta p}{p} \right)^2 = H_x(s) \left(\frac{\Delta p}{p} \right)^2 . \tag{A.89}$$

Then we can also obtain the enhancement of Courant Snyder invariant $\Delta(\sigma_W^2)_{ex,disp}$:

$$\Delta(\sigma_W^2)_{ex,disp} = \frac{1}{2p^2 c} \oint ds H_x(s) \int_0^\infty dp_{rad} n(p_{rad}) p_{rad}^2 = \frac{2r_e}{3} C_q \gamma_e^5 I_5 \tag{A.90}$$

These two results are summarized by applying the enhancements of horizontal and vertical emittance of one turn, $\Delta\varepsilon_{x,ex}$ and $\Delta\varepsilon_{y,ex}$.

$$\begin{aligned} \Delta\varepsilon_{x,ex} &= \Delta \left(\sigma_{W_x}^2 \right)_{ex} = \frac{2r_e}{3} C_q \gamma_e^3 (\gamma_e^2 I_5 + I_{\beta,x}) \qquad \text{(A.91)} \\ \Delta\varepsilon_{y,ex} &= \Delta \left(\sigma_{W_y}^2 \right)_{ex} = \frac{2r_e}{3} C_q \gamma_e^3 I_{\beta,y} \qquad \text{(A.92)} \end{aligned}$$

On the horizontal plane, these two affect the enhancement of the emittance. However on high energy accelerator, first term is dominant in Eq.(A.91).

A.2.4 Equilibrium condition

As is explained on the previous section, the emittance variation and the momentum spread are determined by the radiation damping and quantum excitation.

From Eq.(A.80),(A.81), we can deduce the damping ratio of the momentum spread and the emittance variation every turn by averaging the momentum shift and Courant-Synder invariant;

$$\Delta\left(\frac{\sigma_{p,damp}}{p}\right)^2 = -\frac{2C}{c\tau_s}\left(\frac{\sigma_p}{p}\right)^2 \tag{A.93}$$

$$\Delta\varepsilon_{x,damp} = -\frac{2C}{c\tau_x}\varepsilon_x \tag{A.94}$$

$$\Delta\varepsilon_{y,damp} = -\frac{2C}{c\tau_y}\varepsilon_y \tag{A.95}$$

However after damping process, momentum spread and emittances, finally, settle down by the equilibrium condition. From Eq.(A.93),(A.94),(A.95) and Eq.(A.84),(A.91),(A.91), we can calculate the equilibrium emittance and momentum spread.

$$\left(\frac{\sigma_p}{p}\right)^2 = \frac{c\tau_s}{2C}\Delta\left(\frac{\sigma_{p,ex}}{p}\right)^2 = \frac{C_q\gamma^2 I_3}{I_2 J_s} \tag{A.96}$$

$$\varepsilon_x = \frac{c\tau_x}{2C}\Delta\varepsilon_{x,ex} = \frac{C_q}{I_2 J_x}(\gamma_e^2 I_5 + I_{\beta,x}) \tag{A.97}$$

$$\varepsilon_y = \frac{c\tau_y}{2C}\Delta\varepsilon_{y,ex} = \frac{C_q}{I_2 J_y} I_{\beta,x} \tag{A.98}$$

A.3 Vertical emittance source in ATF

We explained that the equilibrium emittance and momentum spread were determined by the radiation damping and quantum excitation process in the damping ring. We emphasize that these parameters are inherent and determined by the radiation integral of a damping ring.

As shown in Eq.(A.97), horizontal emittance is determined by the first term $\gamma_e^2 I_5$, because in the damping ring $\gamma_e \simeq 2500$ and $I_5 \simeq I_{\beta,x}$. Similarly the vertical emittance should be determined by the lattice parameter of the damping ring. $\varepsilon_y/\varepsilon_x \simeq 1/\gamma_e^2 \simeq 10^{-7}$ should be satisfied. However, in practice, this ideal small vertical emittance cannot be realized. Moreover, the vertical emittance is primarily determined by the vertical dispersion and betatron coupling arising from alignment errors [42]. In realistic case, a small magnetic field for the vertical motion arises from a slight misalignment of the magnets. The betatron oscillation is occurred from the center of a closed orbit which is different from an ideal path. This orbit is called as *Closed Orbit Distortion* (COD).

A.3.1 Effect of the vertical dispersion

If there are the vertical dispersion, we can replace the equilibrium emittance as

$$\varepsilon_x = \frac{C_q}{I_2 J_x}\left(\gamma_e^2 I_{5,x} + I_{\beta,x}\right) \tag{A.99}$$

$$\varepsilon_y = \frac{C_q}{I_2 J_y}\left(\gamma_e^2 I_{5,y} + I_{\beta,y}\right) \tag{A.100}$$

$$I_{5,z} \equiv \oint ds \frac{\gamma_z \eta_z^2 + 2\alpha_z \eta_z \eta_z' + \beta_z \eta'^2}{|\rho_{0,z}|^3} \quad (z = x, y) \tag{A.101}$$

The first term in Eq.(A.100) is the main contribution.

For example, when we have the 20 μm random alignment errors on the setting of the magnets in the 1.28 GeV ATF damping ring, we calculate the vertical emittance and result is $1 - 5 \times 10^{-11}$ m $\cdot$ rad. This value is 1-5 times higher than the design value [10].

A.3.2 Effect of the betatron coupling

The growth of vertical emittance also arises from the betatron coupling between the horizontal and vertical direction. In general, when a skew quadrupole magnetic field K_{skew} exists, the equation of motion in Eq.(A.15) can be written by

$$\frac{d^2x}{ds^2} + K_x x = -K_{skew} y \tag{A.102}$$

$$\frac{d^2y}{ds^2} + K_y y = -K_{skew} x \tag{A.103}$$

Table A.1: The tolerances of the alignment errors .

	Δx (μm)	Δy (μm)	$\Delta\theta$ (mrad)
Quad	90	60	0.2
Sext	90	60	0.2
Bend	90	60	0.2

This equation indicates that transverse motion of horizontal and vertical plane are not considered independently. From the skew effect, the equilibrium emittance finally settles down to the following values [42]:

$$\varepsilon_x = \frac{C_q}{I_2}\left[\frac{\gamma_e^2 I_{5,x}+I_{\beta,x}}{J_x(1+\kappa)}+\frac{\kappa(\gamma_e^2 I_{5,x}+I_{\beta,x})}{J_y(1+\kappa)}\right] \quad \text{(A.104)}$$

$$\varepsilon_y = \frac{C_q}{I_2}\left[\frac{\kappa(\gamma_e^2 I_{5,x}+I_{\beta,x})}{J_x(1+\kappa)}+\frac{\gamma_e^2 I_{5,x}+I_{\beta,x}}{J_y(1+\kappa)}\right] \quad \text{(A.105)}$$

$$\kappa = \frac{1}{16C}\frac{J_x}{J_y}\oint ds\left[\sum_{\pm}\frac{|\kappa_\pm|^2}{\sin^2\pi\nu_\pm}+\frac{2Re\{\kappa_+^*\kappa_-\}}{\sin\pi\nu_+\sin\pi\nu_-}\right] \quad \text{(A.106)}$$

$$\kappa_\pm(s) = \int_s^{s+C} ds' K(s')\sqrt{\beta_x(s')\beta_y(s')}e^{i[\psi_\pm(s)-\psi_\pm(s')+\pi\nu_\pm]} \quad \text{(A.107)}$$

,where $\nu_{x,y}$ is called as tune and means the repetition number of the betatron oscillation by one turn. $\nu_\pm$ and $\psi_\pm$ means $\nu_\pm = \nu_x \pm \nu_y$ and $\psi_\pm = \psi_x \pm \psi_y$. κ is called as *betatron coupling*.

We note that skew components arise from the rotation of the quadrupole magnet and the misalignment of the sextuple magnet.

A.3.3 Requirements for the vertical emittance in ATF

We summarize the requirement of the setting of the magnet of the ATF damping ring to realize $\gamma_e\varepsilon_y = 3.0\times10^{-8}, (\varepsilon_y = 1.2\times10^{-11})$ on 1.28 GeV electron beam in Table.A.1 [10] . [2].

[2]The setting errors of the magnet field also affect the vertical emittance and need the severe requirement At present we have corrected within 0.05 % error, which satisfied the requirement 0.1% of the vertical emittance

Appendix B

Background Study

B.1 The measurements of the background

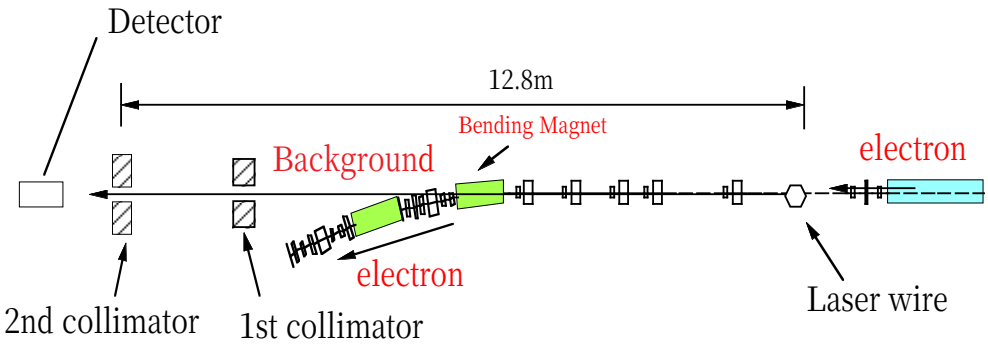

Figure B.1: Apparatus of the background measurement

Fig.B.1 shows the apparatus of the background measurement. Detector is the same that used for the emittance measurement. In order to measure the spatial distribution and rough direction of the background, two collimators are set downstream of the north straight section of the damping ring as shown in Fig.B.1. The 1st collimator has two holes of 10mmϕ and 5mmϕ. The 2nd collimator has 5mmϕ hole. The two collimators were made of 100mm thick lead block. Each collimator independently moves on horizontal direction.

B.1.1 Spatial distribution of the background

We measured the spatial distribution of the background by setting the threshold level above 15MeV. The data transformed to NIM level and counted by a scaler. We measured the spatial distribution of the background by moving two lead collimators independently. After the alignments of two collimator as shown in Fig.3.27, we assign the zero on the initial positions of two collimators. Fig.B.2 shows the results of the measurement of the spatial distribution of background. The horizontal axis shows the position of the 2nd collimator and the vertical axis shows the count rate of the background above 15MeV gamma energy at 2mA electron current.

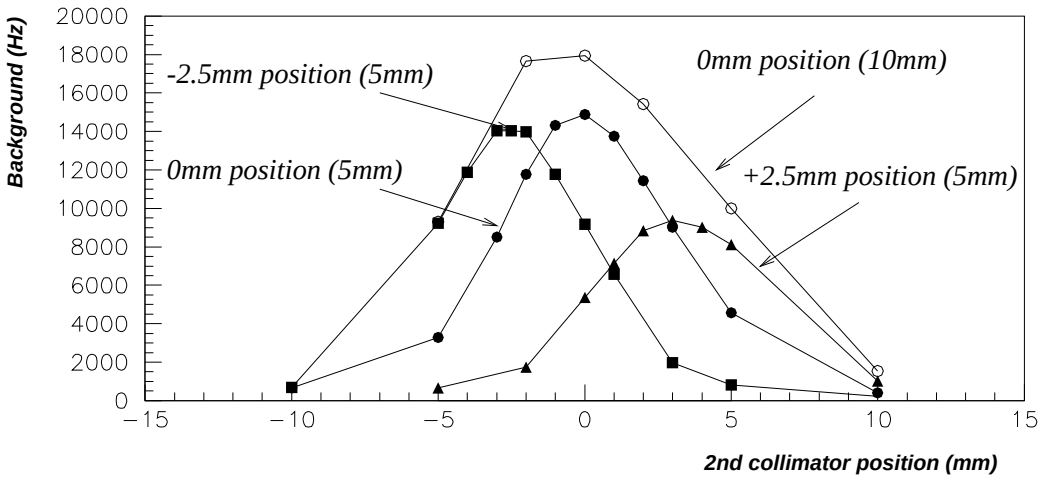

Figure B.2: Spatial distribution of background

The solid circles, solid triangles and solid squares shows the plot when the 1st 5mm collimator was set on the 0mm position, +2.5mm position, -2.5mm position respectively. And the open circles shows the plot when the 1st 10mm collimator was set on the 0mm position. As shown in Fig.B.2, the background profile is asymmetric distribution on setting the position of 1st collimator. Furthermore, the rate of the background of the 10mmϕ collimator is larger than that of the 5mmϕ.

B.1.2 The dependence of the vacuum pressure

In the ATF damping ring, many ion pumps are set to reduce the vacuum pressure. The mount of the absorption of these ion pumps determined by the achievable vacuum pressure in the damping ring. The measurement of the vacuum pressure is done by the cold cathode gauge (CCG). 34 CCG are set

Table B.1: The pressure dependence of the background (2000/06/16).

	Count rate of background at 1.5mA	Average pressure at north straight section
Ion pump off	18.9 kHz	9.4×10^{-6} Pa
Ion pump on	8.90 kHz	3.9×10^{-6} Pa

in a damping ring and 8 CCG are utilized to monitor the vacuum pressure on a north straight section.

In order to measure the pressure dependence to the background, we measure the background by tuning on and off the ion pumps at north straight section. Table.B.1 shows the measurement results by changing the vacuum pressure condition.

We found that the higher the vacuum pressure is, the larger the count rate is. From these results, the vacuum pressure is dominant on the background condition on these measurements.

B.1.3 Current dependence of the background

We also measure the current dependence of the background on the same condition in Fig.B.1. Fig.B.10 shows the current dependence of the background. The horizontal axis shows the electron current and the vertical axis shows the count rate of the gamma-ray above 15MeV threshold.

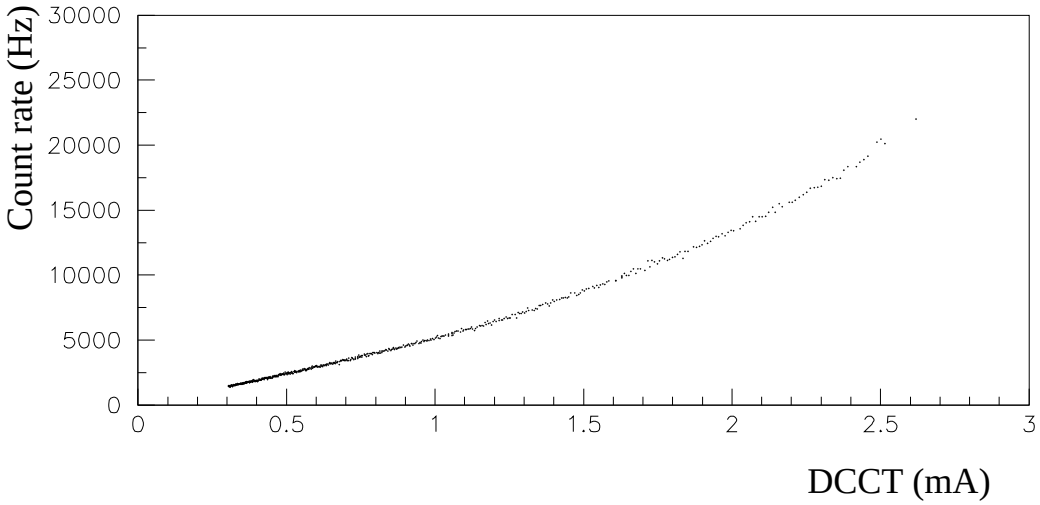

Figure B.3: Current dependence of the background

The count rate of the background is not proportional to the DCCT (mA) but a polynomial function.

B.1.4 Energy spectrum of the background

We also measure the energy spectrum. Fig.B.4 shows the result of the obtained energy spectrum by setting the threshold level above 5 MeV. The data was taken by ADC. It is found that energy spectrum is continuous, and the higher the energy of background is, the smaller the count of background is.

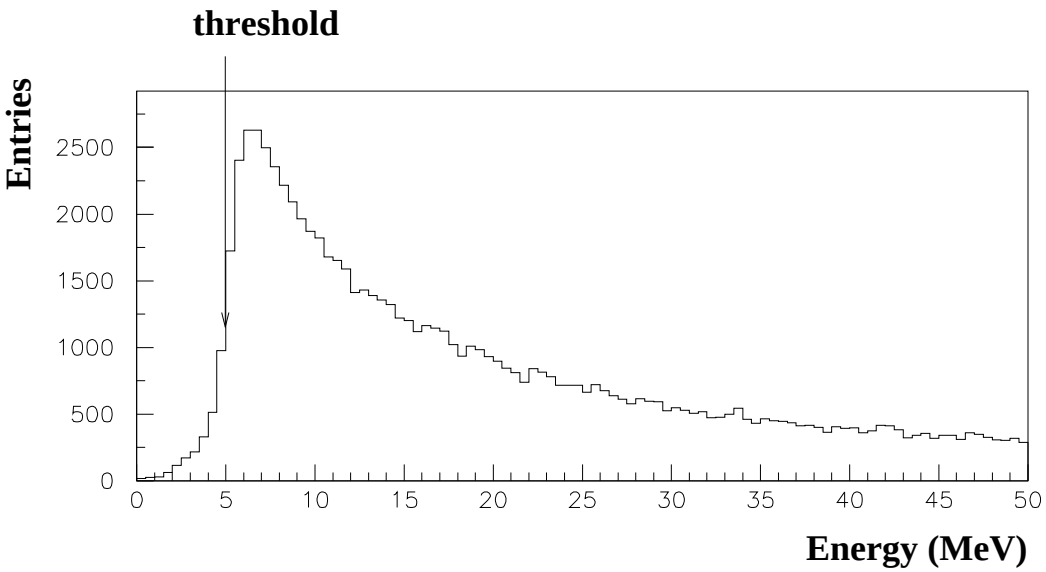

Figure B.4: Energy spectrum of the background

B.2 An estimation of the background source

From these measurements, the characteristics of the background are summarized on the following condition.

1. This spatial distribution is described by an asymmetric function.
2. The background strongly depends on the vacuum pressure.
3. The count rate of the background is not proportional to the DCCT (mA) but a polynomial function of DCCT.

4. The energy spectrum is continuous, and the higher the energy of background is, the smaller the count of background is.

To explain these characteristics, we consider some assumptions of the production process of the background.

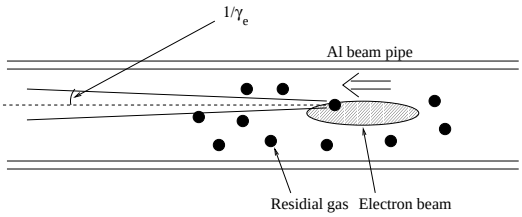

Figure B.5: The background production precess by the residial gas (process 1)

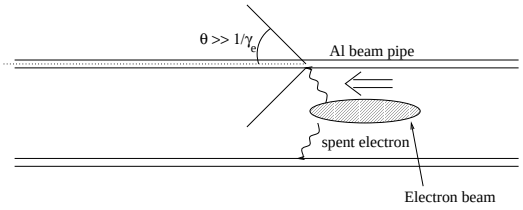

Figure B.6: The background production process by the spent electron (process 2)

First, from the dependence of the vacuum pressure, we can consider the bremsstrahlung caused by the interaction of the electron beam with residial gas as shown in Fig.B.5 (process 1) [34]. The γ-ray produced by the bremsstrahlung has the angler distribution of $1/\gamma_e$. We note that the vacuum pressure is proportional to the electron current. Fig.B.8 shows the plot of the current dependence of the vacuum pressure. The horizontal axis is the electron current (mA) and the vertical axis shows the average pressure through the damping ring. We found that the vacuum pressure is linear to the electron current. If we consider the current dependent pressure, we also make an explanation of the non-linearity current dependence of the background.

Another, we can consider the bremsstrahlung caused by the interaction of the spent electrons with the Al beam pipe as shown in FigB.6 (process 2). The lifetime of the electron beam is described as Eq.(4.12). Especially, the Touschek lifetime is much dominant in the ATF damping ring. Then the nonlinearity of the current dependence of the background is considered by intra-beam scattering dominant spent electons. When the spent electron hits the Al beam pipe, the γ-ray is emitted. This angler distribution θ is much larger than $1/\gamma_e$.

We calculate the spatial distribution of the background on each process by using EGS4 with including the geometry as shown in Fig.B.1. Left figure shows the profile based on the process 1 and right figure shows the profile based on the process 2. The plots of the solid circle, solid triangles ,solid squares and the open circles on FigB.1 corresponds to the conditions of the same mark in Fig.B.2.

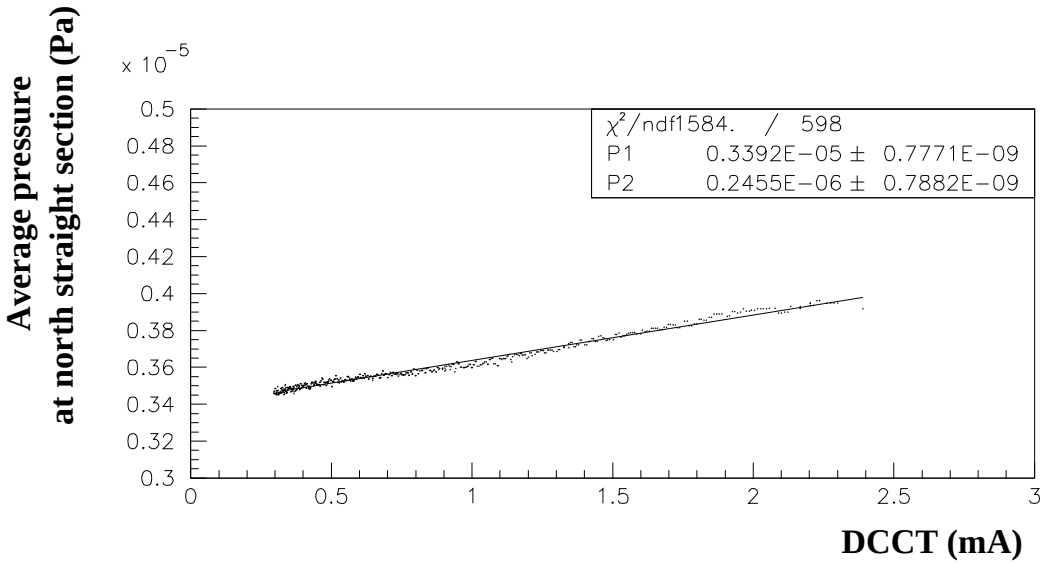

Figure B.7: Current dependence of the vacuum pressure

On the calculation, we apply the 5mmϕ and 10mmϕ 1st collimator , the 5mmϕ 2nd collimator and the 24mmϕ Al beam pipe. To estimate the asymmetric profile of the spatial distribution, we assume the beam orbit has an intentional 1mm offset for the ideal orbit .

By assuming the process 1, we obtain the asymmetric profile like Fig.B.2. On the other hand, we cannot obtain the asymmetric profile by the process 2. The background of 5mm ϕ 1st collimator ,however, is smaller than that of 10mm ϕ 1st collimator. We cannot obtain this reduction on the process 1.

From Table.B.1 and these simulation, the background is assumed to be mainly caused by the vacuum pressure.

B.3 Measurement of the background after improvement

We found that the background mainly depends on the vacuum pressure. In order to improve the signal-to-noise ratio on the detection of the scattered photon from laser wire, then during the summer shutdown, we improve the vacuum pressure at the north straight section. After the improvement, we remeasure the same spatial distribution of the background in Sec.B.1.1. Fig.B.9 shows the spatial distribution of the background of the ion pump on and off condition. The electron current is 1.5mA ,and lower threshold of the scattered gamma energy is above 15MeV. Top figure shows the ion pump

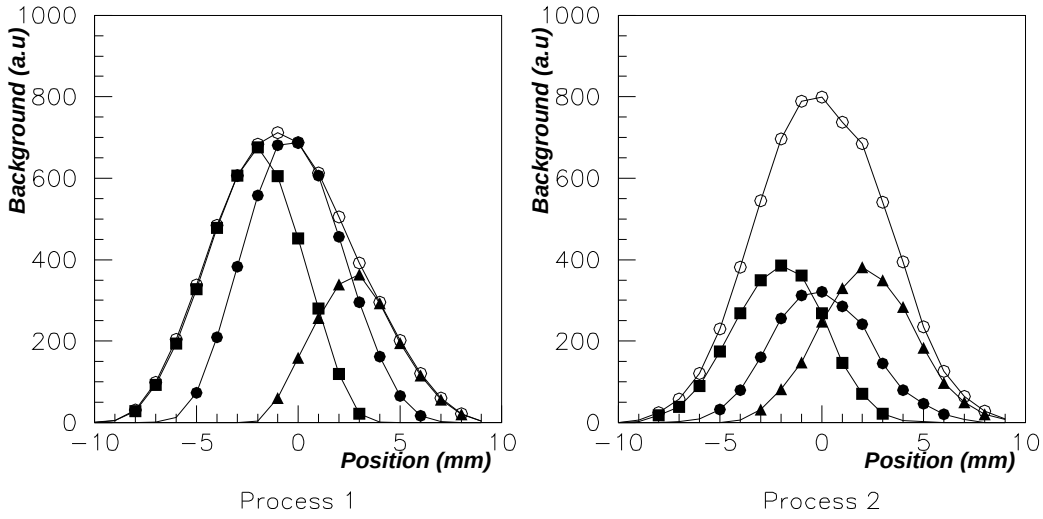

Figure B.8: Simulation of the background on the process 1 and process 2

on condition and bottom figure shows the ion pump off condition. Average pressure is $3.7 \times 10^{-7} Pa$ and $1.45 \times 10^{-6} Pa$,respectively.

In order to check the reduction of the background after improvement. We compare the background before/after improvement and ion pump on/off condition. Fig.B.10 shows the pressure dependence of the background. (2000/06/16) means the condition before the improvement and (2001/03/01) means the condition after the improvement. These data are taken on the same condition as electron current 1.5mA, threshold above 15MeV, and 1st and 2nd collimator 5mm diameter, and are utilized on the peak of the background profile of the spatial distribution. We found the reduction of the background after the improvement and these background is almost linear to the average pressure on the north straight section. If the vacuum pressure will be zero, the background settles down 2.9 kHz above 15 MeV on 1.5mA from the linear fit.

Furthermore, we note that the difference between the 10mm diameter and the 5mm diameter of the 1st collimator is almost same on the two condition ion pump on and off. On the simulation of process 1, that is the dependence from the vacuum pressure, we have no difference between the 10mm diameter and 5mm diameter of the 1st collimator. These results indicate that the difference do not depend on the vacuum pressure.

The measurement of the background is important to also know the beam physics, especially, on the low emittance beam and provide us many information on the beam condition. After the improvement of the vertical emittance, we remeasure the lifetime, horizontal emittance and vertical emittance, the

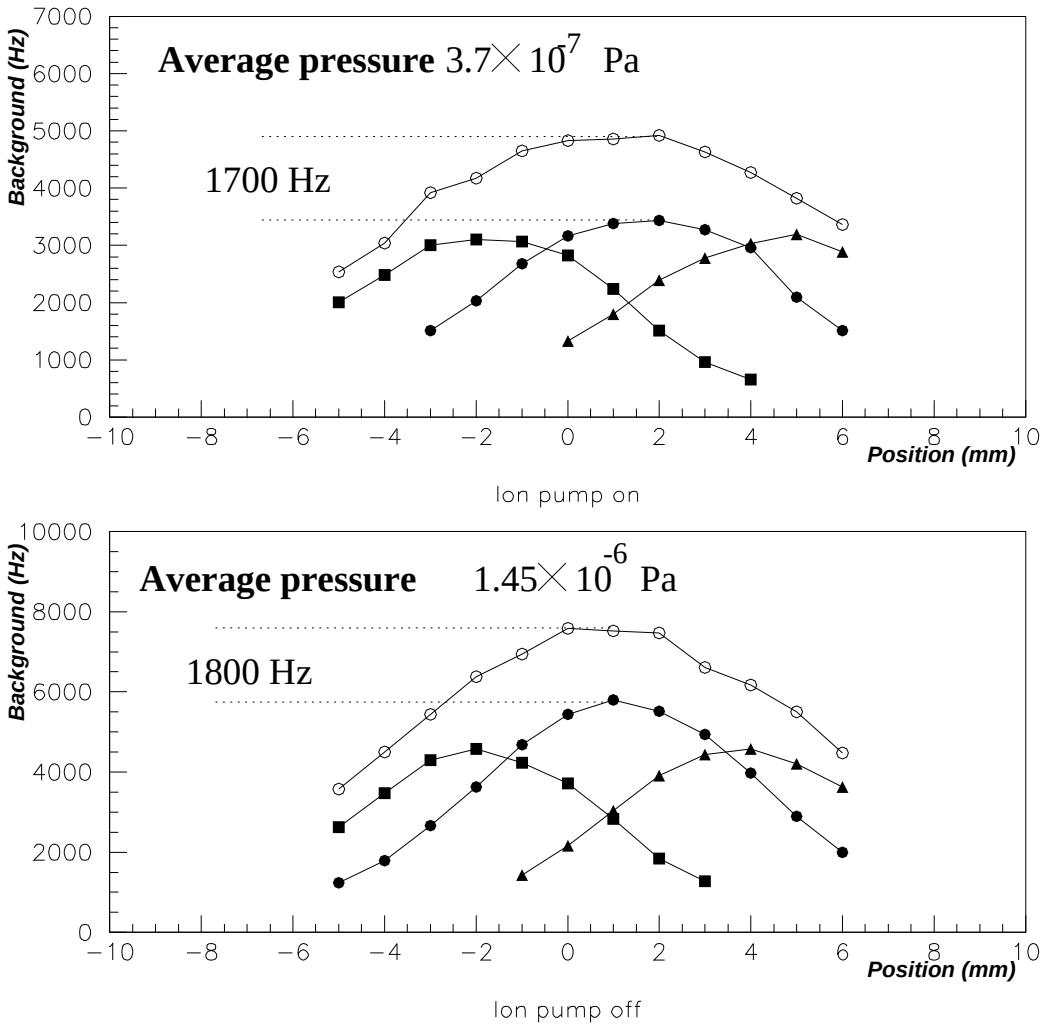

Figure B.9: Spatial distribution of the background (2001/03/01)

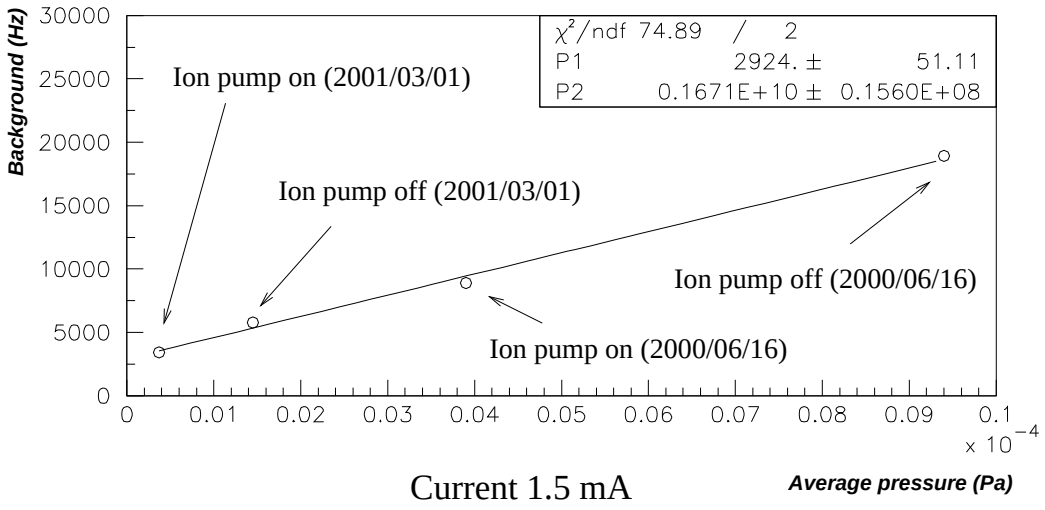

Figure B.10: Pressure dependence of the background

bunch length, and the momentum spread, simultaneously and want to know the beam physics, included the intra-beam scattering, in the ATF damping ring.

List of Figures

List of Tables

Bibliography

[1] R.Allely et.al. "A laser-based beam profile monitor for the SLC/SLD interaction region"; Nucl. Instr. and Meth.**A379** (1996) 363.

[2] M.Ross et.al.,"A high performance spot size monitor"; LINAC96 proceedings p.308 (1996),

[3] T.Shintake, "Proposal of a nanometer beam size monitor for e^+e^- linear collider"; Nucl. Instr. and Meth.**A311** (1992) 453.

[4] Clive Field , "The wire scanner system of the final focus test beam"; SLAC-PUB-6717, Nov. (1994)

[5] J.D.Jackson, "Classical Electrodynamics";2nd ed.,p661 (1975)

[6] The NLC Design Group, "Zeroth-Order Design Report for the Next Linear Collider"; SLAC report 474, May (1996).

[7] R.Brinkmann, "The TESLA superconduvtinh linear collider" ;DESY-M, 97-04,(1997).

[8] H.Henke, "Study work on the CERN Linear Collider(CLIC)"; CERN-LEP-RF, 89-62,(1989).

[9] JLC Design Study Group,"JLC Design Study" ;KEK-Report, 97-1, (1997).

[10] Edited by F. Hinode et. al.,"ATF design and study report"; KEK Internal 95-4 (1995)

[11] T. Okugi et. al.,"Evaluation of extremely small horizontal emittance" ;Phys. Rev. Special Topics- Accelerator and Beams, **2**, 022801 (1999)

[12] H.Hayano, "Wire scanners for small emittance beam measurement in ATF"; The proceedings of 20th Linear accelerator conference (2000), 'http://linac2000.slac.stanford.edu/'

[13] H.Hayano,T.Naito et.al., "Emittance measurement at KEK-ATF damping ring"; The proceedings of the 1999 Particle Accelerator Conference, New York,(1999)

[14] H.Sakai et. al.,"Measurement of an electron beam size with laser wire beam profile monitor" ;Phys. Rev. Special Topics - Accelerator and Beams , **4**, 022801 (2001)

[15] Siegman A,"Lasers";University Science Books, (1986)

[16] H.Kogelnik and T.Li,"Laser Beams and Resonators"; Applied Optics ,vol.5,no.10, (1966)

[17] J.P.Jorda et.al ,"A Fabry-Perot cavity for Compton polarimetry"; Nucl. Inst. and Meth. A412 (1998)

[18] M.E.Peskin and D.V.Schroeder,"An Introduction to Quantum Field Theory"; Addison-Wesley (1995)

[19] G.Giordano et.al,"Coherence in Compton scattering at large angles";Laser and Particle Beams, vol.15, no.1 p167 (1997)

[20] M.Takano, et. al. ,"Upgrade of the BPM readout electronics for the ATF damping ring"; Proceedings of the 6th European Particle Accelerator Conference, Stockholm (1998) 1607.

[21] K.Kubo ,"Beam development in ATF damping ring" ;Proceedings of the 6th European Particle Accelerator Conference, Stockholm (1998).

[22] SAD code is developed by KEK for the accelerator design and simulation. In detail, refer to "http://acc-physics.kek.jp/SAD/sad.html"

[23] Torus 532-100; Laser Quantum Ltd , Manchester M15 6SE United Kingdom

[24] J.D.Bierlein and H.Vanherzeele, J.Opt. Soc .Am., **B6**, 622 (1989)

[25] A. Yariv,"Optical Electronics";Holts, Rinehart and Winston, (New York, 1991), 4th ed.

[26] F.Bayer-Helms, "Coupling coefficients of an incident wave and the modes of the spherical optical resonator in the case of mismatching and misalignment", Applied Optics, Vol.23, No.9, 1369 (1984)

[27] S.A.Collins, J.Opt.Soc. Am. **60(9)**,1168(1970)

[28] LK-2000 series; Keyence K.K., Higashiyodogawa-ku, Osaka, 533-8555, Japan

[29] Leica SMART 310, Noecross, Georgia 30071

[30] T.Okugi et.al.,"Evaluation of vertical emittance in KEK-ATF by utilizing lifetime measurement"; Nucl.Instr.Meth. **A455** ,207 (2000)

[31] W.R.Nelson et al.,"The EGS4 code system"; SLAC-265, Stanford University, Stanford, (1985)

[32] Y. Sakamura, et al., "Development of a laser wire beam profile monitor (1)"; hep-ex/9907054.

[33] H. Sakai et. al., "Development of a laser wire beam profile monitor (2)"; Nucl. Instr. Meth. A **455** (2000),

[34] J.Le Duff,"Current and current density limitations in existing electron storage rings"; Nucl.Instr.Meth, **A239**, 83 (1985)

[35] J.D.Bjorken and S.K.Mtingwa, Particle Accelerators ,**13**, 115 (1983)

[36] A.Pwinski, DESY, 90-113 (1990)

[37] H.Wiedemann, "Particle Accelerator Physics"; Springer Verlag ,New York, 2nd ed.

[38] E.D Courant, H.S.Snyder, Ann.Phys. 3 (1958)

[39] Edited by A.W.Chao, M.Tigner, "Handbook of Accelerator Physics and Engineering"; World Scientific (1998)

[40] T.Okugi, "Textbook of OHO 2000"; ,Seminar of the high energy accelerator held on KEK.

[41] R.H.Helm, et. al. , PAC73

[42] T.O.Raubenheimer ,et.al. "The vertical emittance in the ATF damping ring"; Nucl. Inst. Meth. A **335** 1 (1993)